This electronic thesis or dissertation has been downloaded from Explore Bristol Research, http://research-information.bristol.ac.uk

Author:
Bologna, Simone

Title:
Trigger design studies at future high-luminosity colliders

General rights
Access to the thesis is subject to the Creative Commons Attribution - NonCommercial-No Derivatives 4.0 International Public License. A copy of this may be found at https://creativecommons.org/licenses/by-nc-nd/4.0/legalcode This license sets out your rights and the restrictions that apply to your access to the thesis so it is important you read this before proceeding.

Take down policy
Some pages of this thesis may have been removed for copyright restrictions prior to having it been deposited in Explore Bristol Research. However, if you have discovered material within the thesis that you consider to be unlawful e.g. breaches of copyright (either yours or that of a third party) or any other law, including but not limited to those relating to patent, trademark, confidentiality, data protection, obscenity, defamation, libel, then please contact collections-metadata@bristol.ac.uk and include the following information in your message:

- Your contact details
- Bibliographic details for the item, including a URL
- An outline nature of the complaint

Your claim will be investigated and, where appropriate, the item in question will be removed from public view as soon as possible.

Trigger design studies at future high-luminosity colliders

By

SIMONE BOLOGNA

School of Physics
UNIVERSITY OF BRISTOL

A dissertation submitted to the University of Bristol in accordance with the requirements of the degree of DOCTOR OF PHILOSOPHY in the Faculty of Science.

OCTOBER 2020

Word count: 31726

ABSTRACT

The LHC will enter in 2026 its high-luminosity phase which will deliver a peak instantaneous luminosity of $7.5 \times 10^{34}\ \mathrm{cm}^{-2}\ \mathrm{s}^{-1}$ and produce events with an average pile-up of 200. In order to pursue its ambitious physics programme, the CMS experiment will undergo a major upgrade. The level-1 trigger will be replaced with a new system able to run the particle flow algorithm. An algorithm that reconstructs jets and computes energy sums from particles found by the particle flow algorithm is presented in this thesis. The algorithm is able to provide similar performance to offline reconstruction and keep the same p_{T} threshold as in the previous CMS runs. The algorithm was implemented in firmware and tested on Xilinx FPGA. An agreement rate of 96% was obtained in a small-scale demonstrator setup running on a Xilinx FPGA. The full-scale algorithm is expected to use around 41.5% of LUTs, 11.6% of flip-flops, and 2.9% of DSPs of a Xilinx VU9P FPGA running at the frequency of 360 MHz.

The FCC-hh project studies the feasibility of a hadron collider operating at the centre-of-mass energy of 100 TeV after the LHC operations have ended. The collider is expected to operate at a base instantaneous luminosity of $5 \times 10^{34}\ \mathrm{cm}^{-2}\ \mathrm{s}^{-1}$, and reach a peak value of $30 \times 10^{34}\ \mathrm{cm}^{-2}\ \mathrm{s}^{-1}$ corresponding to an average pile-up of 200 and 1000, respectively. Rates of a trigger system of a detector at FCC-hh were estimated by scaling rates of the Phase-2 CMS level-1 trigger and by developing a parameterised simulation of the Phase-1 trigger system. The results showed that at the instantaneous luminosity of $5 \times 10^{34}\ \mathrm{cm}^{-2}\ \mathrm{s}^{-1}$ the 100-kHz p_{T} threshold is expected at 85 GeV, 170 GeV, and 350 GeV for single muon, e/γ , and jet triggers, respectively.

ACKNOWLEDGEMENTS

I would like to thank the people I had the pleasure to work and share this experience with. First of all, I am grateful to my supervisor Jim Brooke for helping me with his wise advice throughout my PhD research, Paris Sphicas for his supervision at CERN, Dave Newbold and Joel Goldstein. I would like to thank Aaron Bundock, Emyr Clement, and Katie for their help in testing and demonstrating my firmware on hardware. A special thanks goes to Alessandro Thea, without him I would probably have not started this project in the first place (although I think he now regrets this!).

I thank Yingpu, who I have shared a significant part of my PhD troubles with. I would like to thank my colleagues Joe, fellow hiker, and Esh, the author of innumerable memes, for the fun times in and outside the office. I met amazing people at CERN that I would like to include in these acknowledgements: Glenn, dino-fanatic and software guru; Stefan, host of memorable Stefanfests; Amy, my favourite hiking partner; Simone, my theatre boss and owner of a Beethoven bust; and Federica, who introduced me to the joy of half marathons. Thanks to them, my staying at CERN was an amazing and unique experience.

Finally, a big *grazie* to my parents and brothers, who supported me all the time. *Grazie* to the *zagatori della valmorea* that have been together with me since ever. A special *grazie* to Bobbi, who patiently listened to my stressed rants, and to Erika and Federico.

AUTHOR'S DECLARATION

I declare that the work in this dissertation was carried out in accordance with the requirements of the University's Regulations and Code of Practice for Research Degree Programmes and that it has not been submitted for any other academic award. Except where indicated by specific reference in the text, the work is the candidate's own work. Work done in collaboration with, or with the assistance of, others, is indicated as such. Any views expressed in the dissertation are those of the author.

SIGNED: .... DATE: ....

TABLE OF CONTENTS

Page

LIST OF TABLES

TABLE **Page**

LIST OF FIGURES

CHAPTER 1

INTRODUCTION

Particle physics studies the properties and the interactions of the fundamental particles that form the universe. Accelerator experiments constitute an important branch of particle physics experiments. In these experiments, particles such as protons and electrons are accelerated and collided at high centre-of-mass energy with other objects. These objects can be either fixed targets, or other accelerated particles. The particles generated in the collision give insight on the nature of the interaction that has produced them. Particle detectors are employed to identify and reconstruct the properties of the produced particles. The data acquisition system (DAQ) collects data produced by a particle detector and converts it to a format that can be permanently stored and later analysed. The trigger system is a device that can recognise when interesting activity has been identified by the detector and can subsequently activate the DAQ. The trigger is crucial in experiments where only a small fraction of the events reconstructed by the detector actually contains interesting signals, as it prevents the DAQ and storage systems from being saturated with background events.

1.1 Triggering at hadron and lepton colliders

The physics of interactions at hadron and lepton colliders are substantially different. Consequently, triggering solutions in particle detectors must adapt to the type of particle collider. Figures 1.1(a) and Figure 1.1(b) displays the cross sections of interesting processes as a function of the centre-of-mass energy $\sqrt{s}$ at proton-proton and electron-positron colliders, respectively. At hadron colliders, the cross section of interesting signals is typically many orders of magnitude lower than the dominating background, which is inelastic proton scattering. For instance, the total cross section of proton-proton scattering at $\sqrt{s} = 14$ TeV is around 10^8 nb. The cross section of the Higgs boson production via vector boson fusion is 10^{10} times smaller. This can be compared

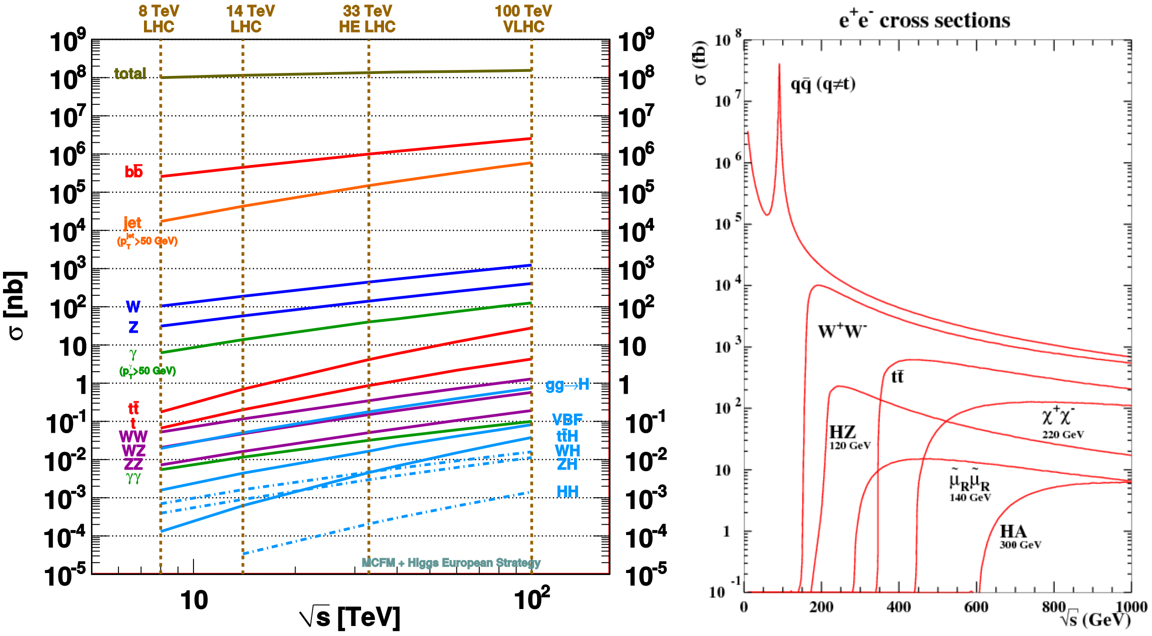

(a) Proton-proton

(b) Electron-positron

Figure 1.1: Cross-section of various physics processes at proton-proton and electron-positron colliders. Figure (a) is taken from Ref. [1]; Figure (b) is taken from Ref. [2].

with lepton colliders where background interactions have a much smaller contribution. At lepton colliders, the cross section of Higgs boson production in association with a Z boson is only two times smaller than the dominant background interaction, i.e. fermion pair production.

In order to produce interesting physics within a reasonable experimental lifetime, hadron colliders must reach high instantaneous luminosity ($\mathscr{L}_{\text{inst}}$). This is achieved by producing an high rate of events where very focused bunches of protons are collided, generating multiple simultaneous interactions. Events are generally very busy and contain a large number of particles. Typically, only one proton pair in an event leads to an interesting interaction, while the others constitute a background. The interesting interaction is often called “primary vertex”, while the background is referred to as “pile-up” (PU). This is not the case for lepton colliders, where $\mathscr{L}_{\text{inst}}$ and the background in an event can be lower thanks to the higher signal-to-background ratio.

Large amounts of information must be read from the detectors at hadron colliders, as they often require highly segmented devices and precise tracking to reject pile-up interactions and identify the primary vertex. This is not the case for a detector at a lepton collider, where the bandwidth required is typically much lower thanks to lower collision rate. For instance, a detector at FCC-hh, a circular hadron collider under study for the post-LHC era, is expected to yield around 2 PB/s of untriggered data [3]. In contrast, the detector under study for the FCC-ee accelerator, which is the lepton collider counterpart of FCC-hh, is expected to generate around 1 TB/s of untriggered data [4], three orders of magnitude less.

The differences in the general properties of hadron and lepton colliders lead to significantly different data rates and, therefore, trigger and data acquisition system architectures. Detectors at hadron colliders typically require sophisticated trigger architectures. Reading out and processing every event for the entire detector is generally not possible due to the enormous data rates and computing costs, therefore triggers use strategies based on successive selections to filter out data. Solutions for detectors at lepton colliders are radically different and generally much simpler. For instance, the data acquisition system of the FCC-ee detector is expected to read out every event. A fully software-based trigger running on a computer farm is run for data filtering.

1.2 Historical background and present status of triggers

The first particle physics experiments did not have a trigger and data acquisition systems. Selecting and storing data was a laborious process that was manually performed by the experimenters. For instance, in the Rutherford scattering experiment conducted by Rutherford, Geiger, and Marsden in 1911 [5], Geiger and Marsden manually counted the amount of α particles scattered at given angles. The ability and speed of the experimenters in counting was a limiting factor in the rate of events that could be processed, thus impacting the statistics of the experiment.

Methods to automate the measurement and alleviate the stress on the experiment operators were proposed in 1919 by Kovarik [6]. Kovarik demonstrated a system able to detect signals produced by incoming α particles and register them on chronograph paper. This system represented one of the first instances of an automated trigger and DAQ system in physics.

In the second half of the twentieth century, trigger and DAQ techniques evolved with the development of electronics. Bubble chambers were one of the first particle detectors in accelerator experiments. The devices had an automated DAQ system that periodically took pictures of the status of the chamber based on the accelerator cycle. No trigger system was in place, however, and the selection was manually performed by scientists visually scanning the pictures for the signal. The rate of these experiments was low, around a few Hz. The need for fully automated systems to filter out data rose as the statistics required for discovery increased, due to the increasingly rare phenomenon being studied.

The first trigger systems were designed for specialised experiments targeting a restricted set of measurements. These systems were simple, and applied thresholds or coincidence requirements to analog electric signals to look for basic detector activity or specific signal coincidences. For instance, in 1964, Christenson and Cronin reported the measurement of the two-pion decay of the K_0^2 [7]. Their experimental setup consisted of two spectrometer arms, both equipped with spark chambers that were triggered by a coincidence of a water Cherenkov detector and a scintillator located at the end of each arm. A camera took a picture of the tracks revealed by the spark chamber when the coincidence caused by the two-prong decay was detected, thus having a triggered readout of the experimental apparatus.

The UA1 and UA2 experiments at the Super Proton-Antiproton Synchrotron (SPPS) in 1981 [8] were the first examples of a large collaboration experiment with a broad physics programmes and a modern trigger. The amount of raw data produced by the experiments was too large to handle for the DAQ technology of the time. For instance, each event in the UA1 experiment was 100 kB in size. The accelerator had a collision rate of 250 kHz, therefore the experiment produced around 25 Gb/s of untriggered data. The experiments faced the challenge of rejecting a large amount of background events while being able to accept a broad range of rare different signals. The UA1 and UA2 experiments adopted a complex three-level trigger system where more information to discriminate between signal and background was available as the event progressed through the selection chain. Ultimately the system reduced rates down to 4–5 Hz, applying a rate reduction factor of ≈ 50000. The level-1 trigger of both experiments consisted of electronic boards able to find events with interesting activity within ≈ 3 µs, which was the time between two consecutive events. The hardware performed simple operations such as finding energy clusters corresponding to electrons and hadron jets, computing energy sums, or identifying muon tracks. The level-1 trigger of the UA1 experiment was a fully digital system, which was considered to be more flexible and stable [9] than an analog trigger. Operations on digitised data were performed using associative tables in RAMs that were hard wired on custom boards. UA2 designed a trigger solution that mixed both analog and digital electronics in NIM and custom boards. The second and third trigger layers of the two experiments could afford longer processing times, therefore they were equipped with microprocessors running on real time systems that partially reconstructed events and applied more refined selections.

Similar techniques were used in the ALEPH, DELPHI, L3, and OPAL experiments [10–13] at the large electron-positron collider (LEP) [14] and in the CDF [15] and D0 [16] experiments during the first run of Tevatron [17]. Trigger requirements at LEP, which was a lepton collider, were less demanding due to the much lower background cross sections. Therefore, the LEP experiments implemented a trigger system able to mostly identify genuine electron-positron interactions. The system mainly rejected data produced by effects such as the interaction between the beam and the residual gas in the beam pipe. Tevatron, which was a proton-antiproton collider, delivered a peak $\mathscr{L}_{\text{inst}}$ around 5 times larger than at the SPPS with a bunch spacing of 3.5 µs in its first run, corresponding to a collision rate of ≈ 250 kHz. The maximum rate that the storage system could accept was 5 Hz. Therefore, in order to maintain the same rate reduction factor as the UA1 and UA2 experiments at the higher $\mathscr{L}_{\text{inst}}$, the CDF and D0 experiments sent information from the calorimeters with finer granularity. The experiments used this information to implement more refined reconstruction algorithms able to better distinguish objects in the calorimeters.

In order to increase $\mathscr{L}_{\text{inst}}$ and extend their physics reach, the HERA electron-proton collider [18] and the Run-II of Tevatron [19] run with bunch spacings of 96 ns and 396 ns, respectively. This introduced a new challenge for trigger systems. Previous trigger systems were not pipelined, hence they had to finish processing an event before the next bunch crossing. This was not technically feasible in a time scale of ~ 100 ns. Therefore, the triggers of the experiments at HERA [20, 21] and Tevatron [22, 23] were redesigned to be pipelined. Data from the detector were fully digitised and stored in frontend buffers able to keep data from over 40 consecutive bunch crossings. At the same time, a subset of the detector data was sent to the level-1 trigger for a first selection. The L1T consisted of custom boards with ad-hoc designed circuits and field programmable gate arrays (FPGAs). Events accepted by the level-1 trigger were read out from the front end buffers and sent to the high-level trigger, which consisted of a computer farm, for further filtering. The rate of accepted events to save was also increased to 30–100 Hz thanks to the progress in computing systems.

The large hadron collider (LHC) [24] adopted an even smaller bunch spacing, 25 ns, and produced events with around 50 simultaneous proton-proton interactions in order to increase $\mathscr{L}_{\text{inst}}$. Trigger systems of the four LHC experiments, ATLAS, CMS, LHCb, and ALICE [25–28] adopted ASICs and FPGAs in their level-1 trigger and commercial computers in their high-level trigger to process a large amount of fine granularity data. In 2026 LHC [29] is expected to enter the high-luminosity phase and produce around 200 simultaneous interactions per bunch crossing. The experiments will completely redesign their triggers and try new triggering solutions to achieve their physics goals. The level-1 trigger of the ATLAS [30] and CMS [31] detectors will correlate information from multiple subdetectors by running algorithms similar to the offline ones in hardware. LHCb [32] and ALICE [33] will try an innovative solution based on a triggerless readout: the detectors will be read out every bunch crossing and every event sent to the high-level trigger for filtering. The experience with these new systems will be crucial in understanding the direction triggers in which future accelerator experiments will evolve.

1.3 Overview of the thesis

The original work in this thesis consists of two studies connected by the common theme of developing trigger systems in high-luminosity colliders. A short overview of physics at hadron colliders will be presented in Chapter 2. The main background and interesting signals will be introduced along with their implications for the trigger system. The LHC and CMS experiments will be described in Chapter 3. Focus will be given to the upgrade of the CMS level-1 trigger, which is the context for Chapters 4 and 5. In the former, the design and performance of a jet trigger algorithm will be presented. In the latter, the development and implementation on hardware of the same algorithm will be shown. Finally, the analysis of the performance and rates of a level-1 trigger at FCC-hh, a proposed post-LHC hadron collider, will be presented in Chapter 6.

CHAPTER 2

PHYSICS AT HADRON COLLIDERS

An introduction to the main physics processes at hadron colliders and their impact on the trigger will be given in this chapter. The particles and the forces described by the standard model will be introduced in Section 2.1. The physics of the strong force will be shortly explained in Section 2.2. Particular attention will be given to the impact that the force has on properties of the proton interactions at hadron colliders, and to proton inelastic scattering, which represents the dominant process at hadron colliders. Finally, a few interesting signals at LHC will be presented in Section 2.3 together with some of their features that can be exploited to trigger on.

2.1 The standard model

The standard model (SM) [34] is a quantum field theory describing the way the fundamental particles of the universe interact via three of the four known forces: strong, weak, and electromagnetic. Figure 2.1 shows the particles that are included in the model. Particles are divided in two major groups: fermions, i.e. particles with half-integer spin; and bosons, particles with integer spin.

There are 12 fundamental fermions, divided in three generations, each one of increasing mass. Each generation consists of a charged and a neutral lepton, the latter called neutrino, and a pair of quarks. Quarks can interact via the strong force, differently from the leptons. Electrically charged fermions can interact via the electromagnetic force. Every fermion can interact via the weak force.

Five fundamental bosons are included in the model. Four of them are the force carriers, also called gauge bosons: fermions interact with each others by exchanging these bosons. The strong force is carried by gluons, the electromagnetic one by photons, and the weak one by the W and Z

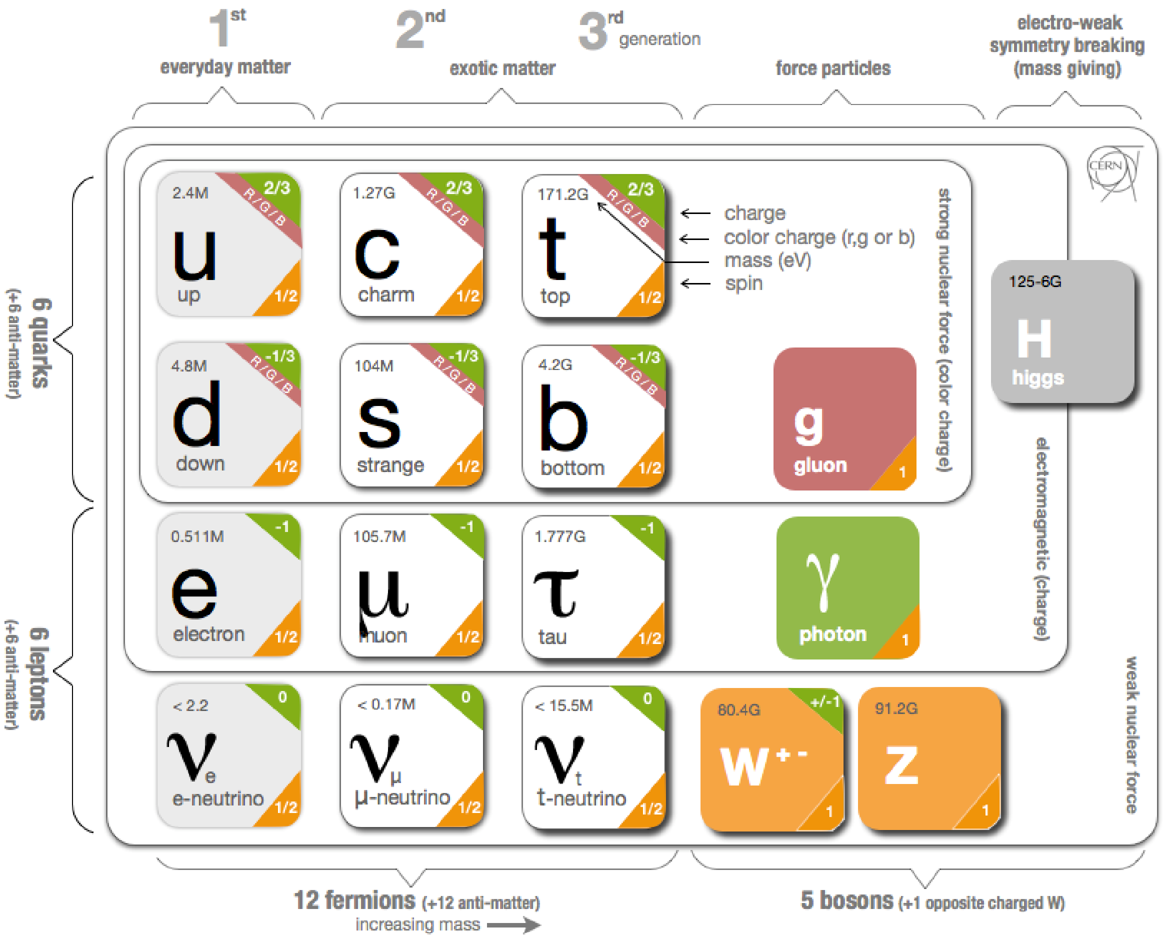

Figure 2.1: Particles of the standard model. Taken from Ref. [35].

bosons. Gluons are electrically-neutral, massless particles, and possess colour charge, therefore they can interact with other gluons. Photons are massless and electrically neutral. The W bosons are electrically charged and have a mass of $m_{\mathrm{W}} \approx 80$ GeV. The Z bosons are electrically neutral and have a mass of $m_{\mathrm{Z}} \approx 91$ GeV. Finally, the Higgs boson is the particle responsible for giving particles their mass via the mechanism of spontaneous electroweak symmetry breaking. It is neutral and has a mass of $m_{\mathrm{H}} \approx 125$ GeV.

The strength of a force is described in the standard model via a coupling parameter between the fermion and force carrier boson. In addition, each force has a characteristic range of action. The strong force has a range of $\approx 10^{-15}$ m and is the strongest force over its range of action. The coupling of the strong force depends in the model on the energy scale of the interaction, as described in Section 2.2. At energy scales around 100 GeV its value is $\approx 10^{-1}$. The electromagnetic force is the second strongest force: it has infinite range and a coupling constant of $\approx 10^{-2}$. The weak force is the weakest: it has a range of $\approx 10^{-17}$ m and a coupling constant of $\approx 10^{-7}$.

2.2 The strong force

Processes mediated by the strong force have the largest cross section at LHC and are the main background at hadron colliders. Therefore, understanding the characteristics of these interactions is fundamental in order to develop effective triggers.

The strong force is responsible for binding quarks forming protons and neutrons and the residual force coming from the quarks inside nucleons is also responsible for aggregating them in atomic nuclei. Quantum chromodynamics (QCD) [34, 36] is the field theory describing the physics of the strong interaction. Quarks and gluons, which have colour charge, can interact via this force. The three interaction vertices of QCD are shown in Fig. 2.2.

The strong interaction exhibits a number of features that makes this force very complex and with a large variety of phenomena. Firstly, three different types of colour charge exists. Secondly, the force carrier itself is charged, enabling gluon-gluon interactions to occur, as shown in Figs. 2.2(b) and 2.2(c). Finally, its coupling strength weakens as the interaction energy scale increases. In the electromagnetic force, the force coupling grows as the distance between the interacting particles decreases, which corresponds to raising the interaction energy. This is due to the screening effect generated from the polarisation of virtual electron-positron pairs surrounding charged particles. A similar effect occurs in QCD, however the gluon self-coupling also causes gluon pairs to be produced in addition to the quark-antiquark pairs. The gluons causes an antiscreening effect that increases the coupling of the strong force at higher distance, corresponding to lower energy scales. The antiscreening effect is stronger than the screening effect from the polarisation of quark-antiquark pairs. Consequently, the strength of the strong force behaves in opposite fashion than that of the electromagnetic force. The coupling strength decreases at smaller distances, i.e. at higher energy scales, and the contribution of the strong interaction to quarks becomes negligible. This feature is called asymptotic freedom, as quarks behave as free particles in this regime. Conversely, at lower interaction energy, i.e. larger distance, the strength of the strong force increases. When a quark is being separated from an hadron, the intensity of the strong

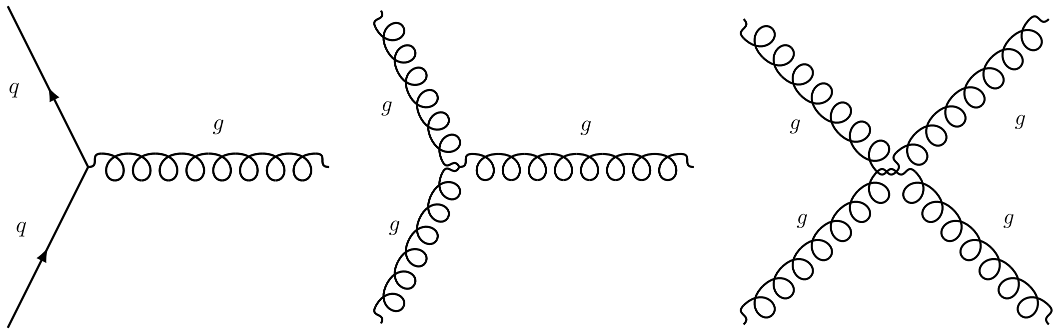

(a) Quark-gluon vertex (b) Three-gluon vertex (c) Four-gluon vertex

Figure 2.2: The three interaction vertices of QCD.

force binding the system together becomes larger. Eventually, if enough energy is introduced, the system produces a quark-antiquark pair and two new hadrons are generated. This leads to a phenomenon called colour confinement: single free quarks can not be observed, as quarks can only be found in colour-neutral hadron systems.

These two phenomena make the strong force more difficult to study than the electromagnetic and weak interaction. Interactions mediated via the electromagnetic and weak force are typically predicted using perturbative methods, expanding the interaction in terms of a power series in the force coupling. This method can be applied as the coupling of these two forces is small, allowing the expansion to be truncated when the desired theoretical precision is reached. However, the strong force has an increasingly strong coupling at lower energies. This implies that the theory has two regimes. At energy scales close to asymptotic freedom, the coupling is small enough to enable the use of perturbative methods to study the interaction. As the energy decreases, the coupling of the force increases, eventually entering a regime where perturbative methods can not be used any longer. In this situation alternative models and methods have to be used.

2.2.1 The parton model

Quarks inside all hadrons interact in the non-perturbative regime of QCD. Building a complete model of hadrons using non-perturbative methods is hard, consequently the parton model [36] was developed to circumvent the issue. In this model, hadrons are made up of two quark types, the valence and the sea quarks, shown in Fig. 2.3. The valence quarks, represented in purple in Fig. 2.3, determine the quantum numbers of an hadron. For instance a proton contains two up and one down valence quarks, leading to an electric charge of 1. The sea quarks are quark-antiquark pairs, displayed in green and orange in Fig. 2.3, that are produced when gluons exchanged by the quarks, represented as looped lines in Fig. 2.3, split. The constituents of the proton, including the sea quarks and gluons, are referred to as partons.

A parton distribution function (PDF) is the probability of finding a parton carrying a fraction x of the total hadron momentum. PDFs can not be computed analytically, due to the non-perturbative nature of QCD at the hadron scale, therefore they are typically measured in dedicated experiments via electron-proton deep inelastic scattering [38]. Figure 2.4 shows two PDFs in a proton at two different interaction energies Q produced by the CTEQ collaboration [39]. The resolving power $\hbar/Q$ of the scattering increases with Q, causing the PDFs to vary. The evolution of the PDFs as a function of Q is described in the high-energy interaction limit, which is in the perturbative regime of QCD, by the Dokshitzer-Gribov-Lipatov-Altarelli-Parisi (DGLAP) equation [40–42].

2.2.2 General properties of proton-proton collisions

The collinear factorisation theorem [43] is used to model scattering processes in hadron collisions. Figure 2.5 shows a diagram of a hard scattering process between two protons of momentum p_1 and p_2. Using the theorem the scattering can be seen as an interaction between free partons

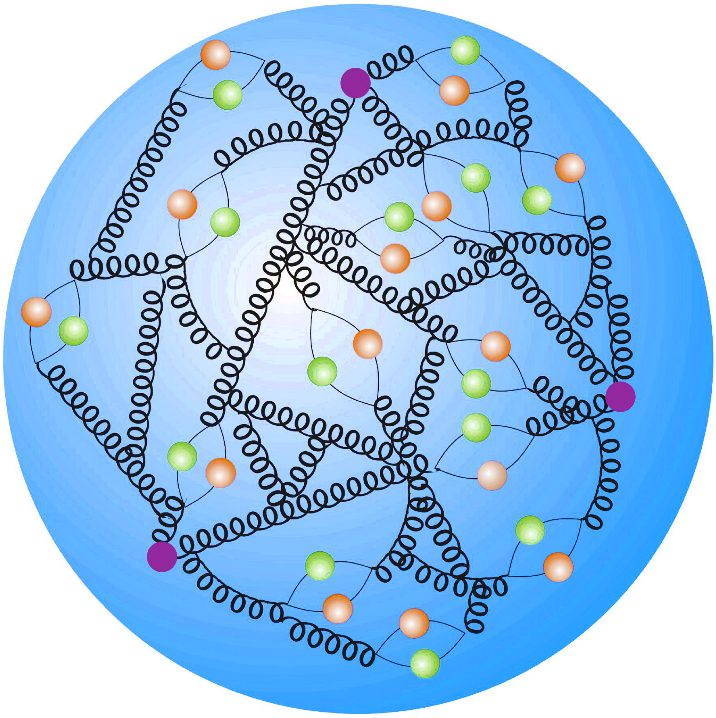

Figure 2.3: Representation of the proton structure in the parton model. The purple quarks are valence quarks. The green and orange particles are sea quarks and antiquarks, respectively. The looped lines are gluons. Taken from Ref. [37].

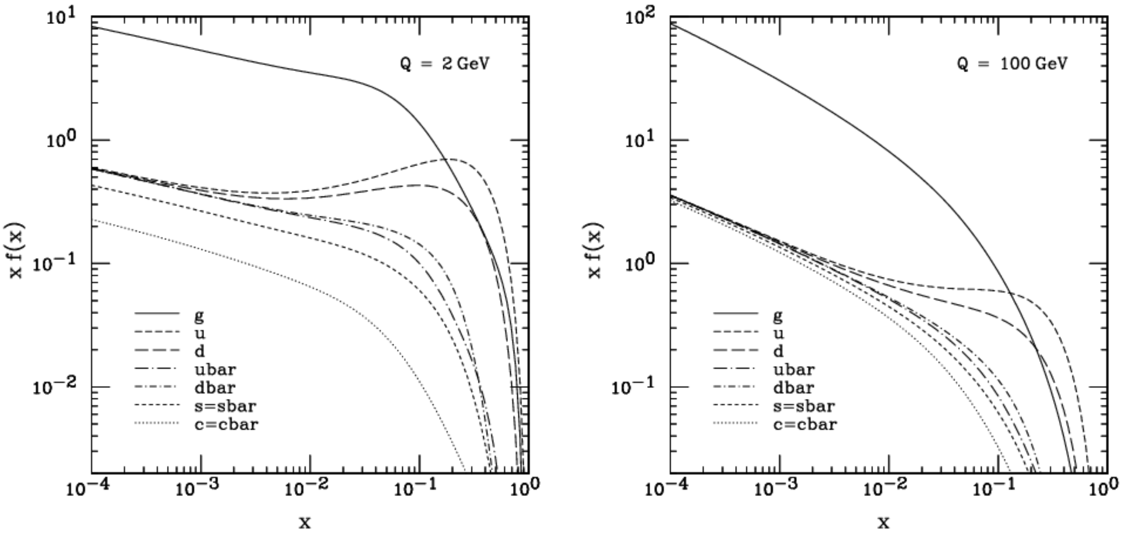

(a) $Q = 2$ GeV (b) $Q = 100$ GeV

Figure 2.4: CTEQ6M parton distribution functions at the interaction energy Q = 2 and 100 GeV. Taken from Ref. [39].

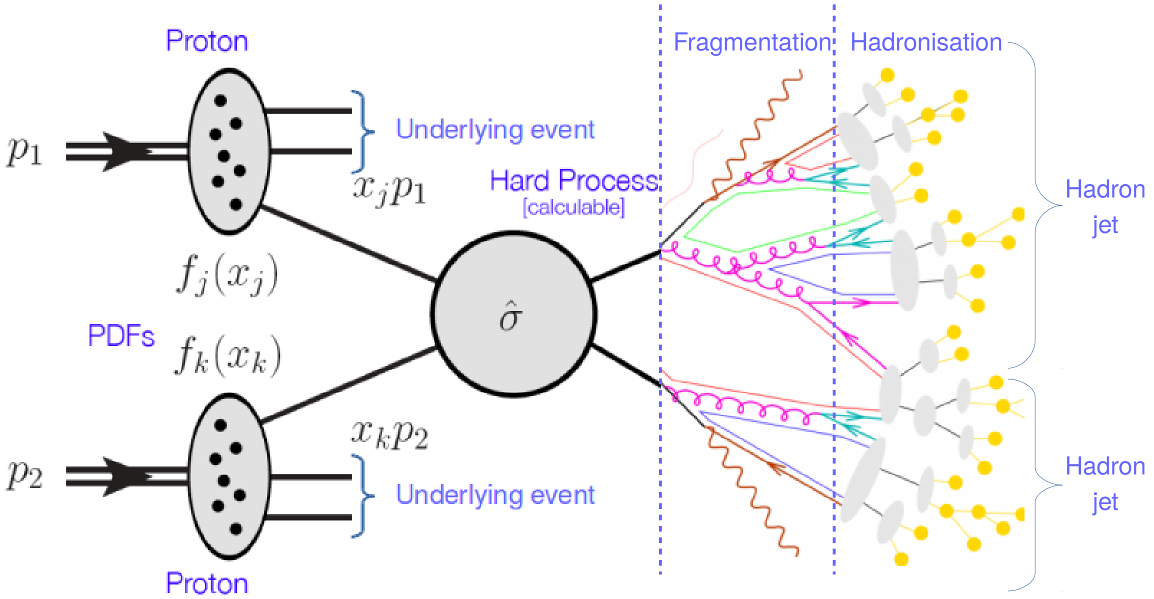

Figure 2.5: Diagram of a hard scattering process between protons. Taken from Ref. [44, 45].

whose momentum is distributed according to the PDFs. Therefore, the cross section can be computed as:

$$\sigma = \sum_{i,j} \int dx_1 dx_2 \cdot f_i(x_1, Q^2)\, f_j(x_2, Q^2) \cdot \hat{\sigma}_{i,j}(x_1 p_1, x_2 p_2) \tag{2.1}$$

where:

- The sum over i and j represents the sum over every parton participating the interaction.
- $f_i(x_1, Q^2)$ and $f_j(x_2, Q^2)$ are the PDFs of the two interacting partons.
- $\hat{\sigma}_{i,j}(x_1 p_1, x_2 p_2)$ is the cross section of the hard process between the two partons i and j with momenta $x_1 p_1$ and $x_2 p_2$, respectively. This term can typically be computed in perturbative theory.

Any other product in an event that is not produced by the hard interaction constitutes the underlying event (UE). The UE typically consists of interactions between the remnants of the original protons and radiation emitted during the hard interaction. The UE is typically produced by non-perturbative processes, therefore phenomenological models tuned with real collision data are employed to describe it.

Hadron interactions typically generate a number of quarks and gluons. As these products get further away from the interaction point, a process called hadron fragmentation begins: the original particles emit new radiation that further results in more quarks being produced. The radiation in this stage is typically low energy and collinear. Ultimately, the fragmentation stage ends in a group of quarks that aggregate in hadron states, in a process called hadronisation. Some of these hadrons are unstable, and decay after a short time. Particle detectors typically observe a group of hadron and leptons, the latter mostly originating from weak decays, centred around a common axis. This group is called a hadron jet. In order to reconstruct the properties of the original quark, all the particles originating from the same quark must be grouped together in a process named jet clustering. More details on the jet clustering algorithms will be given in Section 2.2.2.2.

In contrast to lepton colliders, the momenta of the two interacting partons, $x_1 p_1$ and $-x_2 p_2$, are generally not equal. Therefore, the centre-of-mass system of the collision is boosted with respect to the detector frame of reference. This causes products to be boosted along the beam direction. The pseudorapidity η is typically used in experiments at hadron colliders to indicate the longitudinal angle of a particle:

$$\eta = -\ln\left[\tan\left(\frac{\theta}{2}\right)\right] \tag{2.2}$$

where θ is the longitudinal angle. The pseudorapidity is connected to the rapidity y:

$$y = \frac{1}{2}\ln\left(\frac{E+p_{\mathrm{L}}}{E-p_{\mathrm{L}}}\right) \tag{2.3}$$

where E is the energy of the particle and p_{L} is the total momentum along the beam axis. In the high-energy limit in which the mass contribution is negligible or null, the pseudorapidity is a convenient approximation of the rapidity. Figure 2.6 shows the correspondence between η and θ.

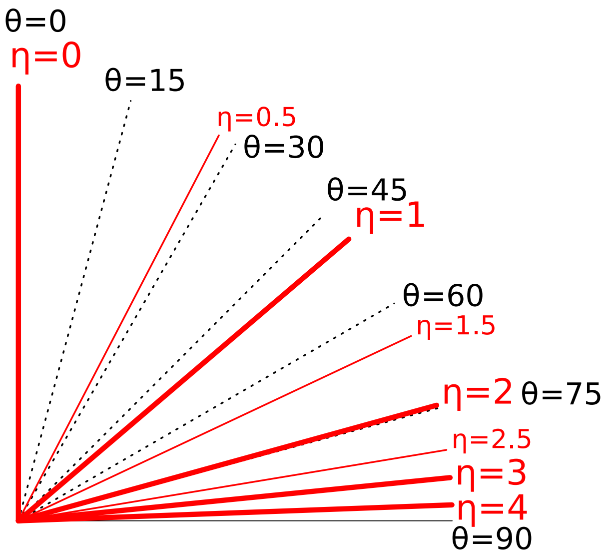

Figure 2.6: Correspondence between η and θ. Taken from [46].

2.2.2.1 QCD scattering

The dominant interaction that generates some activity in the central area of a particle detector is the inelastic proton-proton QCD scattering. Understanding its properties is fundamental, as QCD scattering constitutes the pile-up background at hadron colliders and the dominant background for the level-1 trigger. The total cross section for this process can be broken down into three contributions [47]:

$$\sigma_{\text{inel}} = \sigma_{\text{SD}} + \sigma_{\text{DD}} + \sigma_{\text{ND}} \tag{2.4}$$

where:

- σ_{SD} is the cross section for single diffraction, i.e. a process where one proton leaves the collision intact and the other is broken down in its components, generating new particles. This process generates some activity in the area close to the beam line in the direction of the diffracted particle.

- σ_{DD} is the cross section for double diffraction, i.e. a process where both protons are broken down in their components. This process generates some activity in the area close to the beam line in both directions.

- σ_{ND} is the cross section for non-diffractive interactions. These processes generate particles that can reach $\eta = 0$, i.e. the central part of a particle detector.

The non-diffractive component of the cross section constitutes what are known as minimum bias events, i.e. events that are selected with the minimum possible requirements to detect an inelastic collision. The cross-section of these events at $\sqrt{s} = 13$ TeV is around 78 mb [48].
Fig. 2.7 shows the highest (leading) p_{T} , η, and multiplicity distributions for charged particles measured by the CMS experiment in minimum bias events at $\sqrt{s} = 13$ TeV , compared with predictions obtained from the event generators Pythia v8.153 [49] and EPOS [50] tuned for the LHC experiments. The final products of the interactions in minimum bias events are typically low-p_{T} , with most of the products having $p_{\text{T}} < 5$ GeV. Particles are uniformly spread over the η range. In the θ dimension, this implies that the particle density increases closer to the beam pipe. Therefore, detectors at hadron collider must carefully provide fine granularity reconstruction in the forward region in order to successfully measure events in high pile-up conditions.

2.2.2.2 Jet clustering

A comprehensive review of the jet clustering algorithms and the properties they must satisfy is found in Ref. [52]. All jet algorithms should satisfy two properties: infrared and collinear (IRC) safety. Collinear gluon radiation during fragmentation and the emission of low energy gluons do not affect jet reconstruction in a IRC safe algorithm. These properties make jet algorithms insensitive to effects that would lead to less accurate reconstruction of the particle originating

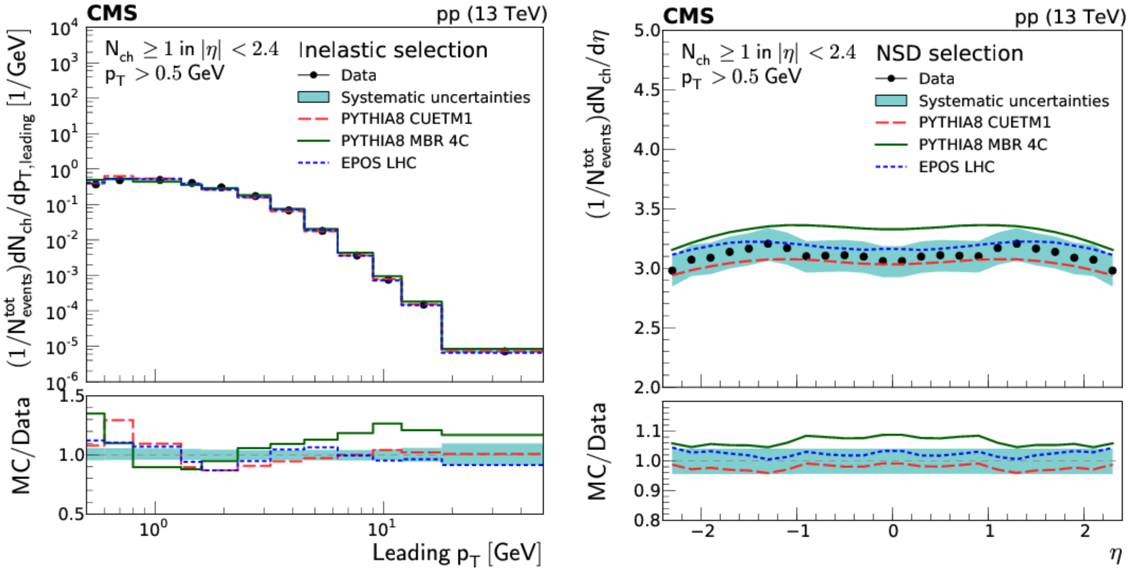

(a) Leading p_T distribution of charged particles

(b) η distribution of charged particles

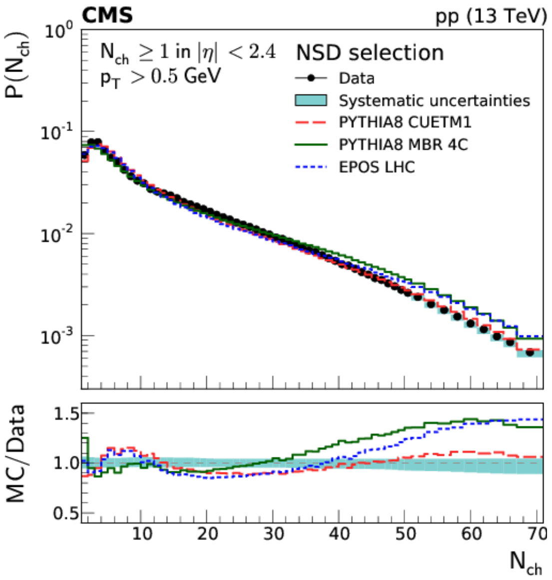

(c) Multiplicity distribution of charged particles

Figure 2.7: Leading p_T , η, and multiplicity distributions of charged particles in minimum bias events measured by the CMS experiment at $\sqrt{s} = 13$ TeV compared with predictions by the event generators Pythia and EPOS. Taken from Ref. [51].

the jet. In addition, from a theoretical standpoint, collinear splitting and infrared emission are typically related to divergent matrix elements in perturbation theory. The divergences cancel out only if jets are reconstructed with a IRC safe algorithm.

The experiments at LHC, including CMS, run the anti-k_T algorithm [53, 54] to reconstruct jets in physics analyses, which is IRC safe. The anti-k_T algorithm is a sequential recombination algorithm. In this algorithm, the following distance measure is computed for all the possible particle pairs in an event:

$$d_{ij} = \min(p_{\mathrm{T},i}^{-2}, p_{\mathrm{T},j}^{-2}) \frac{\Delta R_{ij}^2}{R^2} \qquad \Delta R_{ij}^2 = (\eta_i - \eta_j)^2 + (\phi_i - \phi_j)^2 \tag{2.5}$$

where i and j are the two particles in the pair and R is a configurable parameter that determines the maximum radius of a jet. In addition, for each particle i the distance measure:

$$d_\mathrm{self} = p_{\mathrm{T},i}^{-2} \tag{2.6}$$

is obtained. The minimum of all d_{ij} and d_self is then found. If it is d_{ij}, the corresponding particles i and j are removed from the particle list, combined into a new object, and the resulting entity treated as a particle. If it is d_self, the object corresponding to it is considered to be a jet and removed from the list of particles. Finally, all the d_{ij} and d_self are recomputed on updated list of particles and the previously described prescription applied again based on the new minimum distance. This procedure is run until no particles remain. The CMS experiment typically sets $R = 0.4$; this configuration of the anti-k_T algorithm is often referred to as AK4.

2.3 The signals

In this section a few interesting signals at the LHC will be presented. Emphasis will be put on features that can be exploited in the trigger to help distinguish these signals from the background minimum bias interactions.

2.3.1 Electroweak physics

The electroweak theory provides a unified description of the electromagnetic and weak force. Predictions of the theory have always been in agreement with experiments [34]. Increasing the precision of the measured observables is fundamental in order to look for small deviations from their expected values in the theory. Disagreements with experimental data could be caused by physics not included in the standard model, which will be referred to as new physics (NP).

For instance, precision measurements of the properties of the electroweak bosons W and Z and their couplings is an important branch of activity at LHC. These bosons leave a unique signature in the detector which can be used in the trigger, as their visible decay products typically have higher momentum than the particles produced in minimum bias interactions. For instance, Figs. 2.8(a) and 2.8(b) show the p_T distribution of electrons in leptonic decays of W bosons at $\sqrt{s} = 100$ TeV generated by Pythia v8.223 and a breakdown of the inclusive p_T distribution of muons measured by the CMS experiment at $\sqrt{s} = 7$ TeV, respectively. Both W and Z objects tend to produce electrons and muons with p_T higher then that observed in minimum bias events. For instance, most of the reconstructed muons above 30 GeV appear to be produced by W and Z boson decays [55]. Therefore, it is possible to trigger on these events and reject minimum bias interactions by applying a p_T threshold to electrons and muons.

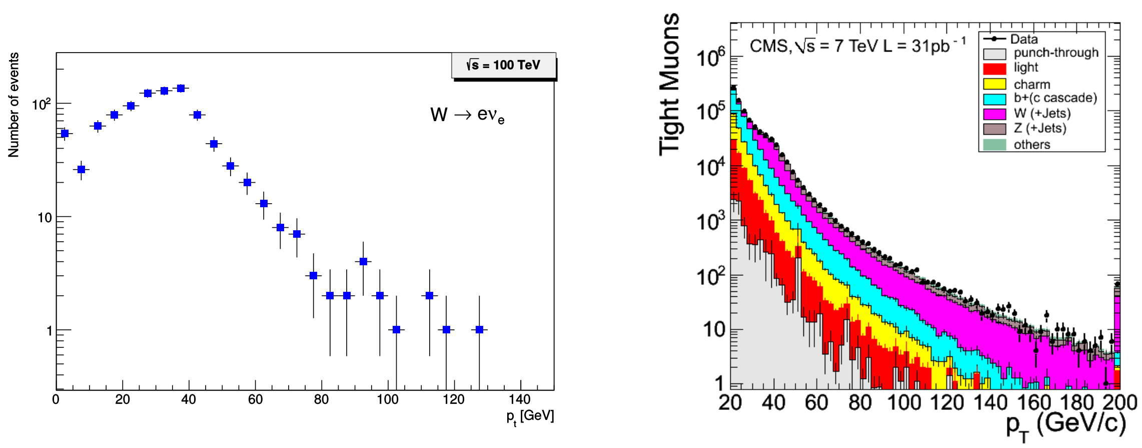

(a) p_T distribution of electrons in 1000 W → $e\nu_e$ events at $\sqrt{s} = 100$ TeV

(b) Breakdown of the inclusive p_T distribution of muons

Figure 2.8: Distribution of the p_T of electrons in 1000 W → $e\nu_e$ events at $\sqrt{s} = 100$ TeV and breakdown of the inclusive p_T distribution of muons in CMS at $\sqrt{s} = 7$ TeV. Figure (b) was taken from Ref. [55].

2.3.2 Higgs sector

The Higgs boson is a scalar boson whose field is responsible for giving masses to the particles of the standard model [34], while retaining the renormalisability of the model. Renormalisation is a procedure that absorbs in observable parameters infinities appearing in perturbative expansions of quantum field theories. A theory is considered renormalisable when the number of parameters required to absorb all the possible infinities of the theory is limited. Renormalisability is fundamental in order to have a theory able to produce useful predictions.

The Higgs field is a complex scalar field. Due to the electroweak symmetry breaking mechanism, the vacuum expectation value (VEV) of the Higgs field is non-zero at energy below the electroweak symmetry breaking scale, $\sim 100-200$ GeV. Masses in the SM arise from the coupling of the particles of the model to the Higgs field. The Higgs boson can interact with all the massive particles, including the boson itself, with a coupling directly proportional to particle mass. Figure 2.9 shows the coupling of fermions and weak bosons measured by the CMS experiment.

The discovery of the Higgs boson [57, 58] is the greatest achievement of LHC experiments at the time of writing. Measuring its decays and couplings, and comparing them to SM is of fundamental importance, as deviations from the predictions could be a sign of NP. Figure 2.10 displays the four dominant production channels of the Higgs boson. Each channel features a peculiar topology that can be exploited to trigger on.

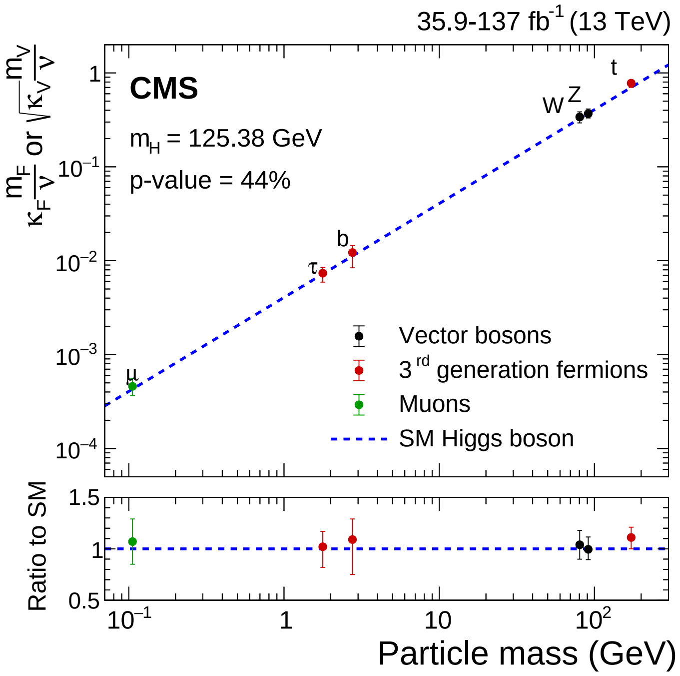

Figure 2.9: Coupling of fermions and weak bosons compared to SM prediction measured by the CMS experiment. Taken from Ref. [56].

The Higgs boson physics programme has strongly driven the design of detectors at LHC and FCC-hh. Figure 2.11(a) shows the η distribution of the most forward lepton in events containing a Higgs boson produced via gluon fusion and decaying into four leptons; Fig. 2.11(b) displays the η distribution of the most forward jet in events containing a Higgs boson produced via vector boson fusion. Reconstructing all the four leptons produced by a Higgs boson decay is necessary in order to successfully reconstruct the boson. Higgs boson production via vector boson fusion is typically associated with jets in the two opposite ends in η, collinear with the collision axis. This is a unique signature that can be detected by reconstructing the two jets in a jet trigger, provided that detectors have sufficient η coverage. The forward hadron subdetector of the CMS experiment covers the $3 < |\eta| < 5$ range [26]; a detector covering up to $|\eta| = 6$ is being studied for FCC-hh, which corresponds to an inner radius of 8 cm at a distance of 16.6 m from the interaction point in the direction of the beam pipe [3].

Higgs boson pair production is another important measurement at LHC. The self-coupling of the boson can be measured through this process, which provides a probe into the shape of the

(a) Gluon fusion

(b) Higgsstrahlung

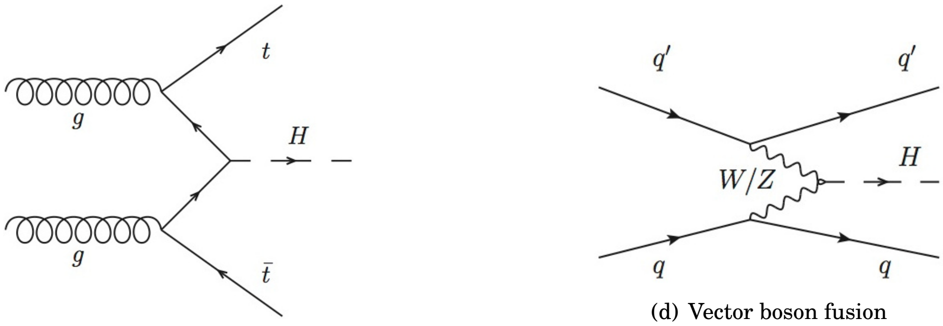

(c) Associated $t\bar{t}$ -Higgs

(d) Vector boson fusion

Figure 2.10: Feynman diagrams of the dominant production channels of the Higgs boson.

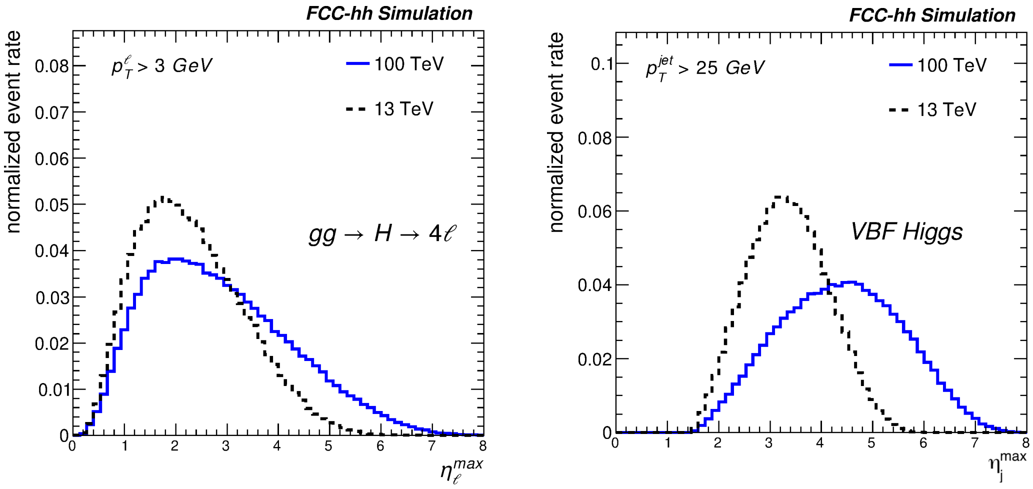

(a) Most forward lepton in a Higgs boson decay into four leptons

(b) Most forward jet in vector-boson fusion Higgs boson production

Figure 2.11: Comparison between proton interactions at $\sqrt{s}$ = 14 TeV and 100 TeV of the pseudorapidity distributions of two Higgs boson production modes. The products are significantly more distributed towards the forward region of the detector at higher energy. Taken from Ref. [59].

Higgs potential and, consequently, the spontaneous symmetry breaking mechanism. This process, however, has an extremely low cross section, around 30 fb at $\sqrt{s} = 13$ TeV [60], requiring large integrated luminosity for its observation. Obtaining a measurement of this process is an important goal of the HL-LHC and FCC-hh experiments.

2.3.3 New physics

The standard model has passed all experimental tests it has been confronted with so far, with an excellent level of agreement between theory and data. The model appears to be complete, as it does not predict any new fundamental particle or physics process. However, there are phenomenon in the universe that the model is not able to explain:

Gravity: the model does not include any quantum-level description of the gravitational force.

Dark matter: data from the rotational speed of visible matter galaxies shows a discrepancy between the tangential velocity and the observed luminous matter, as galaxies appear to rotate faster than expected. This discrepancy can be solved by introducing a new type of non-luminous matter, which does not couple to the electromagnetic force, but that interacts gravitationally called dark matter. The only particle in the standard model that fits with the properties of the dark matter is the neutrino. However, neutrinos appear to be too light to enable formation of structures like stars, and can only represent a portion of the dark matter in the universe [61].

Matter-antimatter symmetry: most of the processes in the SM produce matter and antimatter in equal measure. However, matter is predominant in the universe. Charge conjugation-parity (CP) asymmetry has been observed in the weak sector of SM in the quark mixing, which causes certain decays to prefer matter over antimatter. The contribution from these CP-violating processes, however, appears to be too small to completely explain the prevalence of matter over antimatter [61].

Neutrino mass: neutrino oscillations demonstrate that neutrinos have a very small, but non-zero, mass, with the heaviest mass ~ 100 meV. Mass terms can be implemented in the standard model via a coupling with the Higgs boson, however the model can not explain why the masses of these particles are so small compared to the other constituents of the model.

Hierarchy problem: the mass of the Higgs boson is susceptible to quantum corrections of energy scale up to the Planck mass $m_{\mathrm{P}} \sim 10^{19}$ GeV. These corrections are induced by fermion loops and should cause the Higgs boson to have a much higher mass than observed. An explanation for this is that some numerical cancellation between the Higgs bare mass and the quantum corrections happen to balance out. This is considered to be unnatural as it would require a fine tuning between the corrections and the bare mass terms in order to return observed Higgs boson mass.

Many theoretical extensions to the SM were proposed in order to address these issues. A popular model is supersymmetry (SUSY). Supersymmetry introduces a new supersymmetric partner for each particle in the standard model. The spin of the supersymmetric particles differs from that of their counterparts by half integer, therefore each fermion in the SM has a boson as a supersymmetric partner, and vice versa. The R quantum number is introduced in SUSY: SM particles have $R = 1$ and SUSY particles have $R = -1$. The R number is conserved in some SUSY models, therefore the lightest SUSY particle (LSP) is stable and has the properties required in order to be a dark matter candidate. The supersymmetric particles add new boson loop corrections to the Higgs boson mass that have opposite sign of that of the standard model counterparts. The two corrections can balance out if the masses of the supersymmetric bosons are light enough, thus restoring naturalness to the Higgs boson mass.

No experimental evidence of SUSY has been found so far. In SUSY theories where R is conserved, if a heavy supersymmetric particle is produced, it is expected to generate a decay chain ending with the LSP production, shown in Fig. 2.12(a). The decay chain typically leaves a number of hadron jets and leptons, and a p_{T} imbalance ($p_{\mathrm{T}}^{\mathrm{miss}}$) associated to the LSP, which does not interact with the detector. A trigger on the total scalar sum of the p_{T} of all jets (H_{T}) can be used to provide a robust trigger on this signal that is independent of the number of jets in an event. This trigger can be used in combination with a $p_{\mathrm{T}}^{\mathrm{miss}}$ trigger.

Mono-jet searches are model-independent searches for dark matter particles. If the process producing dark matter particles recoils against a jet, a signature with a jet and $p_{\mathrm{T}}^{\mathrm{miss}}$ is expected. An example of a mono-jet process is shown in Fig. 2.12(b): a neutral mediator, Z$'$, decays into a pair of "invisible" dark matter particles recoiling against a gluon, which produces an hadron jet. Jet triggers are crucial in selecting these events.

2.4 Summary

The standard model describes the way all fundamental particles interact via the strong, weak, and electromagnetic forces. Quarks and gluons have colour charge and can interact via the strong force, modeled by the QCD theory, which is carried by gluons. The strong force has the largest coupling in the model at the interaction energy at which it is typically studied. Processes mediated by this force typically have the highest cross sections at hadron colliders. Non-diffractive scattering between protons, often referred to as minimum bias events, is the main background at hadron colliders that triggers must usually reject. Products of minimum bias events have typically low p_{T} and are uniformly spread over the η range, i.e. are denser closer to the beam pipe. Hadron jets are groups of particles centred around a common axis originating from a quark or a gluon produced in an interaction. The anti-k_{T} algorithm with $R = 0.4$ is the hadron jet

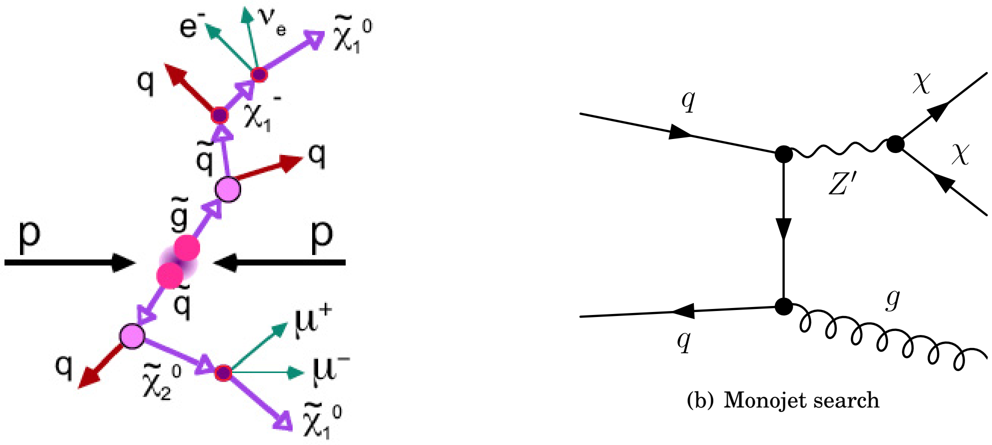

(a) SUSY decay chain

(b) Monojet search

Figure 2.12: Examples of two new physics signatures: a SUSY decay chain and a monojet process associated with dark matter particles. Figure (a) is taken from Ref. [62]; Figure (b) is taken from Ref. [63].

reconstruction algorithm used by the CMS experiment.

Signals associated to electroweak physics, Higgs boson, and new physics are of particular interest at the LHC. These signals typically have unique p_{T} distributions and topologies that allow the trigger to distinguish them from the minimum bias background.

CHAPTER 3

THE LHC AND CMS EXPERIMENTS

A brief overview of the LHC and CMS experiment and their upgrade for the high-luminosity phase will be presented in the first half of this chapter. In the second half the upgrade of the level-1 trigger of the CMS experiment in preparation for the HL-LHC upgrade will be introduced. Emphasis will be put on the particle flow triggers as the original work of this thesis, presented in Chapters 4 and 5, relies on the output of this algorithm.

3.1 The Large Hadron Collider

The Large Hadron Collider (LHC) experiment [24, 64] is a circular proton-proton collider built at CERN in Geneva, Switzerland. At the moment of writing, the LHC is the largest and most powerful particle accelerator ever built. The collider is 27 km long and is located at the border between France and Switzerland. The LHC is able to accelerate protons up to an energy of 7 TeV, corresponding to a maximum centre-of-mass energy $\sqrt{s}$ of 14 TeV. The design $\mathscr{L}_{\text{inst}}$ is 10^{34} cm^{-2} s^{-1}. The first run of the LHC started in 2009 and ended in 2013. Until 2012, the accelerator operated at $\sqrt{s} = 7$ TeV; the energy was then raised to $\sqrt{s} = 8$ TeV. The instantaneous luminosity was progressively increased up to 1.2×10^{34} cm^{-2} s^{-1} over Run 1, and during Run-2 to $\mathscr{L}_{\text{inst}} = 2 \times 10^{34}$ cm^{-2} s^{-1} , corresponding to an average pile-up ($\langle \text{PU} \rangle$), the average number of simultaneous proton-proton interactions per bunch crossing, of 50. This was an excellent result as the instantaneous luminosity exceeded the LHC design value. The centre-of-mass energy was also increased to $\sqrt{s} = 13$ TeV during Run-2, in order to directly search for high-mass resonances and raise the cross-section of interesting physics processes.

Four main experiments are located at four interaction points, shown in Figure 3.1. The ATLAS [25] (A Toroidal LHC ApparatuS) and CMS [26] (Compact Muon Solenoid) experiments are located at

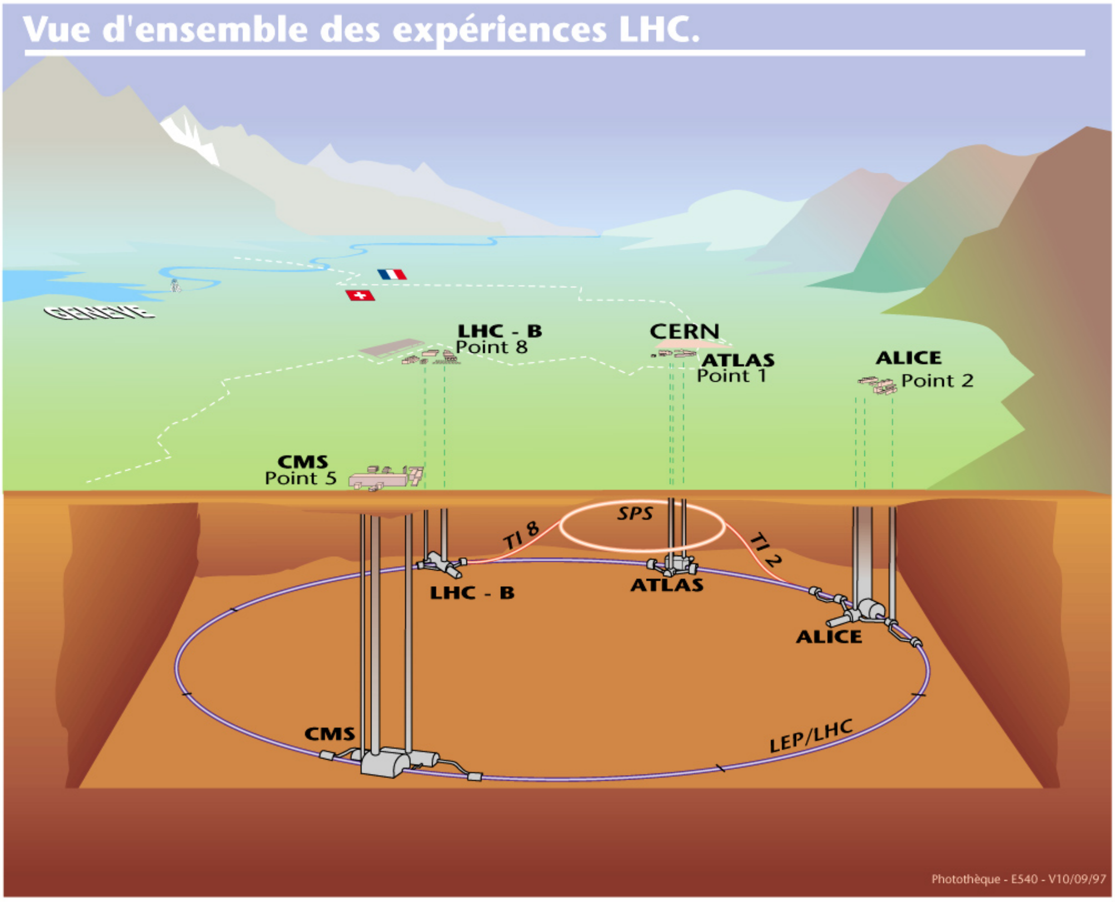

Figure 3.1: Overview of the the LHC experiments, taken from Ref. [65].

interaction point 1 and 5, respectively. They are general-purpose experiments that are designed to detect a wide range of physics processes, ranging from electroweak physics measurements to searches for new particles predicted by supersymmetric models. The LHCb [27] experiment is located at the interaction point 8; its physics goal is to study b quark physics and CP symmetry violations. Finally, the interaction point 2 hosts the ALICE [28] experiment which investigates the properties of the Quark-Gluon Plasma (QGP), a state of matter that manifests itself at extremely high temperature and density. Quark-gluon plasma is obtained at LHC by colliding lead ions in dedicated LHC fills.

3.1.1 The high-luminosity upgrade

By the end of Run-3, the ATLAS and CMS experiments are expected to collect around 300 fb^{-1} each. At this stage, carrying operations at the instantaneous luminosity of 2×10^{34} cm^{-2} s^{-1} will not produce a significant statistical gain on a reasonable timescale. For instance, it is expected that the running time required to halve the statistical error of a given measurement after Run-3

will be over ten years, if the instantaneous luminosity is left unchanged [66]. Consequently, at the end of 2027, the LHC will enter the high luminosity phase, which is referred to as HL-LHC [66]. In this phase the instantaneous luminosity will be increased to 5×10^{34} cm^{-2} s^{-1} , corresponding to $\langle PU \rangle = 140$. In addition, the instantaneous luminosity is planned to further increase to 7×10^{34} cm^{-2} s^{-1} over the years, reaching $\langle PU \rangle = 200$. The extremely high volume of collisions will enable the ATLAS and CMS experiments to record an integrated luminosity between 3000 and 4000 fb^{-1} each. The large dataset will be used to perform high-precision measurements of the standard model and probe increasingly rare new physics phenomena.
To achieve higher luminosity, a large redesign of the CERN's accelerator facilities, such as the injector systems, the kicker and the cryogenics, will be required. In addition, all the LHC experiments will undergo a major upgrade program, which will enable the experiments to maintain sensitivity to interesting physics processes despite the much higher pile-up background.

3.2 The CMS experiment

The CMS detector is located in Cessy (France) at the intersection point 5 of the LHC. A diagram of the Run-1 CMS detector is displayed in Fig. 3.2. CMS is a quasi-hermetic, general-purpose detector that covers the entire azimuthal angle ϕ and pseudo-rapidity η between -5.2 and 5.2. The large solid angle coverage and variety of complementary subdetectors enable CMS to measure a broad range of physics phenomena. Subdetectors are installed in a layered structure where each layer serves a specific function. The layers can be summarised from the inside out as:

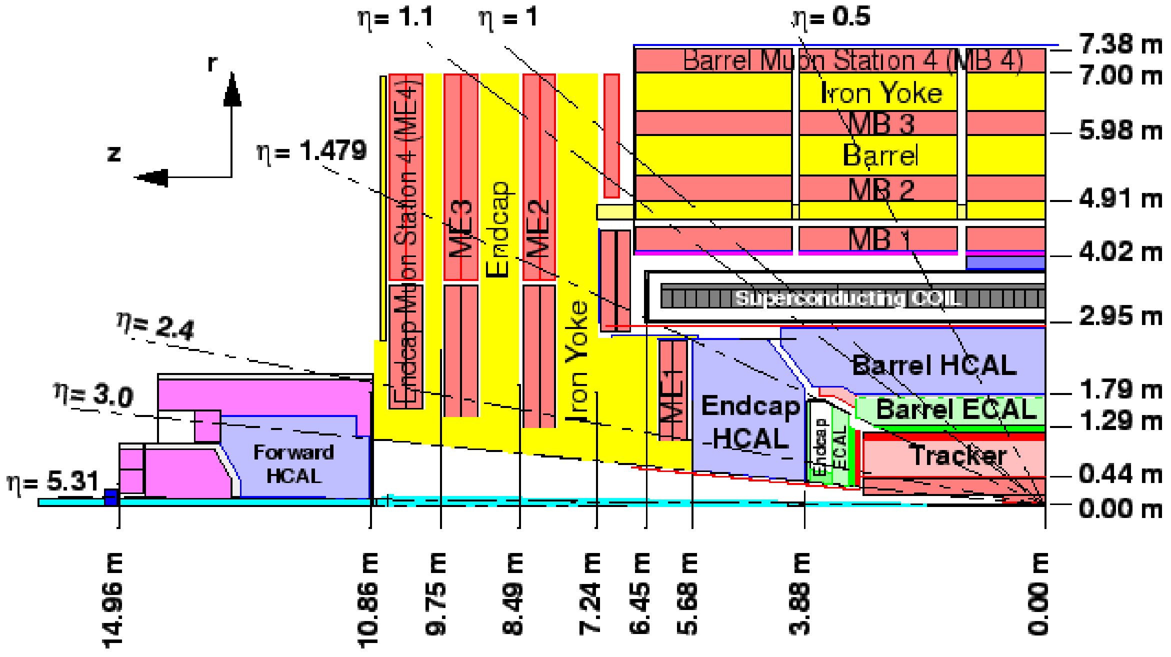

Figure 3.2: Cross-section of the Run-1 CMS detector. Taken from Ref. [67].

Silicon tracker: identifies interaction vertices, reconstructs the tracks of charged particles, whose bending radius due to the magnetic field is used to obtain the associated particle's charge and momentum.

Electromagnetic calorimeter (ECAL): measures the energy of photons and electrons, and contributes to the reconstruction of the charged hadrons.

Hadron calorimeter (HCAL): measures the energy of charged and neutral hadrons.

Superconducting solenoid: produces a 3.8 T magnetic field in the inner part and a 2 T field in the flux return yoke that is used to bend the tracks of charged particles.

Muon chambers: measures the tracks of muons and their momentum in synergy with the silicon tracker.

CMS will be upgraded in view of the HL-LHC upgrade. The upgraded detector is referred to as Phase-2 CMS, in contrast to Phase-1, which is the detector used in Run-2, and Run-3 of LHC. Phase-2 CMS will retain the same layered structure. Many subdetectors will be replaced or upgraded in order to maintain the same reconstruction performance under more demanding pile-up conditions. Most of the electronics front-end and back-end will be upgraded to cope with the increased data rates. In the following sections, both Phase-1 and Phase-2 versions of each CMS layer will be briefly presented.

3.2.1 Silicon tracker

The silicon tracker [68] is used to obtain the tracks of charged particles and infer their momentum and charge. It also identifies the primary vertex. The Phase-1 silicon tracker provides good performance up to $|\eta| = 2.5$. The tracker is composed of two different subdetectors of finer granularity as they approach the interaction point in order to maintain the same track reconstruction performance as the particle density increases. The inner subdetector employs pixel detectors; each pixel is $100 \times 150\ \mu\text{m}^2$ big in the $\phi \times \eta$ directions. Micro strip silicon detectors surround the pixel detectors; the size of each strip increases with distance from the beam pipe.
The Phase-2 upgrade of the tracker [69] will be able to build tracks of particles up $|\eta| = 4$. The inner sector of the tracker will be equipped with silicon pixels $25 \times 100\ \mu\text{m}^2$ or $50 \times 50\ \mu\text{m}^2$ big in $\phi \times \eta$. The outer tracker will be composed of silicon strip pairs, and will be able to provide track stubs built from hit doublets to the trigger. In order to reduce data rates, only stubs above a specific p_T threshold will be sent out. The selection is performed via modules called "p_T modules". A schematic of how the filtering is applied is shown in Fig. 3.3: for each hit, an acceptance window, marked in green in the picture, is created in the second layer; stubs whose second hit is found within the window are considered to have p_T higher than the threshold and sent out. The magnetic field bends the tracks of charged particles; a narrow window corresponds to a higher p_T threshold. A p_T threshold of 2 GeV is sufficient to reduce data rates by an order of magnitude

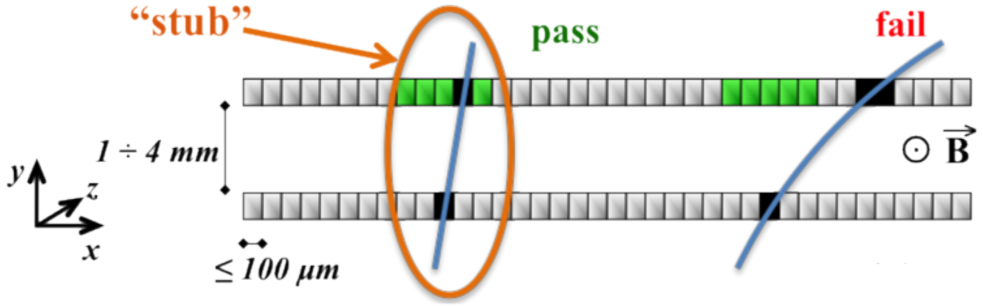

Figure 3.3: Illustration of stub selection by a p_T module. Taken from Ref. [69].

and fit in the bandwidth limits of the system [69].

3.2.2 Electromagnetic and hadron calorimeters

The calorimeters provide an energy measurement of photons, electrons, and charged and neutral hadrons up to $|\eta| = 5$. The barrel, endcap, and forward calorimeter respectively cover the $0 < |\eta| < 1.479$, $1.479 < |\eta| < 3$, $3 < |\eta| < 5$ ranges.

The barrel and endcap ECAL [70] are equipped with scintillating $PbWO_4$ crystals of size 0.0174×0.0174 in $\eta \times \phi$. Crystals in $PbWO_4$ were chosen as an active material for their radiation resistance, density (8.28 g/cm^3), radiation length ($X_0 = 0.89$ cm), and Molière radius (2.2 cm). These properties altogether ensure that ECAL is able to contain and measure an electromagnetic shower in a confined space. In addition this material produces around 80% of the scintillation photons within 25 ns, providing good time resolution.

The barrel and endcap HCAL [71] is a sampling calorimeter composed of alternating layers of plastic scintillators and brass, which was chosen as an absorber material due to its non-magnetic properties. The forward hadron calorimeter (HF) uses quartz fibers and steel absorbers to measure the energy of hadrons via the Cherenkov effect.

The endcap calorimeter will have absorbed a significant amount of radiation by the start of HL-LHC operations and will be replaced by the High Granularity Calorimeter (HGCAL) [72] in the Phase-2 upgrade. HGCAL is a sampling calorimeter with a fine segmentation in both longitudinal and transverse direction, enabling accurate 3D positioning of energy deposits. A cross section of the upgraded endcap calorimeters is displayed in Fig. 3.4. The subdetector is divided into electromagnetic and hadron sections. The former is composed of 28 absorber layers in tungsten and copper alternating with silicon as active material; the latter consists of 12 absorbers layers in brass and copper interleaved with silicon sensors in the front section, and highly-segmented plastic scintillators in the rear section.

The reconstruction performance of the CMS detector will greatly benefit from the high granularity information. The high-density of the calorimeter will cause showers to be contained in a small

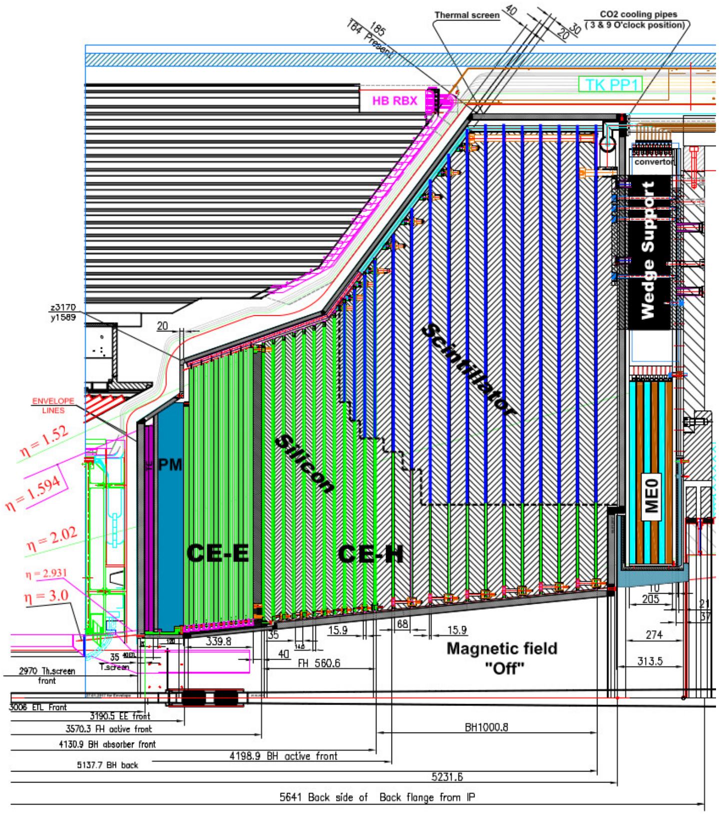

Figure 3.4: Longitudinal cross section of HGCAL. The electromagnetic section is labelled with CE-E, the hadron section with CE-H. The green area employs silicon detectors and the blue one makes use of plastic scintillators. Taken from Ref. [72].

region, which is fundamental in order to prevent overlap between energy deposits coming from different objects in the congested environment of the HL-LHC. The longitudinal and transverse structure of the energy deposits will be used to discriminate between electromagnetic showers, taus, jets and pile-up.

3.2.3 Muon chambers

The muon chambers [73] employ gaseous detectors to reconstruct tracks of muons exiting the inner part of the detector. Muons are minimum ionising particles that do not get stopped by the detector. Therefore, their momentum is obtained from the curvature of the track left in the tracker and the muon chambers. A magnetic field strong enough to produce a measurable effect on tracks outside the solenoid is ensured by a iron yoke, in which the muon chambers are located. The yoke also serves the purpose of containing the magnetic field. The barrel muon chambers, covering up to $|\eta| = 1.1$, employ drift tubes (DT) and resistive plate chambers (RPC). The endcap muon chambers cover the $1.4 < |\eta| < 2.4$ range and consist of RPCs and cathode strip chambers (CSC).

Three main upgrades to the muon detectors are expected for the Phase-2 of the experiment [74]. The existing muon detectors will be upgraded for longevity. Gas electron multiplier (GEM) detectors will be added in the endcap region for redundancy and to improve the track reconstruction performance [75]. The coverage of the endcap muon detector will be extended up to $|\eta| \approx 3$.

3.3 The Level-1 Trigger

The level-1 trigger (L1T) of the CMS experiment will be presented in this section. A short overview of the entire architecture of the trigger system will be given. The L1T system used during in the Phase-1 of the CMS experiment will be then introduced. The Phase-2 upgrade of the system will be described, with particular attention to the particle flow implementation.

3.3.1 Overview of the CMS trigger system

Figure 3.5 shows a diagram of the CMS trigger system [76, 77]. Data produced by the detector every bunch crossing is digitised and stored on front-end pipelines. A subset is processed to produce trigger primitives (TPs). TPs are used to build a coarse granularity version of the event that requires less bandwidth and can be sent every bunch crossing to the level-1 trigger. Within a few µs the L1T analyses the TPs on electronic boards, and issues an accept or reject signal to

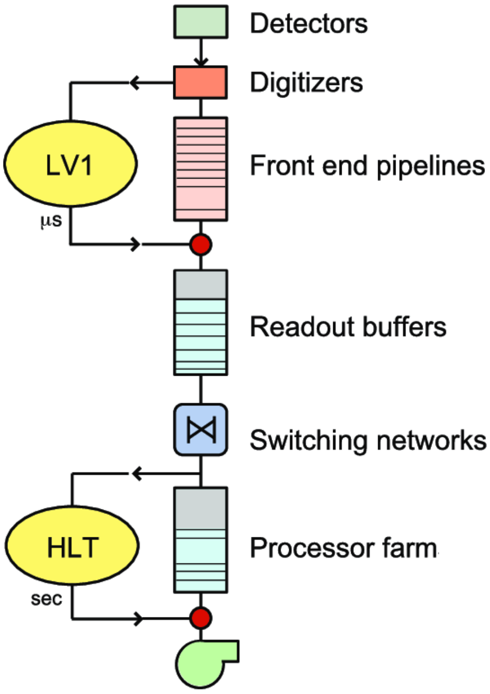

Figure 3.5: Diagram of the CMS trigger system. Taken from Ref. [77].

the front end buffers. The decision on whether to accept or reject an event is based on a trigger menu, i.e. a set of algorithms that define the criteria for which an event is considered interesting. An accept signal causes the front end buffer to send the full-event data to the event builder network. The event builder network collects data from all the detector data sources and combines them together to form a single event entity that is sent to the CMS computing services. Here, a high-level trigger (HLT) runs offline reconstruction algorithms on a computing cluster. A set of progressive filters is run in order to further select events in the time scale of a second on average. Finally, events accepted by the HLT are sent to the CERN computing centre and stored for offline analysis.

3.3.2 The Phase-1 Level-1 Trigger

The Phase-1 level-1 trigger was commissioned in 2015 and 2016, upgrading the Run-1 L1T in order to maintain the Run-1 physics acceptance at the increased luminosity and rates of Run-2 [78]. The system consists of around 100 hardware boards that process around 5 Tb/s of data. This information is used to reduce the detector readout rate from 40 MHz to a maximum of 100 kHz. The system must complete processing of an event within 3.8 µs, determined by the size of the front end buffer, and be ready to process new data every 25 ns.

3.3.2.1 Architecture

A diagram of the architecture of the Phase-1 L1T is displayed in Fig. 3.6. The system is split in two separate sections, one processing inputs from the muon systems and one from the calorimeters. The muon trigger is organised in three different subsystems, each one processing muon hits in a specific η range. The barrel muon track finder (BMTF) find tracks in the $|\eta| < 0.8$ region of the detector, where muons only hit the DTs and RPCs in the barrel. The overlap muon track finder (OMTF) processes data in the $0.8 < |\eta| < 1.25$ region, which corresponds to the overlap between the barrel and the endcap muon detectors. The endcap muon track finder (EMTF) reconstructs muon tracks in the $|\eta| > 1.25$ range, corresponding to the area uniquely occupied by the endcap muon detectors. Muon tracks are found by running pattern matching algorithms. A new algorithm, based on a Kalman filter [79], will be deployed in the BMTF for Run-3 of CMS, improving the reconstruction performance in the corresponding η range.

The calorimeter trigger receives calorimeter towers, i.e. energy deposited in a group of ECAL crystals and the HCAL tower behind them. The calorimeter trigger is organised in a two-layer structure and uses time-multiplexing to process data from a single event in a single board [80]. An example of time multiplexing is shown in Fig. 3.7. In a time multiplexed trigger of period N, a multiplexing layer sends data from every N-th event to a specific board. In order to constantly process new events, N boards are required. Data from consecutive events are sent to consecutive boards in a round-robin fashion. In the calorimeter trigger, a time multiplexing period of 9 is used. The first layer serves as a multiplexing stage. The second layer finds calorimeter objects

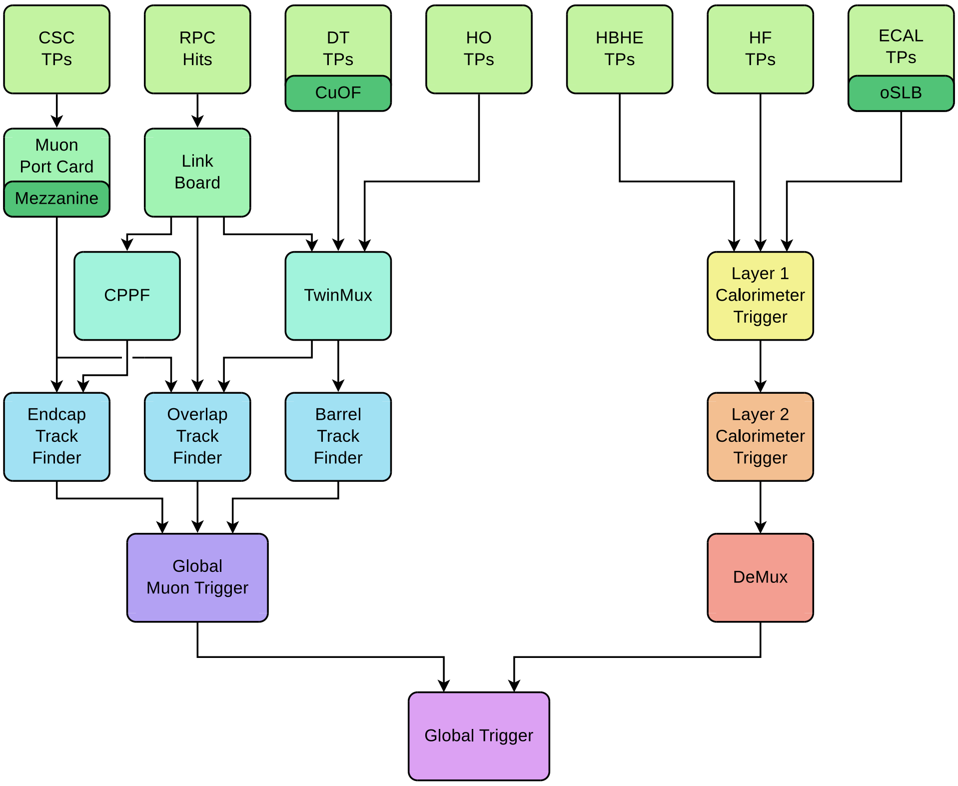

Figure 3.6: Architecture of the Phase-1 L1T. Taken from Ref. [78].

and computes energy sums, e.g. hadron jets and $p_{\mathrm{T}}^{\mathrm{miss}}$. The output is sent to a demultiplexing stage which takes care of sorting the objects and transmitting those with highest energy to the global trigger.

The global trigger (GT) runs a set of selection requirements called the “trigger menu”. These selections range from single-object p_{T} thresholds to complex object correlations involving several trigger objects. The GT can run up to 512 selections in parallel. In the final stage, the GT computes a final logical OR on the output of all selection criteria to determine whether to issue an accept signal.

3.3.2.2 Technologies

The Phase-1 L1T consists of a pipeline of electronic boards that communicate with each other via high speed optical links. This is required in order to fit into the latency and bandwidth constraints of CMS. High-throughput algorithms are run on FPGAs, integrated circuits that can be programmed in the field after production. FPGAs contain configurable logic blocks (CLBs), digital signal processors (DSPs), and memory blocks. A diagram of a simple four-input CLB is shown in Fig. 3.8: configurable logic blocks contain look-up tables (LUTs) and flip-flops (FFs). LUTs are volatile memory units that are configured only once during the initial FPGA programming

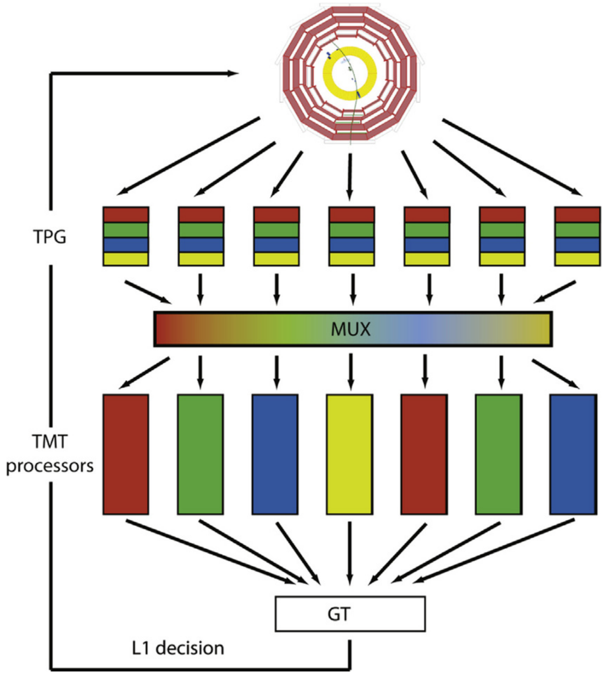

Figure 3.7: Example of time multiplexing with a period of 7. A multiplexing layer sends every seventh event to a specific board. In order to constantly process data consecutive events are distributed to consecutive boards in a round-robin fashion, requiring for seven boards in total to keep processing new data. Taken from Ref. [81].

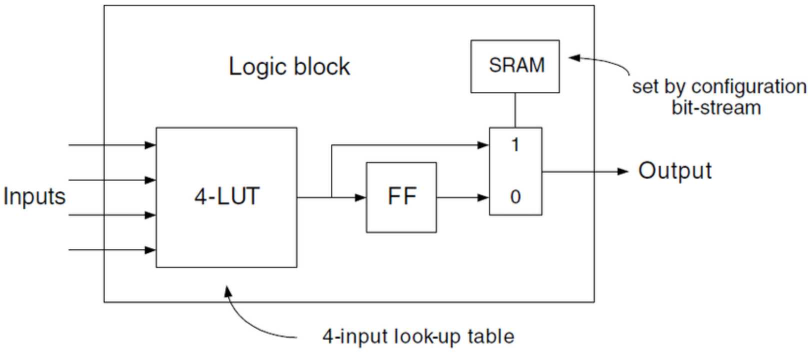

Figure 3.8: Diagram of a simple configurable logic block with four inputs. Taken from Ref. [82].

stage. They are typically used to implement combinatorial logic by loading the corresponding truth table into memory. FFs are devices able to store a logical bit and are typically used to store and synchronise data at the end of a clock cycle. High-end FPGA such as the Xilinx Virtex Ultrascale FPGAs, contain powerful CLBs consisting of eight 6-input LUTs and 16 FFs [83]. DSP cores are units typically used to process digital signals. They can perform a variety of arithmetic and logic operations, e.g. multiplications. Complex algorithms can be implemented on FPGAs by programming and connecting its components to form a circuit performing the logic of the algorithm. FPGAs have the processing power advantages of a circuit and can be reprogrammed at any time, enabling bugs to be fixed or additional features to added at a later stage.

Standardisation is paramount in the L1T design in order to limit maintenance costs. Its hardware boards are based on the μTCA (Micro Telecommunications Computing Architecture) standard [84]. A generic and flexible processing element was obtained by equipping boards with a large number of high-bandwidth input/output links and large FPGAs (Xilinx Virtex 7). Based on this model, three board variants were implemented, each one optimised for a specific task:

Calorimeter Trigger Processor v7 (CTP7): a card optimized for data sharing within a single crate. Designed for the calorimeter layer-1, where data exchange in the same crate is required to prepare data for time multiplexing.

Master Processor v7 (MP7): a card optimized for data processing and sharing via a large number of optical inputs and outputs. Designed as a generic data processing board for a variety of applications.

Muon Track Finder v7 (MTF7): a card with large look-up tables optimized for the muon trigger, where large memory banks are required to store information necessary to correctly reconstruct muon tracks.

3.3.3 The Phase-2 Level-1 trigger

The Phase-1 L1T is expected to have an accept rate of 1500 kHz if the same trigger menu and algorithms are kept at $\mathscr{L}_{\text{inst}} = 5 \times 10^{34}\ \text{cm}^{-2}\ \text{s}^{-1}$ [85]. This rate would increase to 4000 kHz at $\mathscr{L}_{\text{inst}} = 7 \times 10^{34}\ \text{cm}^{-2}\ \text{s}^{-1}$. It is impossible for the CMS detector to operate and successfully acquire data under these conditions without raising the trigger thresholds and critically compromise its physics reach. The main objective of the Phase-2 upgrade of the L1T is to maintain and potentially expand the physics acceptance of the CMS experiment at the higher luminosity conditions of HL-LHC while remaining within the bandwidth limits of the detector. This is achieved by introducing in L1T a track trigger and high granularity 3D TPs from HGCAL [31], which drastically improve the reconstruction performance of the system. In addition, the readout of the pre-existing subdetectors is upgraded to handle higher L1T accept rates. The Phase-2 L1T consists of around 500 boards that analyse an input data rate of 50 Tb/s. The maximum accept rate will be increased to 750 kHz and the maximum latency to 12.5 µs. These improvements

enable the Phase-2 L1T to maintain a physics acceptance similar to the Phase-1 system with an accept rate of 260 and 500 kHz at an instantaneous luminosity of 5×10^{34} and 7×10^{34} $\mathrm{cm}^{-2}\,\mathrm{s}^{-1}$, respectively [85].
The Phase-2 L1T is able to compute two types of objects:

Standalone objects: objects reconstructed by using data from a limited set of subdetectors, e.g. from only the calorimeters;

Particle flow objects: objects found using the particle-flow (PF) algorithm [86], further details on the algorithm will be given in Section 3.3.3.3

The redundancy enables the L1T to be more robust in case of issues. Having track information enables the system to run the pileup per particle identification (PUPPI) algorithm [87] for pile-up subtraction, making PF objects extremely resilient to the harsh pile-up conditions of HL-LHC. The PUPPI algorithm will be briefly presented together with PF algorithm in Section 3.3.3.3.

3.3.3.1 Architecture

The diagram in Fig. 3.9 represents the architecture of the Phase-2 L1T system. Three main branches receive and process inputs from a set of subdetectors. The calorimeter trigger receives

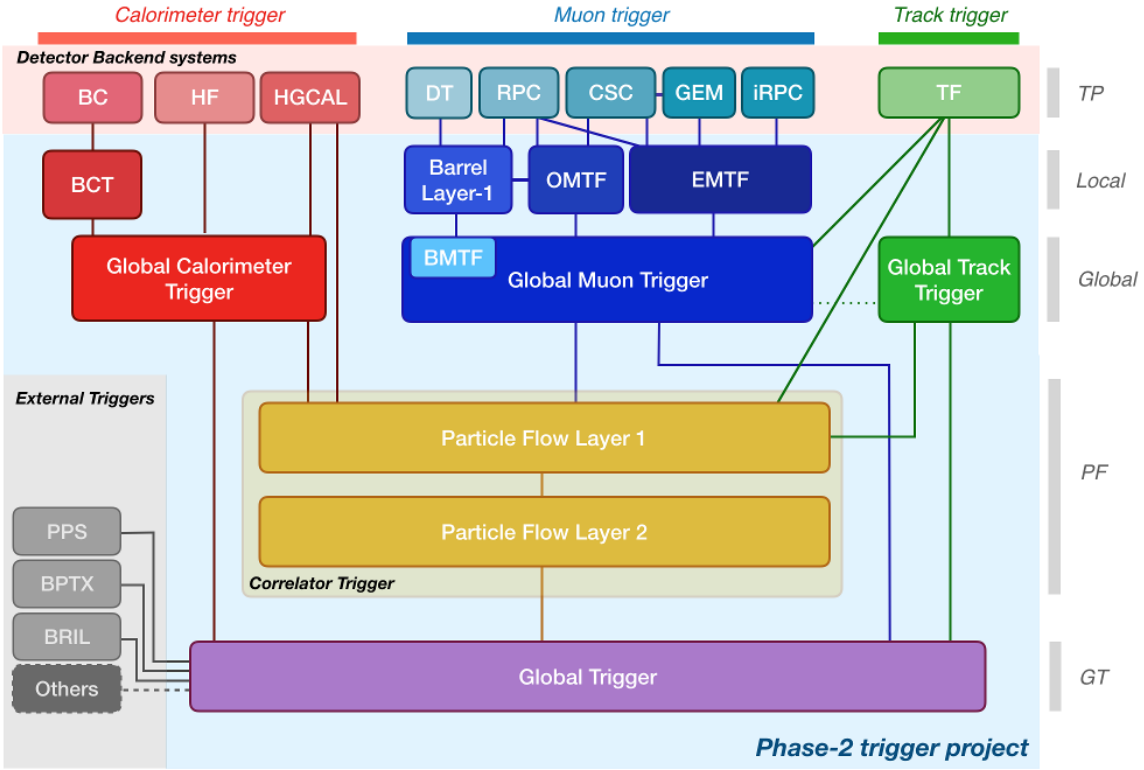

Figure 3.9: Architecture of the Phase-2 upgrade of the CMS L1T. Taken from Ref. [31].

input from the barrel ECAL and HCAL, the HGCAL, and HF. The barrel calorimeter trigger (BCT) combines data from the barrel calorimeters to form clusters. Clusters from the BCT are sent together with HGCAL clusters, which are computed by the HGCAL backend, to the global calorimeter trigger (GCT). The GCT computes calorimeter-only standalone objects and energy sums.

The muon trigger is organised, as in the Phase-1 system, in barrel, overlap, and endcap muon track finder. The global muon trigger (GMT) receives standalone muons and muon tracks. The GMT removes muon duplicates and misreconstructed muons. In addition, it computes track-matched muons by matching tracks in the muon chambers to the ones in the tracker. Tracks are matched by propagating the trajectory of particles in the tracker to the muon chambers.

The global track trigger (GTT) receives tracks that are computed by the tracker backend. It identifies the primary vertex in an event and computes hadron jets and energy sums only using the received tracks.

The three branches send their standalone objects to the global trigger (GT). Tracks, clusters, muons, and the primary vertex position are transmitted to the correlator trigger (CT). The CT is at the centre of the Phase-2 L1T and reconstructs objects with the PF algorithm using inputs from all subdetectors. The subsystem can also run the PUPPI algorithm to subtract pile-up. Further details will be given in Section 3.3.3.2.

Finally, the GT receives objects from the GCT, GMT, GTT, and CT and runs a trigger menu to make a decision on whether to accept the event.

3.3.3.2 The correlator trigger

The CT combines inputs from all the trigger subsystems to obtain the best possible reconstruction performance in the L1T. The system is organised in two layers, both using time multiplexing with a period of six bunch crossings. The first layer reconstructs single particles and subtracts pile-up using the PF and PUPPI algorithms. It is composed of 36 boards, six of them processing a single event in parallel. The $|\eta| < 3$ range of each event is split in regions; each board processes a set of regions. Particle flow and PUPPI in the $3 < |\eta| < 5$ range, which is not covered by the tracker, are run in the GCT and the output sent to the first layer of the CT. These objects are then forwarded to the second layer together with the objects found in the $|\eta| < 3$ range.

The second layer reconstructs trigger objects from particles found by the first layer and consists of 30 boards, five of them processing a single event. Each card receives the full list of PF inputs found in the first layer and finds a specific set of objects. The organisation of the algorithms has not been defined, at the moment of this writing. It is expected, however, that the hardware resources will be enough to easily accommodate the following algorithms:

1. Jets
2. Energy sums

3. Taus
4. Electrons and photons, with and without isolation
5. Muons using particle flow, with and without isolation

It is likely that even after implementing these algorithms there will be space to implement additional features, if required. Objects found by each board type are sent to the GT for the final decision.

3.3.3.3 The particle flow and PUPPI algorithms

The particle flow algorithm [86] reconstructs individual particles in an event by using an optimized combination of all subdetector information. The PF algorithm has been adopted by CMS as the flagship offline reconstruction algorithm. The Phase-2 L1T upgrade will introduce high granularity information from calorimeters and tracks that will enable an implementation of a similar algorithm in the L1T for the first time.

Particles are identified by the PF algorithm as either electrons, photons, charged hadrons, neutral hadrons, or muons based on the unique signature left in the detector. Figure 3.10 summarises how each particle type interacts with the CMS detector: electrons produce tracks in the tracker and deposit their energy in the ECAL; photons do not leave a track and interact with the ECAL; charged and neutral hadrons leave most of their energy in the HCAL, the former also interacts with the tracker; muons are minimum ionising particles and are the only ones that can reach and interact with the muon chambers, in first approximation. The PF algorithm computes the particle direction and energy based on the object type.

The initial step of the PF algorithm is muon identification. Track-matched muons found in the GMT are promoted to PF muons and their track removed from further processing. Energy clusters in the calorimeter are, then, computed and classified using machine learning techniques in either electromagnetic, hadronic or from pile-up interactions based on their shape, energy, and ratio between energy in the electromagnetic and hadron section of the calorimeter. These clusters will be referred to as **particle flow clusters**. PF clusters of electromagnetic type are associated to nearby tracks. Based on the p_{T} difference between PF clusters and the relative tracks, clusters can be tagged as electrons, overlapping electrons and photons, or be ignored if they appear to be produced by an hadron shower initiating in the ECAL. Remaining electromagnetic PF clusters that have no nearby tracks are classified as photons, while those with an associated track are merged with the hadronic-type PF clusters to form new hadronic clusters. These clusters are matched to tracks that are in the vicinity if they have compatible p_{T} . Hadronic clusters with an associated track are labelled as charged hadrons, otherwise as neutral hadrons. In the HF, where no tracks are available, every PF cluster is classified as either photon or neutral hadron based on the type.

PUPPI removes particles coming from pile-up vertices by using information on the primary

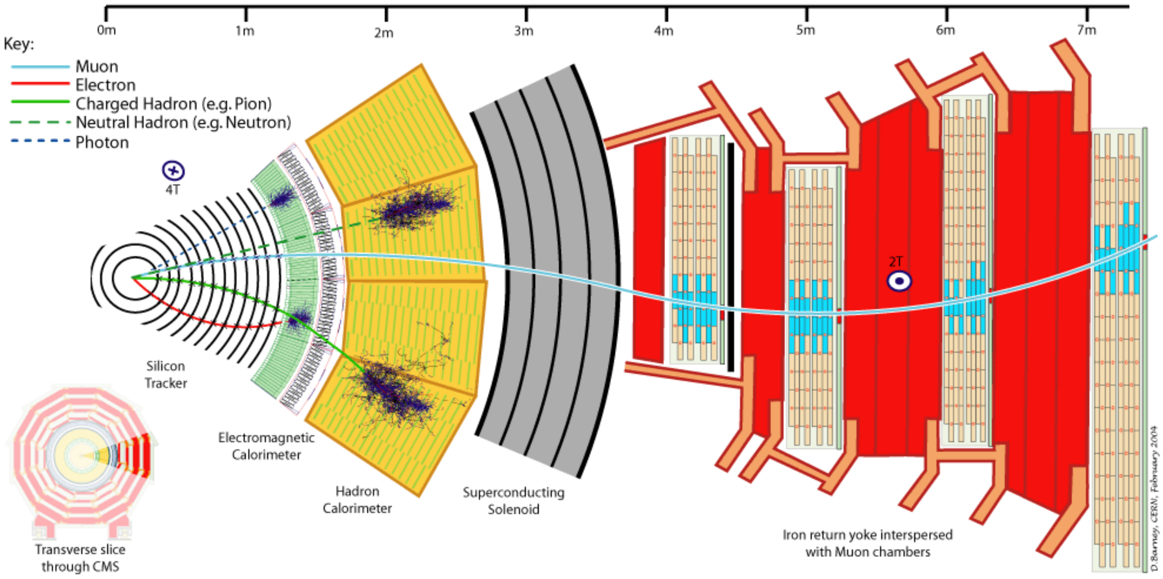

Figure 3.10: Transverse slice of CMS showing how different particles interact with the detector. Taken from Ref. [88].

vertex received from the global track trigger. Charged particles not originating from the primary vertex are removed. The momentum of neutral particles is scaled based on the probability to originate from the primary vertex. This probability is computed for each neutral particle based on its p_{T} , and the p_{T} and distance of all charged particles within a cone of a specific radius from the neutral one. In the forward section of HGCAL and HF, which are not covered by the tracker, every particle is treated as a neutral particle. A probability similar to the previous one is computed based on all the particles surrounding the one under consideration, instead of only the charged ones. The particles obtained from the PF and PUPPI algorithm will be referred to as **particle flow candidates**.

3.3.3.4 Technologies

The newest technologies were used in the Phase-2 upgrade to design a reduced set of generic boards able to serve a large variety of uses. Boards will follow the ATCA (Advanced Telecommunications Computing Architecture) standard [89] and will be equipped with large FPGAs and high-speed optical links. Serenity and Advanced Processor, shown in Fig. 3.11 are the two main R&D hardware platforms that are being studied. Both are equipped with around 100 optical links running up to 28 Gb/s. Xilinx VU9P FPGAs are being considered as main processing component for both boards.

Serenity is the hardware platform on which the jet trigger presented in Chapters 4 and Chapters 5 was developed. It is a flexible and modular data-processing board that hosts FPGAs via daughter cards. This solution enables a large variety of FPGAs of different form factors to be used,

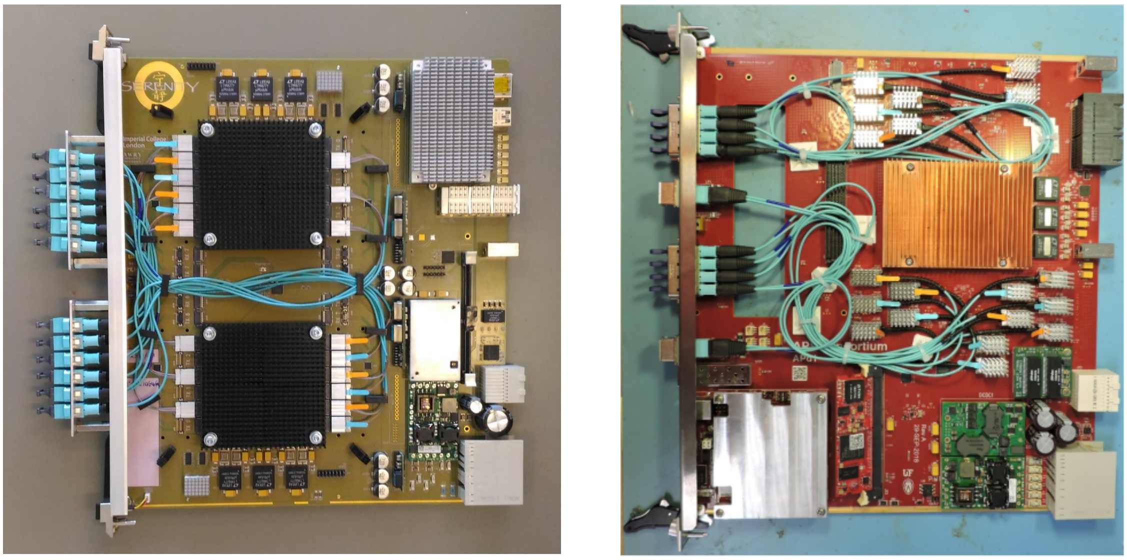

(a) Serenity

(b) Advanced Processor

Figure 3.11: Pictures of the Serenity and Advanced Processor prototype boards. Courtesy of the Serenity and Advanced Processor consortiums.

as daughter cards can be adapted to match the application requirements, and prevents FPGAs from being damaged during manufacturing and testing of the motherboard. The motherboard provides services such as power, clock, and interfaces to the optical links, and hosts a CPU via a COM Express type-10 computer-on-module [90] for higher-level control and monitoring of the device. An Artix-7 FPGA on the motherboard interfaces the control CPU to the on-board components. The board control and monitoring system is provided by the SMASH (Serenity MAnagement SHell) framework which is configurable in order to adapt to the different hardware configurations. The EMP framework (Extensible Modular (data) Processor framework) [91] provides access to board services, such as optical links, memory buffers, or clock, to the algorithms loaded on the processing FPGA. The framework provides a general and configurable firmware infrastructure that simplifies development of trigger algorithms. The setup separates data processing and board infrastructure firmware, allowing developers to focus only the former.

3.4 Summary

The high-luminosity upgrade of the LHC will collide protons at $\sqrt{s} = 14\ TeV$ and $\mathscr{L}_{\text{inst}}\ \ 5 \times 10^{34}$ cm^{-2} s^{-1} . The CMS experiment will be upgraded to retain its physics sensitivity despite the larger background. The level-1 trigger will be completely replaced by a new system equipped with large FPGAs and high-speed optical links running up to 28 Gb/s. The system will receive fine granularity inputs from the calorimeters, and tracks from the tracker and muon chambers. The correlator trigger is a subsystem of the L1T that will run the particle flow algorithm to identify single particles in an event and powerful pile-up subtraction techniques to reject those not produced in the hard interaction vertex.

CHAPTER 4

DESIGN AND STUDY OF A JET AND SUM TRIGGER ALGORITHM

As presented in the previous chapter, the goal of the Phase-2 upgrade of the L1T of the CMS detector is to be able to maintain and potentially expand the physics reach of the experiment at an instantaneous luminosity which is 3-4 times larger than at LHC. The new system uses state-of-the-art hardware to process a large volume of high-granularity inputs. The improved granularity and hardware enables a variety of powerful and sophisticated algorithms to be run, such as particle flow [87]. At the time of this work, some of these algorithms were being studied and developed, others were still to be. In particular, an algorithm to reconstruct hadron jets and compute the $p_{\mathrm{T}}^{\mathrm{miss}}$ and H_{T} energy sums from the particle flow inputs was not available. Until then, most of the trigger upgrade studies were performed by running the AK4 algorithm on the particle flow inputs, as a proxy for an actual jet trigger algorithm. In this chapter, the design and performance of a jet and sum trigger algorithm for the upgrade of the CMS Phase-2 L1T will be presented.

An overview of how a trigger algorithm is developed will be first described in Section 4.1. The Phase-1 jet and sum algorithm, which is not part of the original work of this thesis and was used as a basis, will be presented in Section 4.2. The Phase-2 jet and sum algorithm will be introduced in Section 4.3. Its performance will be presented in Section 4.4, alongside with the impact on the trigger menu of the upgraded L1T. Finally, conclusions and possible improvements will be discussed in Section 4.5.

4.1 Overview of the development of a trigger algorithm

Developing and optimising a trigger algorithm is a complex procedure that requires multiple steps and iterations. Algorithms must be designed bearing in mind the timing, bandwidth, and hardware constraints of the trigger system. FPGAs have limited computing capabilities as operations as multiplication and division can be computationally expensive. In addition, the trigger system is a synchronised system, and algorithms running on the L1T boards must be able to produce results after a fixed amount of time, ruling out methods that have indefinite length and complexity. This often implies that the L1T can not run simple adaptations of reconstruction algorithms that are used in offline analyses.

Once an algorithm has been designed, its performance needs to be studied. More specifically, two different aspects must be analysed: the reconstruction performance and the FPGA hardware usage. Looking at the former means verifying that the algorithm provides satisfactory reconstruction capabilities. This is typically done using GEANT4 [92] simulations of the CMS detector. Studying the usage means estimating the amount of resources taken by the algorithm on the FPGA to ensure it can physically fit on the target hardware, and making sure processing meets the timing constraints of the trigger. The two performance aspects are not studied independently: often new unforeseen constraints are found during firmware development, causing the algorithm to adapt to them and prompting a new study of its reconstruction performance. Therefore, multiple iterations are typically required in order to obtain an optimal algorithm.

The final step of the algorithm development is validation. Typically, physics studies are performed in an emulator of the trigger in the CMS simulation framework. FPGA firmware is written in a different software language, and is typically harder to write and prone to bugs. Therefore, the final stage involves verifying that both hardware and emulator produce identical results starting from the same inputs. This step enables testing the trigger algorithm before deploying it and ensuring its behaviour is well-understood.

This chapter will focus on the implementation in the CMS GEANT4 simulation of the jet and sum algorithm, and the study of its physics performance. The next chapter will focus on the implementation on FPGA of the same algorithm, the study of its hardware performance, and the validation with the emulator.

4.2 The Phase-1 jet and sum algorithms

The AK4 jet finding algorithm, the algorithm used by CMS during offline reconstruction, has a variable computing time that depends on the number of inputs. Therefore, it cannot be run on the trigger without modifications and an alternative jet clustering algorithm has to be developed. The ideal jet algorithm has similar performance to AK4, but constant computing time. The jet trigger algorithm implemented in the Phase-1 L1T [93] was used as a base idea to build the Phase-2 version. The Phase-1 jet algorithm finds jets by building fixed-size squares centred on a seed, i.e. a trigger tower (TT) that is a local maximum. A trigger tower corresponds is a $\eta - \phi$ area in the calorimeter that combines input from both ECAL and HCAL in a single entity. Its size is 0.087×0.087 in the $\eta \times \phi$ space in the barrel, corresponding to a group of 5×5 ECAL crystals packed together with the HCAL tower behind. Mechanical constraints causes the tower size to become bigger in the endcap and forward region. Seeds must have $p_T > 4$ GeV, and satisfy the inequality mask in Fig. 4.1 to find local maxima while preventing double counting and self vetoing of jets. The preliminary jet p_T is given by computing the sum of the p_T measured in a 9×9 TT square centred on the seed. The square size in the barrel calorimeter, 0.783×0.783, matches the average area covered by the anti-k_T algorithm with a ΔR parameter of 0.4. The window becomes larger in the endcap and forward detectors due to increasing TT size.

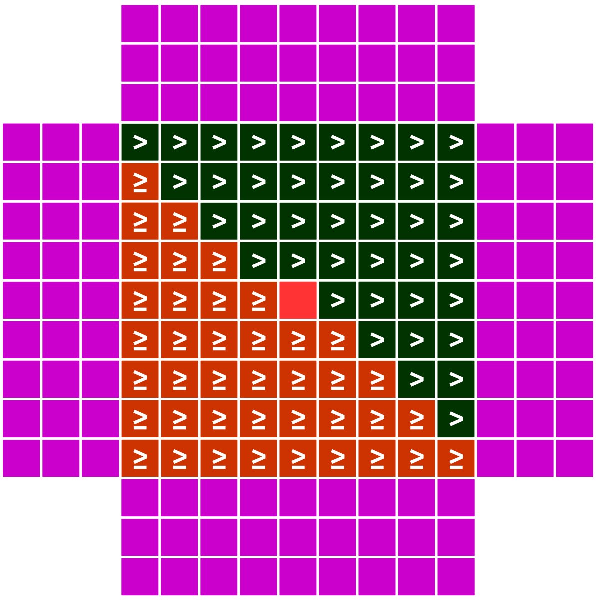

Figure 4.1: Inequality mask that is applied to each trigger tower to identify a seed. The purple area represents the area that is studied for pile-up sampling and subtraction.

The Phase-1 jet algorithm estimates and removes pile-up energy from jets. The energy surrounding the jets is sampled and subtracted to provide a dynamic correction that reliably works on a range of pile-up conditions. The p_T in the four 9×3 strips around the jet, shown in purple in Fig. 4.1, is computed. The total p_T contained in the three lowest strips is subtracted from the jet p_T . Discarding the highest strip enables rejection of fluctuations produced by the presence of other nearby jets. Finally, jets are calibrated based on their p_T and η to compensate for differences in the response of the detector which varies depending on the material traversed by the particles and their energy.

In addition, the algorithm computes a variety of energy sums. Amongst those, it calculates the missing transverse energy, E_T^{miss}, using TT information, and the total scalar transverse energy, H_T, of all jets whose $p_T > 30$ GeV. The sine and cosine trigonometric functions required in order to compute E_T^{miss} are implemented on FPGAs by storing their values in LUTs, to save hardware resources.

4.3 The Phase-2 jet and sum algorithms

The Phase-2 jet algorithm - dubbed the “histogrammed jet algorithm” - uses a fixed-window jet clustering algorithm centred around a seed, which is very similar to the Phase-1 algorithm. The algorithm was designed to run in the second layer of the correlator trigger subsystem to reconstruct jets using particle flow candidates as input. An explanation of the particle flow objects in the trigger is available in Section 3.3.3.3. The algorithm is quite generic and adaptable, therefore its performance using input from only the calorimeter was explored as a sideline, to understand how it would need to be adapted in case of usage in the calorimeter trigger. Particle flow clusters were used as input in this scenario.

The algorithm creates pseudo trigger towers by building a 2D histogram in $\eta-\phi$ space using the p_{T} of the particle flow input as a weight. Seeds are found by applying a similar logic to the Phase-1 jet trigger. Multiple jet sizes were investigated. A preliminary study presented in the HGCAL Technical Design Report [72] showed that using smaller jet size than $\approx 0.8\times0.8$ may provide better performance at high $\langle\mathrm{PU}\rangle$, as it can give a better compromise between including jet energy and excluding pile-up contributions. Bin widths and number of bins used to create the clustering window were changed to find the optimal jet size. The following configurations were investigated for jets built using PF clusters, the label that will be used to refer to them is highlighted in bold:

Phase-1 jets: inputs were binned using an histogram that reproduces the segmentation of the Phase-1 calorimeter trigger towers. Jets were clustered using 9×9 bins.

Phase-1 with pile-up subtraction jets (PUS): same as the Phase-1 configuration, with the addition of the Phase-1 pile-up subtraction algorithm. Effectively the same algorithm presented in Section 4.2.

$\mathbf{0.4\times0.4}$ jets: inputs were binned in bins that are 0.08×0.08 big in $\eta\times\phi$. Jets were clustered using 5×5 bins resulting in a window size of 0.4×0.4.

As for jets built using PF candidates, the $\eta\times\phi$ space was split in 120×72 bins, each one being 0.083×0.087 big. These jet sizes were investigated:

$\mathbf{0.4\times0.4}$ jets: jet were clustered using 5×5 bins corresponding to a window size of 0.415×0.435.

$\mathbf{0.6\times0.6}$ jets: jet were clustered using 7×7 bins corresponding to a window size of 0.581×0.609.

$\mathbf{0.8\times0.8}$ jets: jet were clustered using 9×9 bins corresponding to a window size of 0.747×0.783.

The performance with PUS was not investigated with PF candidates, since pile-up subtraction is intrinsic in PUPPI.

The same inequality mask as in Fig. 4.1 was scaled down to 5×5 and 7×7 bins, to investigate jets found with these window sizes. The total momentum over the investigated window is assigned as

the preliminary jet p_T , while the seed η and ϕ position are assigned as the jet axis.
Calculation of E_T^{miss} and H_T was implemented and studied using PF candidates as input. The former was computed by first dividing the ϕ space in intervals, computing the total p_T of the inputs in each ϕ range, and finally multiplying the total p_T by the corresponding value of the trigonometric functions sin and cos at the centre of the ϕ interval, in order to emulate a LUT. The quantity H_T was obtained by computing the total p_T of all jets whose $p_T > 30$ GeV.

4.3.1 Jet calibration

Jets were calibrated based on their p_T and position in order to compensate for the dishomogeneous response of the calorimeter which can vary based on the jet energy and its position. Factors were computed using two different samples based on the type of particle flow input. Correction factors for jets built using PF candidates were obtained by matching generator-level jets, i.e. hadron jets reconstructed by running the AK4 algorithm on particles in output from the event generator, to histogrammed jets in a QCD and $t\bar{t}$ Monte Carlo samples at $\langle \text{PU} \rangle \approx 200$. A larger QCD-only sample at $\langle \text{PU} \rangle \approx 200$ was used for the PF clusters. Matching was performed by searching for the closest histogrammed jet to a generator-level one within $\Delta R < 0.5$, with $\Delta R = \sqrt{\Delta\eta^2 + \Delta\phi^2}$. Mismatches were prevented by also requiring a reverse matching, i.e. by verifying that the generator-level jet was the closest jet to the histogrammed one. This matching procedure will be used various times in this thesis to pair various types of objects and will be referred to as cross-matching.
Calibration factors were computed by first obtaining the distribution of the ratio $p_T^{\text{gen}} / p_T^{\text{L1T}}$ between the generator and trigger jet p_T in bins of p_T^{L1T} and η. This distribution was then fit with a Gaussian function to have a better estimate of its centre, which was used as calibration factor. The number of events containing PF candidates available for this study was much smaller than the one containing PF clusters. This caused correction factors for jets produced with PF candidates to have large fluctuations due to insufficient statistics. Correction factors for these jets were adjusted in order to reduce fluctuations. Firstly, factors were fit with the following function:

$$f(p_T^{\text{L1}}) = \begin{cases} a\,(p_T^{\text{L1}})^2 + b\,p_T^{\text{L1}} + c & 30\text{ GeV} < p_T^{\text{L1}} < 80\text{ GeV} \\ d\,p_T^{\text{L1}} + e & 80\text{ GeV} < p_T^{\text{L1}} < 200\text{ GeV} \\ f\,p_T^{\text{L1}} + g & 200\text{ GeV} < p_T^{\text{L1}} < 600\text{ GeV} \end{cases} \tag{4.1}$$

with a, b, c, d, e, f, and g parameters of the fit. New corrections were, then, obtained from the resulting function over the fitted range. Correction factors below 30 GeV were set to $f(p_T^{\text{L1}} = 30\text{ GeV})$.
Figure 4.2 shows as an example the correction factors for Phase-1 jets built with PF clusters in the $1.83 < \eta^{\text{L1T}} < 1.93$ region, and for 7 × 7 jets built using PF candidates. Factors computed for jets built with both input types in the $3 < |\eta^{\text{L1T}}| < 5$ region had large uncertainties, due to limited statistics. The fluctuations were so significant that it was not possible understand the trend of

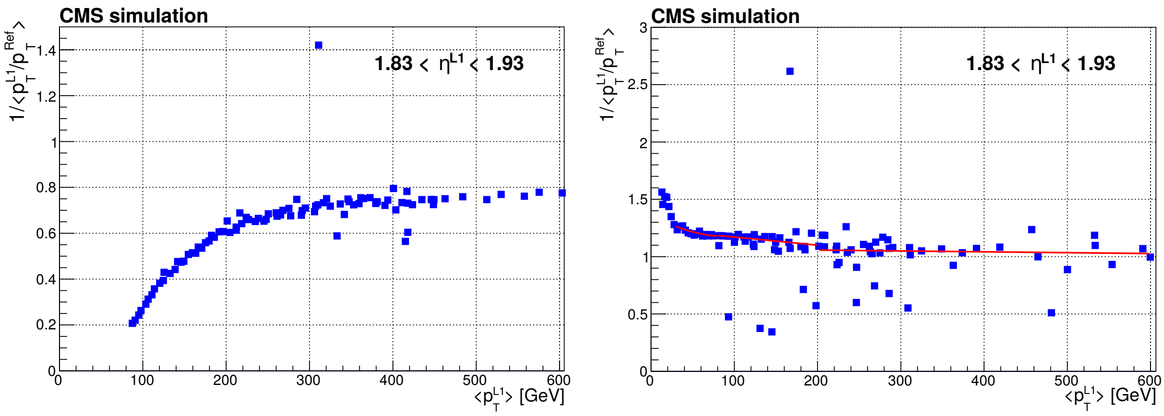

(a) Phase-1 jets with PF clusters

(b) 0.6 × 0.6 jets with PF candidates

Figure 4.2: Calibration factors in the $1.83 < \eta^{\mathrm{L1T}} < 1.93$ region of jets built with PF clusters and PF candidates. The red line in Fig. (b) shows the factors actually used to correct jets computed from PF candidates.

the factors. Therefore, the same technique previously used to mitigate fluctuations could not be performed and the energy of jets in this η range was not corrected.

Calibrations for this η range could be derived by either producing a larger QCD sample, or by studying another physics process. The Higgs boson production via vector boson fusion is a valid alternative, as it features jets in the forward region of the detector.

4.4 Performance of the jet and sum trigger algorithm

The reconstruction performance of the jet trigger will be presented in this section. The performance of jet configurations presented in Section 4.3 was analysed and compared to that of the AK4 algorithm run on the same inputs, which represents the ideal reconstruction performance. Jets identified with the AK4 algorithm will be referred to with the **AK4 jets** label. Jet energy correction factors were computed for AK4 jets with both particle flow input types in the same way as the others. Factors for AK4 jets obtained from PF candidates were adjusted using data interpolation as well.

Jets with PF clusters and candidates were studied on the same QCD and $\mathrm{t\bar{t}}$ sample their calibrations were calculated from. Generator-level jets were cross-matched with jets obtained from the histogrammed and AK4 algorithm. The resulting jet pairs were processed to compute the reconstruction performance of the trigger.

An important quantity that will be used in this section is the trigger response:

$$\text{Response} = \frac{p_{\mathrm{T}}^{\mathrm{L1T}} - p_{\mathrm{T}}^{\mathrm{gen}}}{p_{\mathrm{T}}^{\mathrm{gen}}} \tag{4.2}$$

where $p_{\mathrm{T}}^{\mathrm{L1T}}$ is the momentum of the jet found using the trigger inputs, and $p_{\mathrm{T}}^{\mathrm{gen}}$ is the momentum of the generator-level jet matched to it.
Finally, the detector was split in four regions, identified based on the subdetectors involved in the particle flow reconstruction:

Barrel: $|\eta| < 1.5$, which is the region covered by the barrel hadron and electromagnetic calorimeter

Endcap with tracker: $1.5 < |\eta| < 2.5$, which is the region covered by the tracker and the HGCAL

Endcap without tracker: $2.5 < |\eta| < 3$, which is the region only covered by the HGCAL

Forward: $3 < |\eta| < 5$, which is the region only covered by the HF detector; jets in this region are not energy-corrected

The performance of the various jet configurations was analysed in these four regions to understand the impact that each subdetector has on the algorithm performance. Since PF candidates are built with the same trigger primitives as PF clusters in the $|\eta| > 2.5$ region and provide the best input quality available, jets obtained from PF clusters were not studied in this area.

4.4.1 Jet energy corrections

Correction factors in three η regions for jets built with PF clusters and PF candidates are respectively shown in Figs. 4.3 and 4.4.
All jet configurations with PF clusters, including AK4, tend to overestimate the momentum of jets, as the correction factors are less than 1. This can be attributed to the pile-up contribution, as factors get closer to one when a smaller jet window or a pile-up subtraction algorithm is used. The correction factors of the 0.4×0.4 and Phase-1 with PUS jet types also appear to depend less on the jet momentum, as they are constant over a wide range of p_{T} .
Factors are greater than 1 for all jet configurations with PF candidates, showing that the jet energy is underestimated. This indicates that the pile-up subtraction algorithm, PUPPI, is successfully subtracting pile-up energy and is partially removing energy from the primary vertex in doing so.

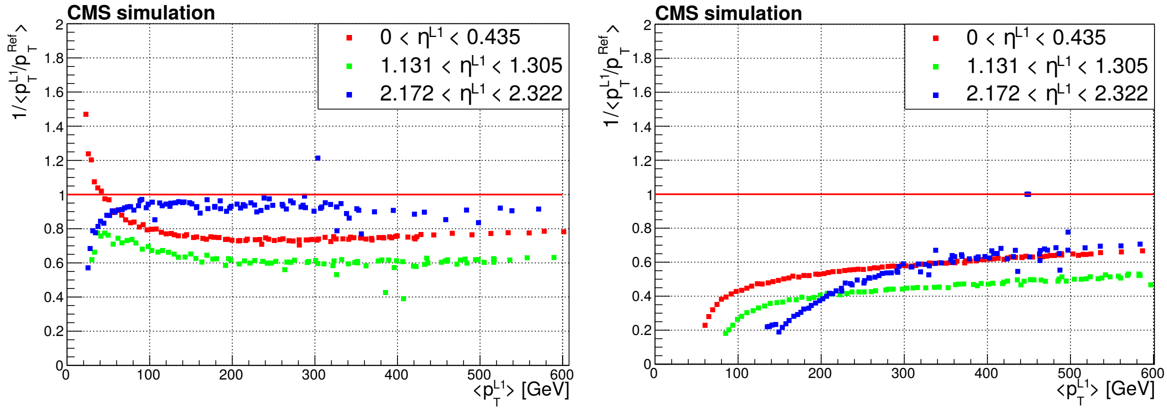

(a) 0.4 × 0.4 jets

(b) Phase-1 jets

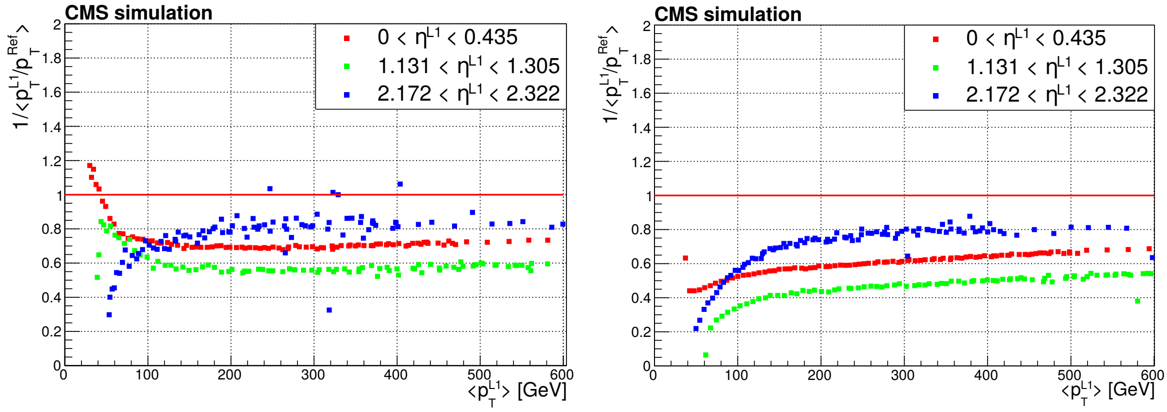

(c) Phase-1 with pile-up subtraction jets

(d) AK4 jets

Figure 4.3: Jet energy correction factors for jets obtained using the histogrammed algorithm on PF clusters with the three different jet configurations and with the AK4 algorithm.

4.4.2 Jet area study

The performance of the histogrammed jet configurations under study was compared to AK4 jets by looking at each η region separately to find the optimal algorithm tune. Figures 4.5(a) and 4.5(b) display the response of jets computed from PF clusters: the Phase-1 and 0.4 × 0.4 jet configurations provide similar performance to AK4 in the barrel and endcap, respectively. The results in the endcap region are in agreement with what shown in the HGCAL Technical Design Report [72], where it is shown that the anti-k_T algorithm with $R = 0.2$ performs better than AK4, as smaller jet sizes appear to be more resilient to pile-up in this area. The same seems to not apply to the barrel, where a larger jet performs better.

Using PUS appears suboptimal in all regions. Not using any pile-up subtraction algorithm and letting the correction factors correct for pile-up energy is a possible solution at HL-LHC, where luminosity levelling will keep the instantaneous luminosity and pile-up conditions roughly constant throughout a fill. Moreover, the pile-up energy density is expected to be uniform over

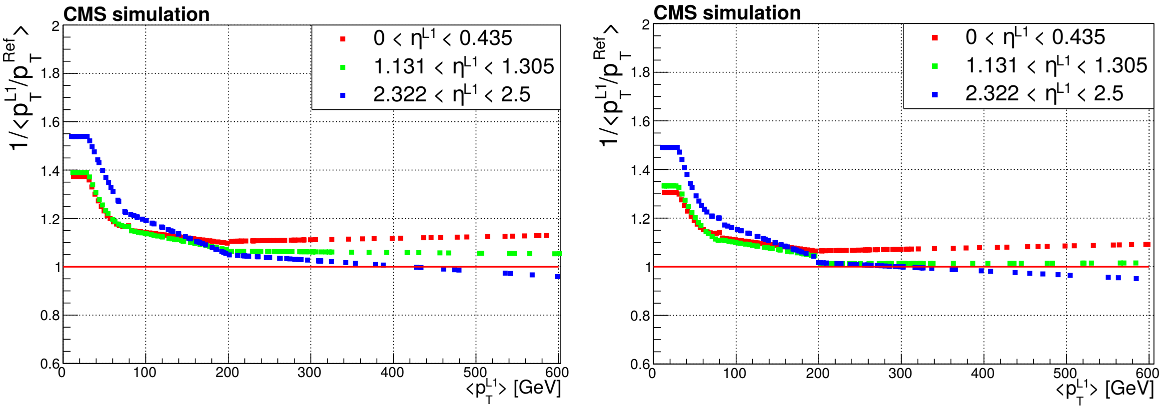

(a) 0.4 × 0.4 jets

(b) 0.6 × 0.6 jets

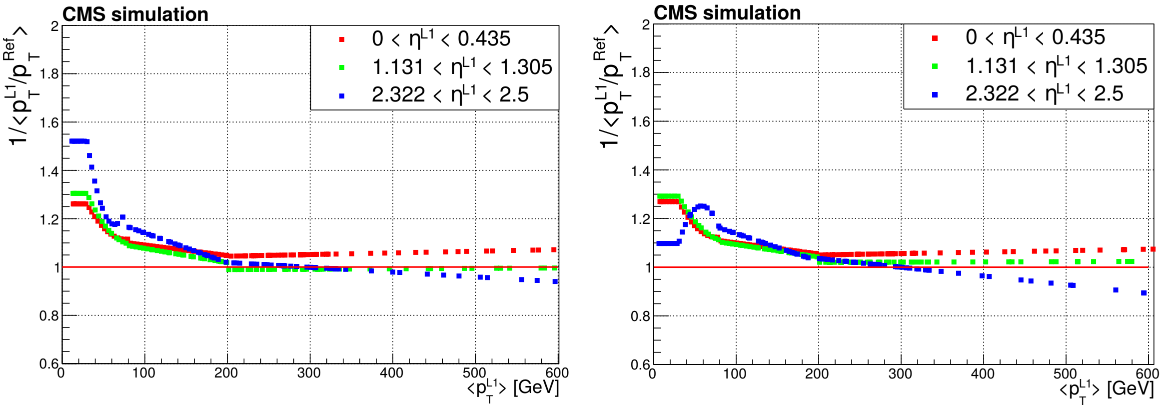

(c) 0.8 × 0.8 jets

(d) AK4 jets

Figure 4.4: Jet energy correction factors for jets obtained using the histogrammed algorithm on PF candidates with the three different jet sizes and with the AK4 algorithm.

the detector space due to the high pile-up level, removing the need for a local measurement. However, handling pile-up with this method might become more technically difficult to achieve in fills without luminosity levelling, as multiple sets of jet energy corrections that depend on the luminosity level would have to be dynamically deployed. In this situation, using an algorithm with pile-up subtraction might be advisable.

The 0.8 × 0.8 jet configuration have very similar performance to AK4 with PF candidates as input, according to Figs. 4.5(c)–4.5(f). Performance worsens with smaller windows: jets obtained with a 0.6 × 0.6 window size have slightly worse response; clustering using a 0.4 × 0.4 window tends to significantly underestimate p_T , showing that an important fraction of jet energy is not included any longer. This behaviour differs from jets computed with PF clusters and seems to indicate that there is no benefit in using smaller jet sizes to reduce pile-up contribution in the endcap, possibly because PUPPI is able to successfully remove most of it.

The 0.4 × 0.4 jet configuration was selected for further studies for jets built with PF clusters, due to its much improved performance in the endcap. As for the jets built with PF candidates,

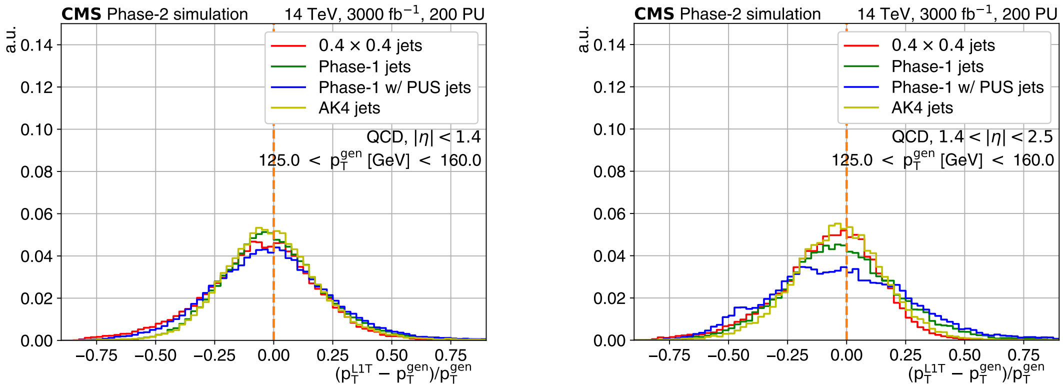

(a) PF clusters, barrel

(b) PF clusters, endcap with tracker

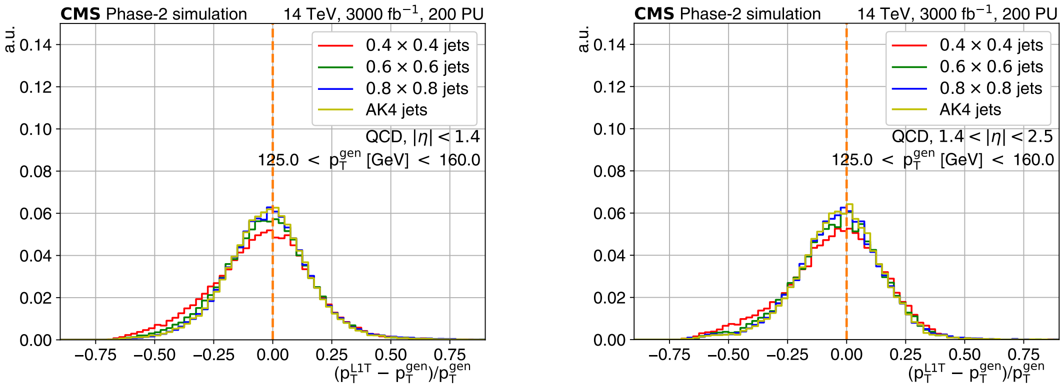

(c) PF candidates, barrel

(d) PF candidates, endcap with tracker

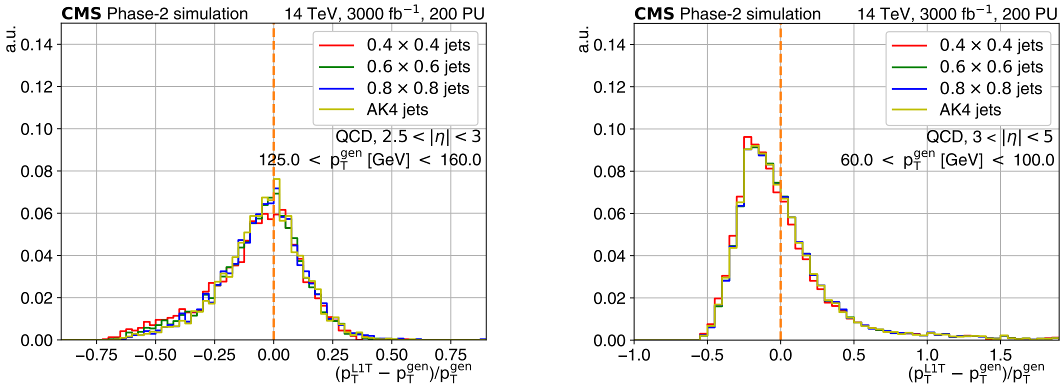

(e) PF candidates, endcap without tracker

(f) PF candidates, forward

Figure 4.5: Comparison of the response of the jet trigger configurations under study and AK4 algorithm on PF clusters and candidates split in detector regions. Jets in the forward region are not energy-corrected. Distributions are normalised to unit area.

using a 0.8 × 0.8 window seems the best choice, however it will be shown in Chapter 5 that implementing a clustering window of that size is harder than 0.6 × 0.6, which was implemented and demonstrated in firmware instead. For these reasons, the performance of both 0.6 × 0.6 and 0.8 × 0.8 jets was studied in more detail.

All selected algorithms have similar response to AK4, showing that the p_{T} resolution of the inputs is the limiting factor in defining the response and, consequently, finding an alternative algorithm able to provide much better response is unlikely.

4.4.3 Performance of the histogrammed jet algorithm

Figure 4.6 shows the response of the 0.4 × 0.4 jet configuration on PF clusters, and 0.6 × 0.6 and 0.8 × 0.8 jet configurations on PF candidates as a function of $p_{\mathrm{T}}^{\mathrm{gen}}$ and η.

The response curve displayed in Fig. 4.6(a) is asymmetric with a longer tail towards the positive side for low-p_{T} jets and towards the negative side for jets with $p_{\mathrm{T}} > 100$ GeV. The plot demonstrates that jets below 100 GeV still receive a significant contribution from pile-up, which becomes negligible above that energy. In general, the response improves as the p_{T} of the jet increases. Figure 4.6(b) more clearly shows that the 0.4 × 0.4 jet configuration has better performance in the endcap, as previously discussed.

The response of the 0.6 × 0.6 and 0.8 × 0.8 jet configurations, respectively presented in Figs.4.6(c) and 4.6(e), is almost identical. The response distributions appear much more symmetrical compared to jets built with PF clusters, although a slightly longer tail towards the negative side can be observed, especially in the 0.6 × 0.6 jet configuration. This is compatible with what previously suggested by the calibration factors in Section 4.4.1: PUPPI is removing a fraction of energy from primary vertex, causing the jet energy to be underestimated. This feature is more pronounced in 0.6 × 0.6 jets as the smaller window misses more energy from the hard interaction. Figs.4.6(d) and 4.6(f) show that the response does not significantly vary over the detector, maintaining the same response even in the region not covered by the tracking system, where the PUPPI is less effective. This suggests that using the same pile-up subtraction techniques employed in the $|\eta| > 2.5$ region on the PF clusters in the $|\eta| < 2.5$ area of the detector might further improve the performance of the jet finder. The differences that were observed between the Phase-1 and 0.4 × 0.4 configuration could potentially be reduced by using these techniques.

Jets built from PF candidates should to have better spatial resolution than the ones built from PF clusters, thanks to the additional track information. However, only a small improvement was actually observed. Comparing Fig. 4.7(b) with Figs. 4.9(a), and Fig. 4.7(d) with Fig. 4.9(c) shows that the AK4 algorithm has better η resolution, especially when PF candidates are used as input. The same can be observed in the ϕ resolution by comparing Fig. 4.8(b) with Figs. 4.9(b) and 4.8(d) with Fig. 4.9(d). This demonstrates that the algorithm choice is limiting the η and ϕ resolution of the trigger. Therefore, it might be possible to improve the spatial resolution of the trigger by using a different algorithm. For instance, computing the jet position as the average of the position

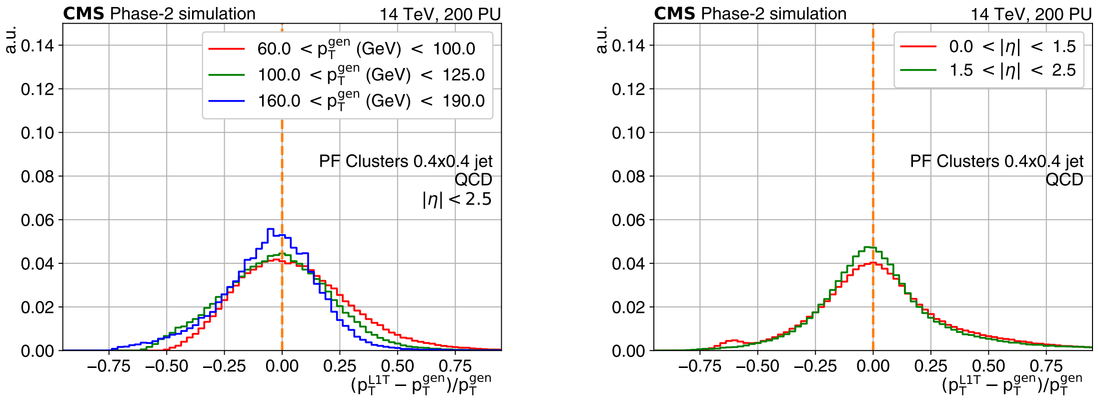

(a) PF clusters, 0.4 × 0.4 jets

(b) PF clusters, 0.4 × 0.4 jets

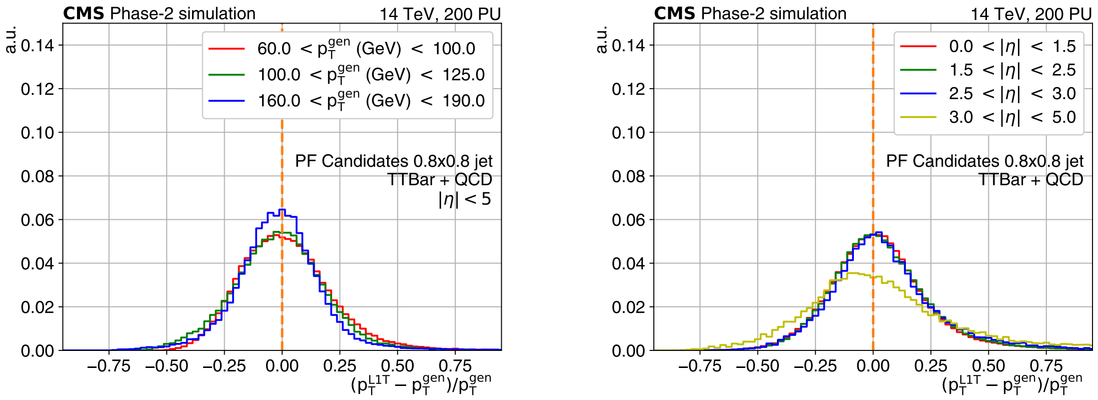

(c) PF candidates, 0.8 × 0.8 jets

(d) PF candidates, 0.8 × 0.8 jets

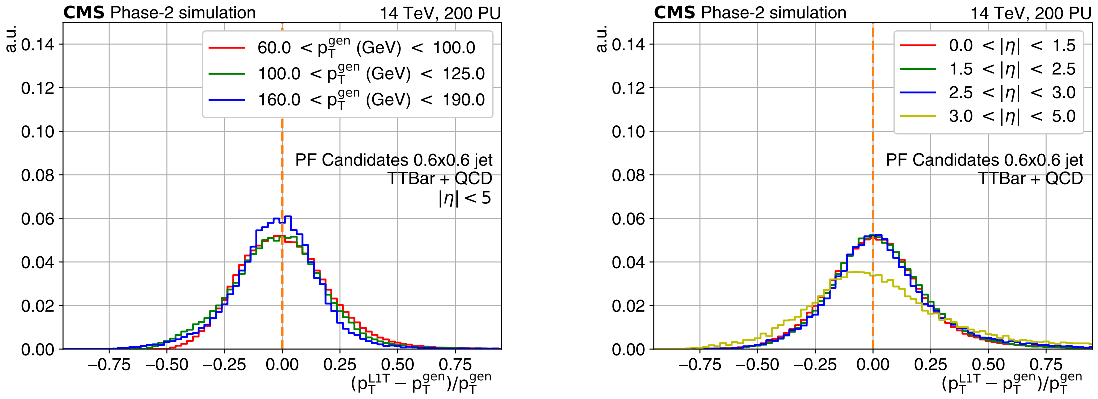

(e) PF candidates, 0.6 × 0.6 jets

(f) PF candidates, 0.6 × 0.6 jets

Figure 4.6: Left: Response of the 0.4 × 0.4 jet configuration on PF clusters, and the 0.6 × 0.6 and 0.8 × 0.8 jet trigger configurations on PF candidates in three different p_T^{gen} bins. Right: Response of the same configurations on the left averaged over detector regions. The feature on the left tail of Fig. (b) is caused by a miscalculated correction factor. Jets in the $|\eta| > 5$ region are not energy-corrected. Distributions are normalised to unit area.

of the histogram bins within the clustering window weighted by their momentum might return better results.

An offset in the η position of the jets was found in forward calorimeters, i.e. the $3 < |\eta| < 5$ region of the detector, which is shown in yellow and purple in Fig. 4.7(d). This issue does not appear to be caused by bug in the jet finder, but rather by an offset in the particle flow inputs, as Fig. 4.9(c) indicates that AK4 jets are also affected by the same problem. The source of the problem was found to be in a mismatch in the physical and logical segmentation of the HF detector which caused an offset in the position assignment of the energy deposits and, consequently, in the reconstructed location of the jets. The offset could be removed during jet finding by either subtracting the center of the η resolution curves to inputs in the corresponding η range or to jets found using those inputs. This operation is expected to be very simple to perform on FPGA as well. However, subtracting the offset during input generation in the first layer of the correlator trigger is a more appropriate solution, as this would address the problem for every algorithm that receives particle flow inputs. In case this last solution appears to not be feasible, then a patch could be applied in the jet finder.

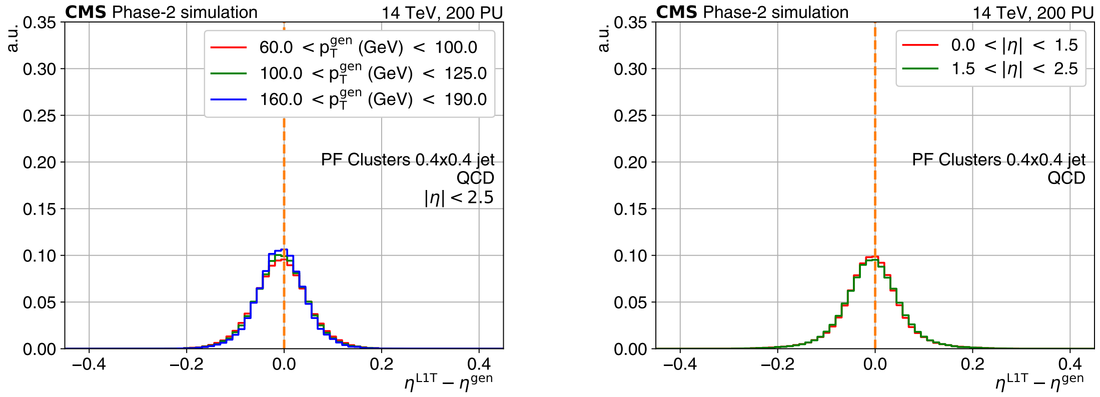

(a) PF clusters, 0.4 × 0.4 jets (b) PF clusters, 0.4 × 0.4 jets

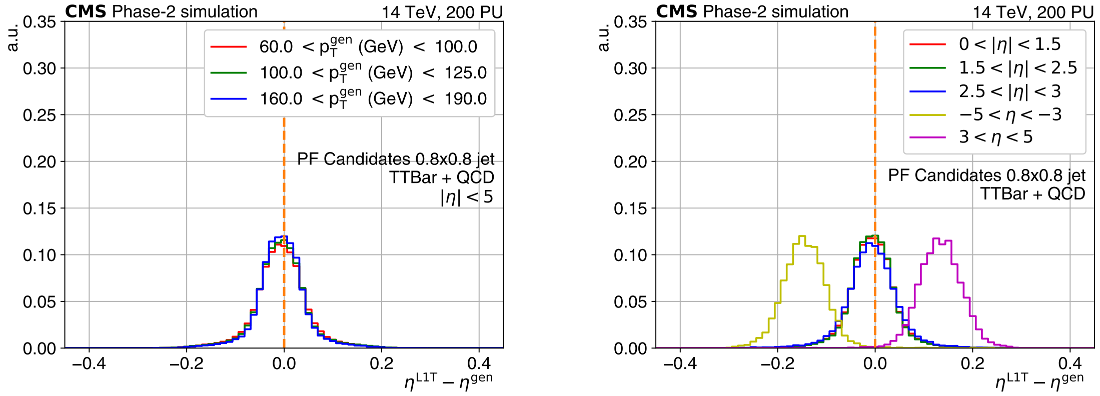

(c) PF candidates, 0.8 × 0.8 jets (d) PF candidates, 0.8 × 0.8 jets

Figure 4.7: Left: η resolution of the 0.4×0.4 jet trigger configuration on PF clusters and 0.8×0.8 jet trigger configuration on PF candidates in three different p_T^{gen} bins. Right: η resolution of the same jet configurations averaged over detector regions. Offsets in the η position of the inputs were observed in the forward calorimeters. Distributions are normalised to unit area. The η resolution of the 0.6×0.6 jet finder on PF candidates was found to be identical to the one of the 0.8×0.8 configuration and is not shown.

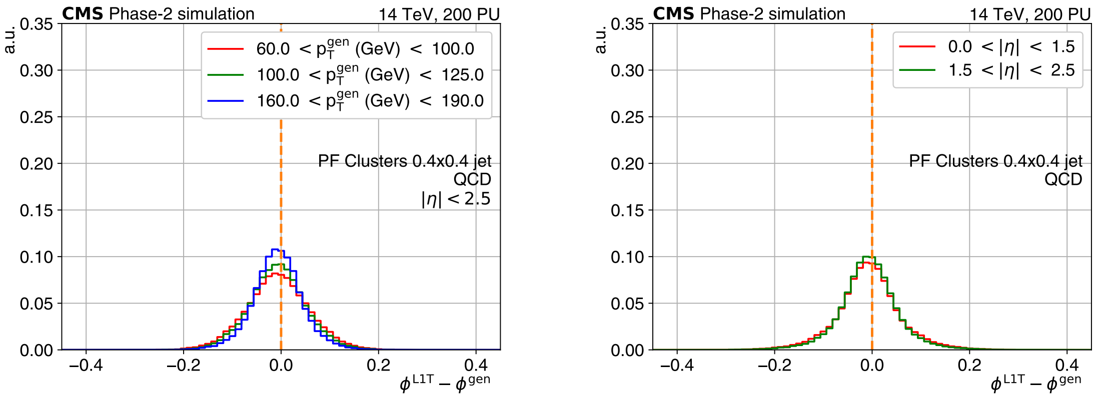

(a) PF clusters, 0.4 × 0.4 jets

(b) PF clusters, 0.4 × 0.4 jets

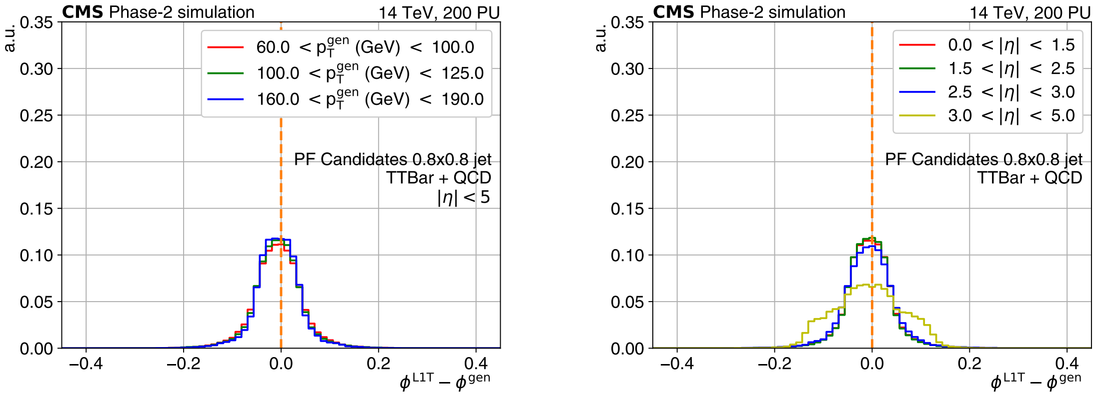

(c) PF candidates, 0.8 × 0.8 jets

(d) PF candidates, 0.8 × 0.8 jets

Figure 4.8: Left: ϕ resolution of the 0.4 × 0.4 jet trigger configuration on PF clusters and 0.8 × 0.8 jet trigger configuration on PF candidates in three different p_T^{gen} bins. Right: ϕ resolution of the same jet configurations averaged over detector regions. Distributions are normalised to unit area. The ϕ resolution of the 0.6 × 0.6 jet finder on PF candidates was found to be identical to the one of the 0.8 × 0.8 configuration and is not shown.

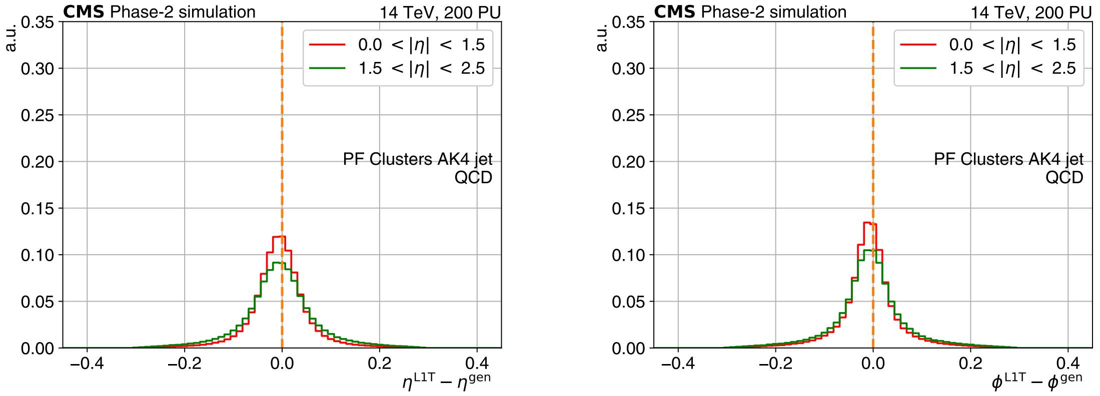

(a) η resolution, PF clusters

(b) ϕ resolution, PF clusters

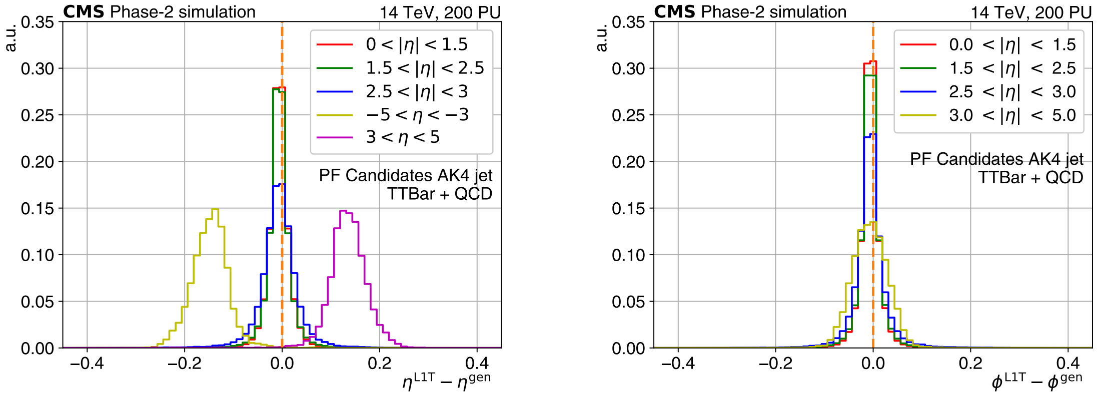

(c) η resolution, PF candidates

(d) ϕ resolution, PF candidates

Figure 4.9: Left: η resolution of the AK4 jet algorithm on PF clusters and candidates split in η bins. Offsets in the η position of the inputs were observed in the forward calorimeters. Right: ϕ resolution of the same jet configurations average over detector regions. Distributions are normalised to unit area.

4.4.4 Performance of the energy sum algorithms

The performance of the energy sum algorithms was studied using PF candidates and 0.6 × 0.6 jet inputs. The response of the algorithm was computed in an analogous fashion to Eq. 4.2 by comparing sums computed by the trigger with the equivalent obtained from the event generator. Figure 4.10 shows the responses of the $p_{\mathrm{T}}^{\mathrm{miss}}$ and H_{T} algorithms as a function of the respective value in the event generator. The H_{T} response is centred on 0, while the $p_{\mathrm{T}}^{\mathrm{miss}}$ response has a negative offset. Two possible reasons were investigated to understand the source of the offset. First, it was checked whether discretising the sine and cosine functions had severely degraded the $p_{\mathrm{T}}^{\mathrm{miss}}$ performance, causing the offset. $p_{\mathrm{T}}^{\mathrm{miss}}$ was computed in the same events using the actual values of the functions, instead of the discretised ones. Figure 4.11 presents a comparison of the response of the trigger algorithm in the two scenarios. No difference was observed, thus excluding discretisation as a cause.

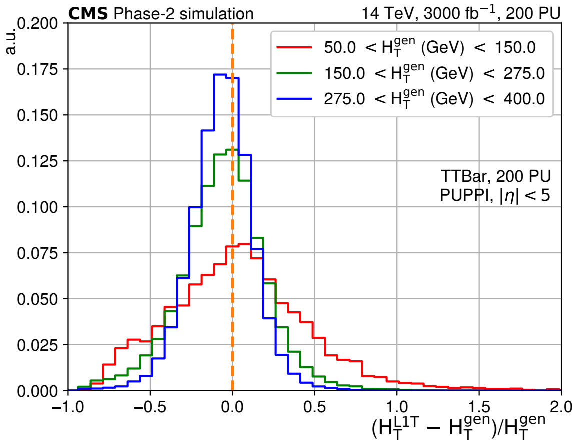

(a) H_{T} response

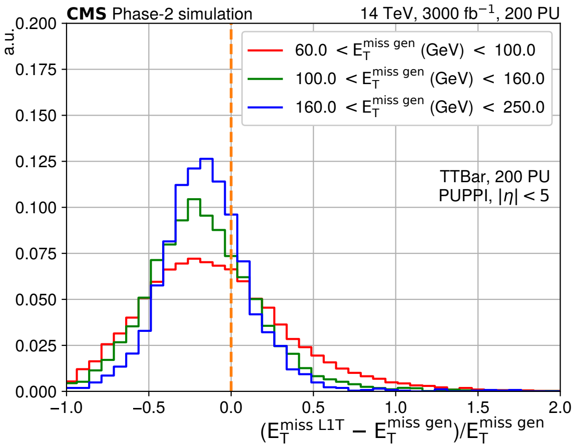

(b) $p_{\mathrm{T}}^{\mathrm{miss}}$ response

Figure 4.10: Response of the H_{T} and $p_{\mathrm{T}}^{\mathrm{miss}}$ algorithm to $\mathrm{t\bar{t}}$ events as a function of the respective value in the event generator. The H_{T} response appears to be centred on 0, while the $p_{\mathrm{T}}^{\mathrm{miss}}$ one does not.

Second, it was verified whether it was an issue with the $\mathrm{t\bar{t}}$ event topology. Four other event types were analysed to confirm :

- Higgs boson produced via vector-boson-fusion decaying invisibly
- Z boson decaying invisibly
- Z boson decaying invisibly produced in association with a photon
- Z boson decaying into a b-quark pair produced in association with an Higgs boson decaying invisibly

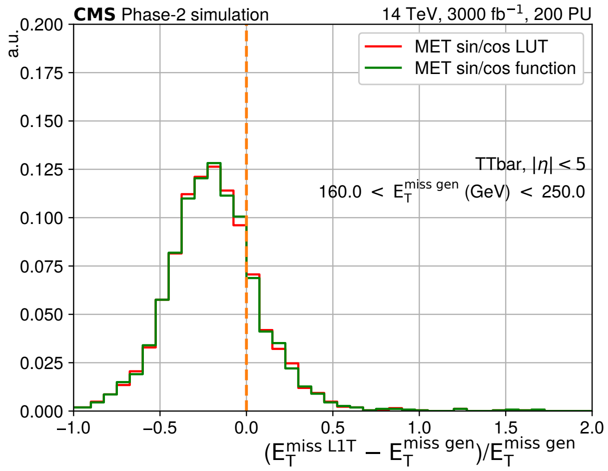

Figure 4.11: Comparison between the p_T^{miss} response of the trigger when the trigonometric functions are stored in a LUT and when they are actually evaluated in events with p_T^{miss} between 160 and 250 GeV. No substantial difference between the two distributions was observed.

In all samples, except the first, the invisible particle had $p_T > 120$ GeV to produce measurable p_T^{miss} . Figure 4.12 shows that the offset is present in most of samples, although its position mildly depends on the event topology. This excludes the event topology as a cause.

In conclusion, the offset appears to be an issue with the PF candidate calibration. This is supported by Fig. 4.4, which shows that the p_T of jets obtained from PF candidates is underestimated, indicating that the response of the particle flow reconstruction needs further corrections, at least when in an hadron jet. The response of the H_T^{miss} trigger also suggests that calibrating the PF candidates may solve the issue. H_T^{miss} is defined as the transverse component of the vector:

$$\vec{H} = \sum_{\text{jets}} \vec{p}_{\text{jet}} \text{ if } p_T > 30 \text{ GeV}$$

This quantity is typically used in analysis where the missing energy mostly has an hadronic signature, as in searches for SUSY particles. Figure 4.13 shows that the response of the H_T^{miss} trigger is centred on zero, as jets are calibrated.

Further work should investigate and address the issue. The following method, which is already applied in offline analyses by the CMS experiment, could be performed to compute a corrected p_T^{miss} response:

1. Jets are found with the clustering procedure and their energy corrected.
2. Particles that are included in any of the reconstructed jets are removed from the list of particles in the event.
3. p_T^{miss} is computed using the remaining particles and the corrected jets.

Maintaining the offset in the p_T^{miss} trigger and not applying any corrections means that a scaling between the measured p_T^{miss} and the actual p_T^{miss} must be introduced. However, Fig. 4.12 shows

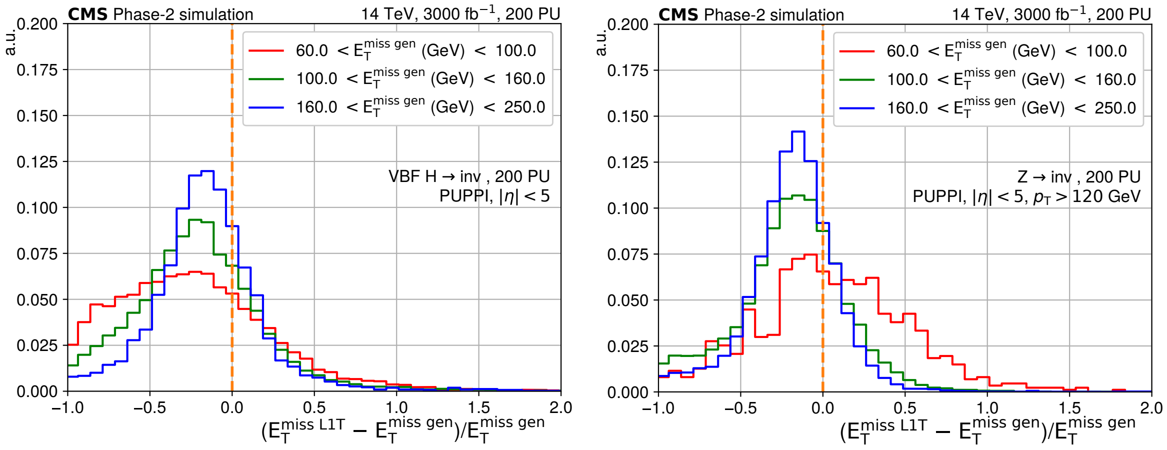

(a) Invisible Higgs boson (b) Invisible Z boson

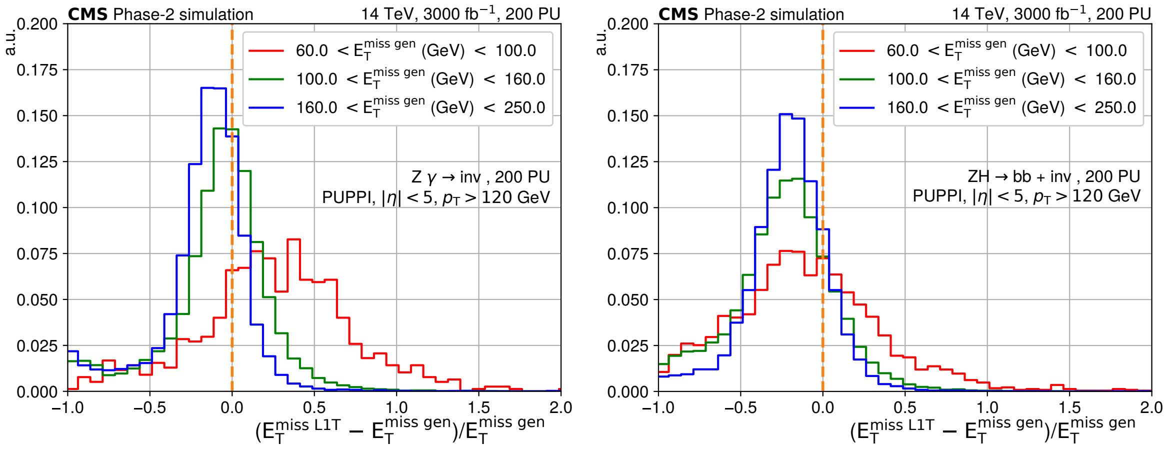

(c) Invisible Z boson + photon (d) Z boson + invisible Higgs boson

Figure 4.12: Response of the p_T^{miss} trigger to four different event types. An offset in the measurement was observed in most of them.

that the p_T^{miss} response slightly differs based on the signal under consideration and the efficiency turn-on depends on the event topology. Because of this, a signal-independent set of scaling factors can not be used. This is known in CMS analysis, which usually take account for the specific efficiency turn-on of the signal under study.

4.4.5 Trigger efficiency and rates

A turn-on describes the efficiency of a trigger as a function of the momentum of an object. Turn-on curves were computed for the 0.6 × 0.6 and 0.8 × 0.8 jet trigger configurations on PF candidates for a variety of p_T thresholds as a function of the p_T^{gen} of the jet. The jet trigger efficiency was computed by first cross-matching the leading p_T jet in the event generator to a histogrammed jet. Pairs of generator and histogrammed jets were then split into p_T^{gen} bins and in each bin the

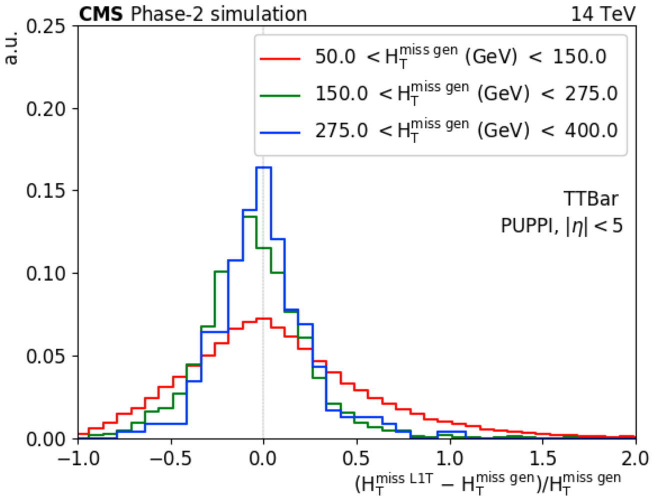

Figure 4.13: Response of the H_T^{miss} trigger. Taken from [94]. Results produced by Katie Walkingshaw-Pass in collaboration with the author.

efficiency for a specific threshold T was computed:

$$\varepsilon(p_T^{\text{gen}}) = \frac{n_{\text{pass}}(p_T^{\text{gen}})}{n_{\text{tot}}(p_T^{\text{gen}})} \tag{4.3}$$

where n_{pass} is the number of events whose $p_T^{\text{L1T}} > T$ and n_{tot} is the total number of events with p_T^{gen} in that bin. Turn-on curves of the H_T and p_T^{miss} triggers were also obtained with an analogous method from pairs of sums computed by the trigger and from equivalent inputs in the event generator.

Fig. 4.14 shows the efficiency of single-jet trigger using 0.6 × 0.6, 0.8 × 0.8 and AK4 jet configurations with PF candidates as input in QCD and $t\bar{t}$ events. Jets in the forward region of the detector were excluded, as they are not calibrated. Both configurations have very similar efficiency to AK4, with 0.8 × 0.8 being slightly sharper, and plateau at 100%, which is of fundamental importance as high-momentum jets should always be detected.

Figure 4.15 displays the efficiency of the H_T and p_T^{miss} triggers presented in Section 4.4.4. The turn-on of the H_T trigger was computed from jets in the $|\eta| < 2.4$ range as this trigger is typically used to collect events containing hadronic decays of high-mass objects, which usually produce jets in the central region of the detector. The efficiency of the H_T trigger was obtained in QCD and $t\bar{t}$ events. Only $t\bar{t}$ events were considered in obtaining the turn-on of the p_T^{miss} trigger in order to have genuine p_T^{miss} . For comparison, Figure 4.15 also shows the efficiency turn-ons of the H_T trigger using AK4 jets as input and of the p_T^{miss} trigger when the actual sin(ϕ) and cos(ϕ) of each input is evaluated in the sum calculation. The H_T trigger has similar efficiency to the same algorithm run on AK4 jets and plateaus at 100%. As previously suggested by Fig. 4.11, Figure 4.15(b) shows that discretising the sin and cos function does not cause any significant

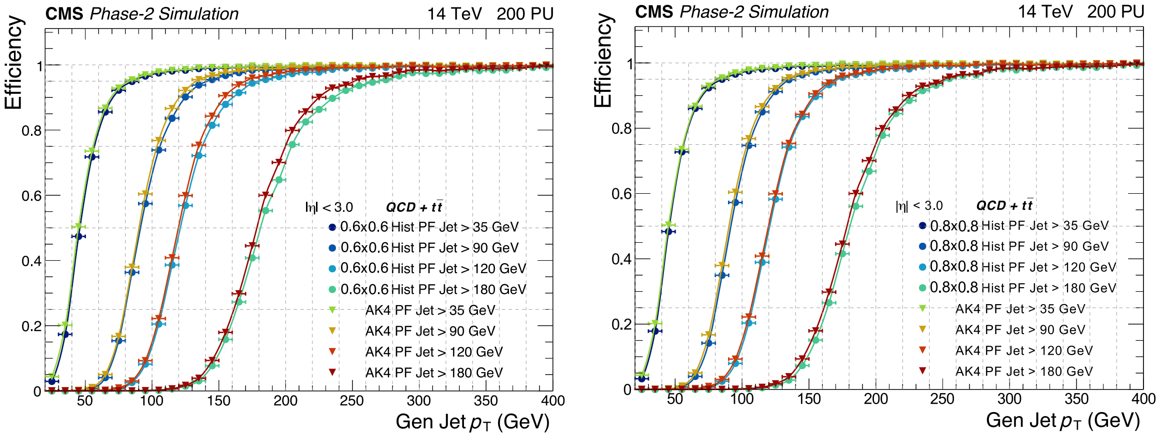

(a) 0.6 × 0.6 jets

(b) 0.8 × 0.8 jets

Figure 4.14: Efficiency turn-on curves of single-jet triggers using 0.6 × 0.6, 0.8 × 0.8, and AK4 jets in QCD and $t\bar{t}$ events using PF candidates as input. The $|\eta| > 3$ range was excluded as jets in this area do not have energy corrections applied. Taken from Ref. [31]. Results produced by Aaron Bundock in collaboration with the author.

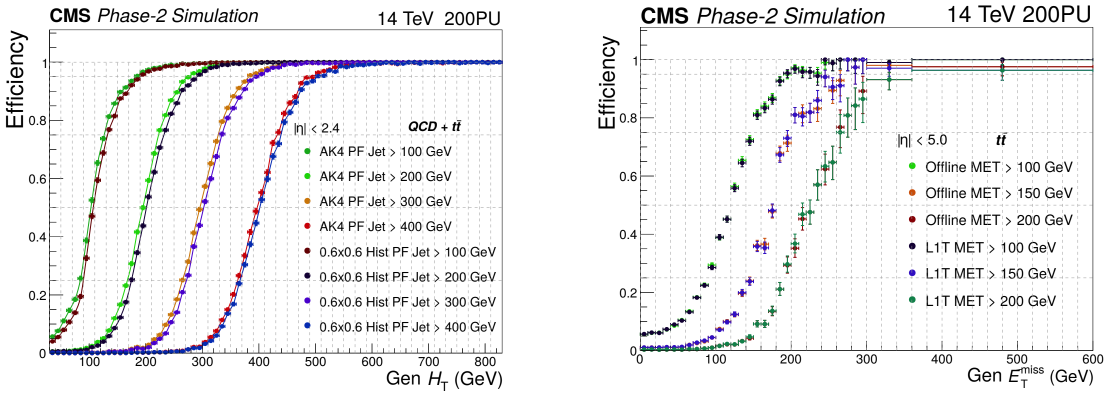

(a) H_T

(b) p_T^{miss}

Figure 4.15: Efficiency turn-on curves of H_T and p_T^{miss} triggers. The efficiency of the H_T trigger is compared with the same H_T algorithm run on AK4 jets. The efficiency of the p_T^{miss} trigger is compared with the "'offline"' algorithm that computes p_T^{miss} by evaluating the value of sin(ϕ) and cos(ϕ) of each input. Results produced by the author in collaboration with Emyr Clement and Katie Walkingshaw-Pass.

degradation of the $p_{\mathrm{T}}^{\mathrm{miss}}$ trigger efficiency. The $p_{\mathrm{T}}^{\mathrm{miss}}$ turn-on appears to be less steep than the other triggers, which is expected, and plateaus at 100%.

Background rates from events at $\langle \mathrm{PU} \rangle = 200$ were computed for the single-jet, $p_{\mathrm{T}}^{\mathrm{miss}}$, and H_{T} triggers and are shown in Fig. 4.16. A potential trigger menu targeting $\mathscr{L}_{\mathrm{inst}} = 7 \times 10^{34}\ \mathrm{cm}^{-2}\ \mathrm{s}^{-1}$ is presented in the technical design report of the Phase-2 upgrade of the L1T [31]. The 0.6×0.6 jet configuration was chosen as the flagship algorithm for jet reconstruction using particle flow inputs in the menu studies. The analysis of H_{T} and $p_{\mathrm{T}}^{\mathrm{miss}}$ triggers in the menu was performed using the offline reconstruction algorithms on PF candidates as a proxy for the L1T algorithms, as the energy sum algorithms presented in this thesis were developed after the document was finalised. The offline algorithms have similar performance to the ones implemented in the trigger, however. Thresholds in the menu are reported in terms of a so-called "offline" threshold, i.e. the $p_{\mathrm{T}}^{\mathrm{gen}}$ value corresponding to 95% efficiency in the turn-on curve of the chosen trigger. For H_{T} and $p_{\mathrm{T}}^{\mathrm{miss}}$ triggers, the 90% working point is reported. A bandwidth of 70 kHz is allocated in the menu for the single-jet trigger, corresponding to an offline threshold of 180 GeV. An additional 70 kHz is reserved for a double jet trigger with a offline p_{T} threshold for each object of 70 GeV. The H_{T} and $p_{\mathrm{T}}^{\mathrm{miss}}$ have an allocated bandwidth of 11 and 18 kHz, which corresponds to an offline threshold of 450 and 200 GeV, respectively. This is consistent with the efficiency and rates of the energy sum triggers shown in Figs. 4.15 and 4.16. A quadruple jet trigger with p_{T} thresholds of 70, 55, 40, and 40 GeV and a H_{T} threshold of 400 GeV is also presented, with a rate of 9 kHz.

The jet and sum trigger algorithms are fully integrated in the CMS trigger menu and are fundamental to collect interesting signals. The presented thresholds are similar to the ones currently used in the Phase-1 L1T [93], even through the Phase-2 luminosity is three to four times larger than the Phase-1. Therefore, the algorithms meet the goals of the Phase-2 upgrade of the L1T.

4.5 Conclusions

The design of a generic algorithm able to reconstruct hadron jets and compute the $p_{\mathrm{T}}^{\mathrm{miss}}$ and H_{T} energy sums was presented in this chapter. Its design was optimised in CMS simulations to return the best response with particle flow candidates. Jet reconstruction performance using particle flow clusters was also studied, to investigate its capabilities when information from only the calorimeters is used.

The 0.6×0.6 and 0.8×0.8 jet configurations were found able to return similar jet response to AK4 when run on PF candidates. Its η and ϕ resolution are not as good as the AK4 algorithm, however possible improvements were identified. As for the algorithm performance with PF cluster, the Phase-1 and 0.4×0.4 jet configurations were found to be optimal, depending on the detector region. Results from PF candidates suggest that better response could be obtained by applying pile-up suppression techniques to PF clusters, before attempting clustering. This could help, potentially, in attenuating differences in response between the two tunes.

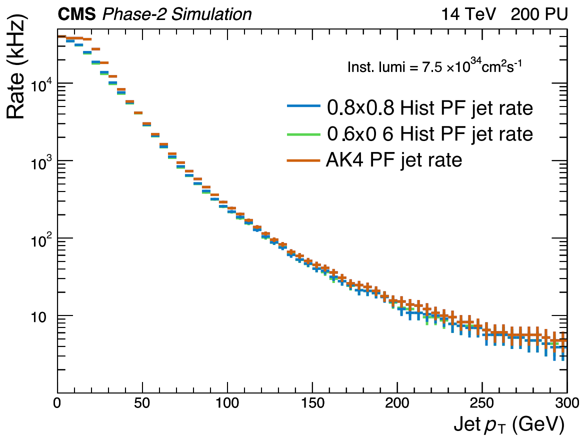

(a) Single-jet

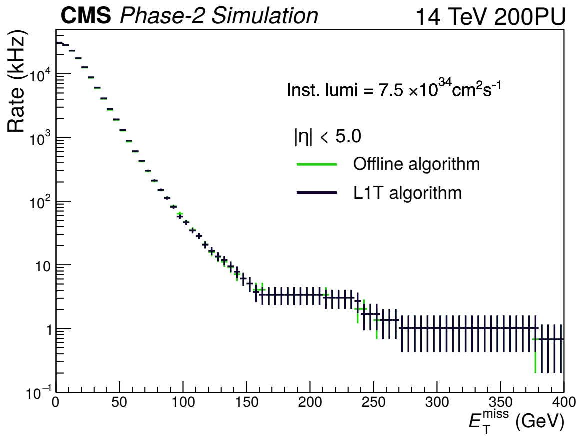

(b) p_T^{miss}

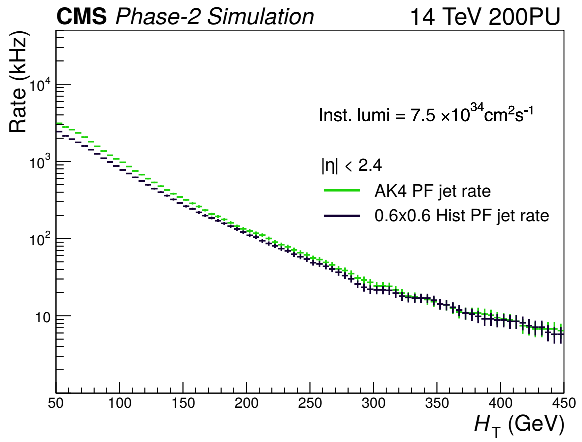

(c) H_T

Figure 4.16: Background rate as a function of the p_T threshold of single-jet, p_T^{miss} , and H_T triggers. Taken from Ref. [31]. Single-jet trigger rates were computed by Aaron Bundock in collaboration with the author. p_T^{miss} and H_T trigger rates were obtained by the author in collaboration with Emyr Clement and Katie Walkingshaw-Pass.

The $p_{\mathrm{T}}^{\mathrm{miss}}$ and H_{T} response was investigated using PF candidates as input. The algorithm tends to underestimate $p_{\mathrm{T}}^{\mathrm{miss}}$. The cause was found to be in the pile up subtraction algorithm, PUPPI, which removes energy from the primary vertex. Implications of the issue and possible solutions were investigated and discussed.

In the next chapter, the implementation of the 0.6×0.6 jet clustering algorithm and the H_{T} and $p_{\mathrm{T}}^{\mathrm{miss}}$ calculation on a FPGA board will be presented together with a proof-of-concept demonstrator running on actual hardware.

CHAPTER

5

IMPLEMENTATION OF THE PHASE-2 JET AND SUM TRIGGER ALGORITHM

The design and the reconstruction performance of an algorithm able to find jets and compute H_T and $p_\mathrm{T}^\mathrm{miss}$ was introduced in Chapter 4. In this chapter the development of the same algorithm on FPGA will be presented. The goal of this work is to understand the feasibility of implementing the algorithm in firmware, discovering the impact of the algorithm on the trigger hardware, and presenting a proof-of-concept demonstrator on an actual trigger board. The tool that will be used to develop the algorithm, Vivado High-Level Synthesis, will be introduced in Section 5.1, together with definitions of important metrics used in FPGA firmware design. Inputs to the algorithm, and its design and implementation on an FPGA will be presented in Section 5.2 and 5.3, respectively. The proof-of-concept demonstrator will be described in Section 5.4 together with its testing and validation against the CMS simulation. Resource usage estimates of the final version of the algorithm, and possible optimisations and improvements will be discussed in Section 5.5.

5.1 High-Level Synthesis workflow

Vivado High-Level Synthesis (HLS) [95] enables users to produce FPGA firmware starting from code written in C, C++, and SystemC programming languages. HLS is an important change in paradigm in FPGA development. FPGA firmware is typically programmed in an hardware description language (HDL) such as Verilog or VHDL. HDL languages are description languages and are different from imperative programming languages such as C++. Code in HDL represents an actual circuit, while code written in an imperative programming language is a set of instructions that are executed by a CPU from top to bottom. HDL languages are widely considered to be difficult to learn, master and understand. Code in high-level programming languages is generally much easier to write and maintain. HLS provides tools to bridge the gap between the two platforms, ultimately simplifying FPGA firmware development. A significant fraction of the firmware of the Phase-2 upgrade of the L1T was written using HLS, unlike the firmware of Phase-1 L1T, as HLS enables physicists with no HDL background to develop prototypes and demonstrate ideas on actual hardware.

Figure 5.1 shows a diagram of the firmware development. Code in HLS usually targets a specific Xilinx device, running at a given clock speed. C++ was the development language of this work. A set of directives can be used to instruct the tool to run various optimisations. More specifically, it is possible to make sectors of an algorithm run in parallel, or to pipeline them. Pipelining is a fundamental technique that enables a piece of firmware to receive new input before previously submitted data has completed processing, enabling for a continuous flow of information to be accepted.

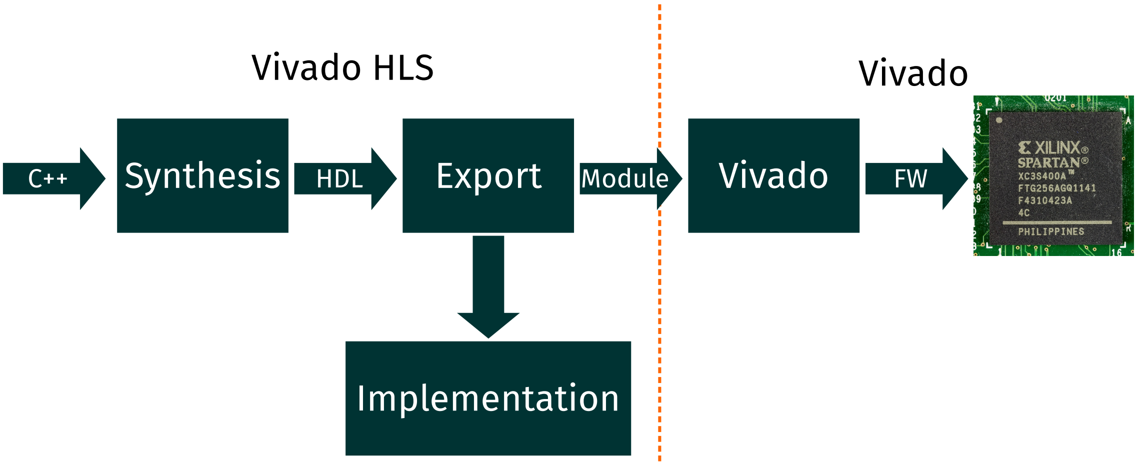

Figure 5.1: Diagram of the firmware development workflow.

A process called synthesis converts code into HDL code. At this stage HLS provides information about the performance of the resulting design. The latency is of particular interest, defined as the number of clock cycles, or time, between the first data in input and the first output. HLS also returns an estimate of the number of FPGA resources that are required to implement the algorithm. This resource usage estimate will be referred to as post-synthesis usage. Post-synthesis usage estimates are typically indicative and can substantially change in the successive steps of development. The HDL code generated by HLS can be exported as a generic HDL module that can be loaded in the Vivado software suite to obtain firmware or to interface it with other HDL modules. Vivado returns the FPGA resources actually used by the firmware once it is produced. This process is quite lengthy and complicated, therefore HLS can also run a simplified version of this workflow which will be referred to as implementation. This process returns a more precise estimate of the resource usage than the synthesis step. Resource usage figures obtained from this

step will be referred to as post-implementation usage.
All the results presented in this chapter were produced using the Vivado HLS and development suite version 2019.2.

5.2 The inputs

The correlator trigger subsystem is split in two layers, as presented in Section 3.3.3.2. The first layer computes particle flow candidates and sends them to the second layer, which reconstructs objects and calculates quantities to trigger on. At the time of writing, the correlator trigger is expected to run using time multiplexing with a period of 6 bunch crossings.
The particle flow algorithm is a local algorithm, as it requires information from a small area close to the particle that is being reconstructed. Therefore, the complexity of the algorithm is reduced in the first layer by splitting the detector into regions and processing each one separately. The region layout at the time the algorithm was developed is shown in Fig. 5.2: dashed lines delimit regions, solid lines group regions that receive input from the same subdetectors together. Regions are processed by six FPGA boards over multiple clock cycles, thanks to time multiplexing. PF candidates in a region are sent to the second layer as soon as processing is finished. Boards are

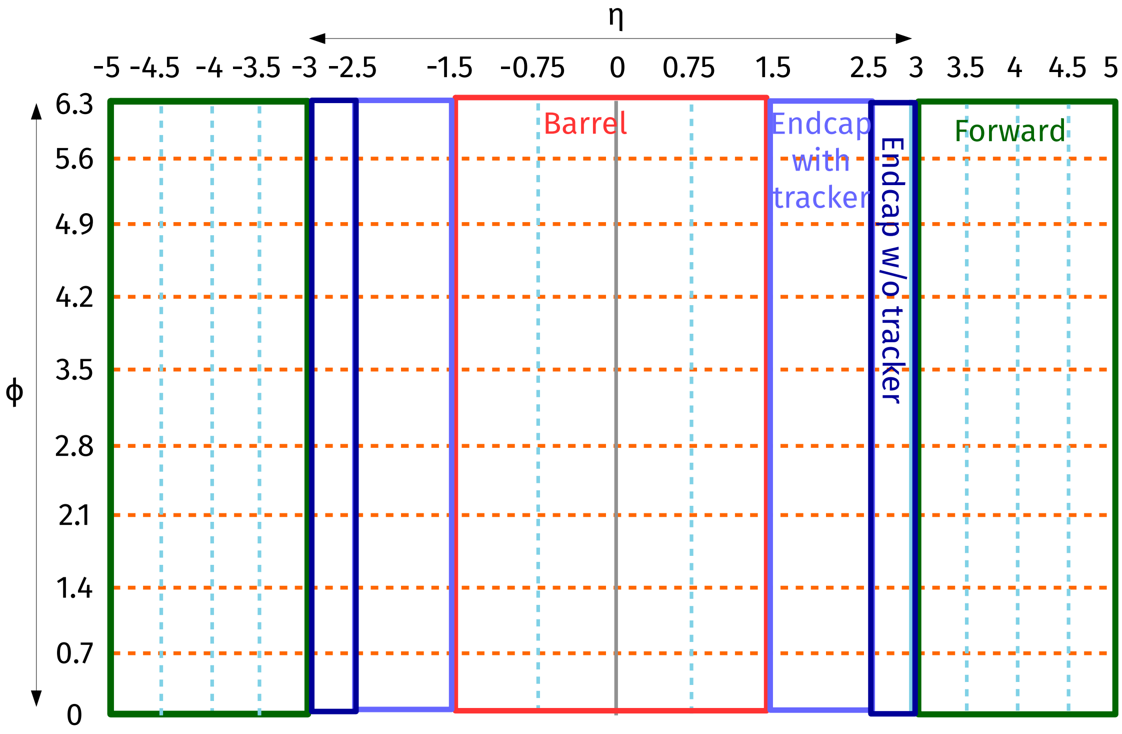

Figure 5.2: Layout of the detector regions used in the particle flow reconstruction in the correlator layer-1 trigger subsystem. Dashed lines delimit regions, solid lines group regions that receive data from the same subdetectors together.

expected to complete analysing one row of regions at the same ϕ before moving to the next one. The specific order was not fully defined at the time this work was done.

In its current implementation, each board can find up to 24 PF candidates per region and send them to the second layer via 28 Gb/s optical links. One 16-bit, and two 10-bit integers are employed to represent the p_{T} , η, and ϕ of each object, respectively. These quantities use integer values to save hardware resources, instead of floating point values in units such as GeV. Conversion from internal units ip_{T}, $i\eta$, and $i\phi$ to "physical" p_{T} , η, and ϕ can be done using:

$$p_{\mathrm{T}} = ip_{\mathrm{T}} \cdot 0.25 \text{ GeV} \qquad \eta = i\eta \cdot 0.00436 \qquad \phi = i\phi \cdot 0.00436 \tag{5.1}$$

The conversion factor from integer to floating point units is referred to as least significant bit. Inputs are sent in relative coordinates, with the origin being in the negative η and ϕ corner of the region.

5.3 Design of the algorithm

The jet trigger algorithm implemented in the CMS simulation was redesigned to fit the requirements of the trigger system. The main difference between the CMS simulation and the actual system is in the way the data is received. In the CMS simulation, a list of all the inputs in an event is immediately available for processing. This enables the algorithm to first produce a histogram of all inputs, then compute jets and sums, and, finally, output the results. This is not the case in the actual trigger. Inputs are sent to the second layer over multiple clock cycles, and divided by regions, as explained in the previous section. Buffering inputs until the full event is received before starting processing is not possible. This solution would nullify the benefits of time multiplexing and require a design able to process a large number of inputs in a short time, which can not fit on the L1T FPGAs.

Therefore, the hardware implementation of the algorithm was redesigned to start processing as soon as enough input data is received to produce output in a streaming fashion. This was achieved by building histograms of the various input regions as they arrived, buffering a limited number of bins, and finding jets as soon as a histogram covering an area larger than a jet has been buffered. This solution has the advantage of reducing the amount of resources required, as the FPGA has to store only small parts of the event and can overwrite memory areas as soon as the information stored in them has been processed.

The jet and sum algorithm was divided in three separate HDL modules connected together as in Fig. 5.3:

Histogrammer: receives inputs in an area of the detector and builds an histogram. Outputs the bin content of the histogram.

Buffer: receives bins from the various areas of the detector, buffers them until a set of bins with the same ϕ covering the entire η range (which will be referred to as ϕ slice) is received. Outputs ϕ slices.

Jet and sum finder: receives ϕ slices, finds jets and computes H_T and $p_\mathrm{T}^\mathrm{miss}$.

Splitting the jet finder algorithm in small blocks facilitates rapid development, as synthesising large firmware designs usually takes long time and can require a prohibitive amount of computing resources. Only one block was developed and tested at the time, thus saving time by not having to synthesise the entire algorithm. The entire chain is pipelined: each block can process new data before it has finished analysing the information previously received, enabling for a continuous stream of inputs to be acquired without interruptions.

Figure 5.3: Diagram showing how the FPGA version of the jet and sum algorithm was organised.

In the next two sections the design and performance of the histogrammer and jet finder will be presented. A Xilinx VU9P FPGAs running at 360 MHz, which is the expected clock speed of the CT boards, was targeted. It will be shown that the two components were designed to be adaptable for a multitude of uses and configurations. The design of the buffer heavily depends on the order in which inputs from the first layer are received. A specific order was assumed in the demonstrator setup. The buffer of the demonstrator will be presented in Section 5.4.2.

5.3.1 The histogrammer

The histogrammer receives PF candidates from the first layer of the correlator trigger and builds pseudo trigger towers by computing an histogram of the η and ϕ positions of the inputs using their p_T as a weight. The firmware runs the following operations for each set of inputs:

1. Each input gets a η and ϕ bin index, η_bin and ϕ_bin, assigned by computing:

   $$\eta_\mathrm{bin} = \mathrm{floor}\left(\frac{i\eta}{\Delta i\eta}\right) \qquad \phi_\mathrm{bin} = \mathrm{floor}\left(\frac{i\phi}{\Delta i\phi}\right) \tag{5.2}$$

   where $\Delta i\eta$ and $\Delta i\phi$ are the bin size in the η and ϕ dimension, respectively.

2. The content of each bin is defined as:

   $$p_\mathrm{T}^\mathrm{bin} = \sum_\mathrm{inputs} \begin{cases} p_\mathrm{T}^\mathrm{input} & \text{if } \eta_\mathrm{bin}^\mathrm{input} \text{ and } \phi_\mathrm{bin}^\mathrm{input} \text{ correspond to bin position} \\ 0 & \text{else} \end{cases} \tag{5.3}$$

3. The resulting bins are output to the next stage of the chain.

The firmware has a configurable number of inputs, N_{inputs}, and bins, N^{η}_{bin} and N^{ϕ}_{bin}. The size of the bins is changeable as well. This enables use of the same histogram logic to create different binning schemes matching the various characteristics of the regions of the detector. In addition, developing a flexible histogram enabled studies of latency and hardware usage for a variety of different configurations, in order to study how these performance metrics scaled and extrapolate them to larger designs.

Figures 5.4(a) and 5.4(b) respectively show the LUT and FF usage of the histogrammer as a function of the number of η bins and inputs. The number of ϕ bins was fixed at eight. The LUT and FF usage linearly scales with the number of η bins and inputs. The usage of these two resources is connected to the total number of additions run by the algorithm in order to build the histogram. For each bin, HLS has to allocate logic for a number of additions equal to the number of inputs in order to compute Eq. 5.3. Therefore, the total number of sums that must be run to fill the histogram is:

$$N_{\text{additions}} = N_{\text{inputs}} \cdot N^{\eta}_{\text{bin}} \cdot N^{\phi}_{\text{bin}} \tag{5.4}$$

This explains the linear scaling of the LUT and FF usage with the number of η bins and inputs. The same scaling was observed as a function of the number of ϕ bins. This limits the usage of this histogrammer to small regions of the detector with a limited number of inputs. However, this design enables a fast and highly-parallelised execution of the histogram fill operation.

Figure 5.4(c) shows that the DSP usage linearly increases with the number of inputs. DSPs are typically used in multiplications and divisions. In this case DSPs were used to obtain the η_{bin} and ϕ_{bin} using Eq. 5.2. Each input requires two DSPs for bin indexing, thus the linear increase.

The algorithm was found to have a latency of 7–8 clock cycles, depending on the number of bins and inputs, corresponding to 19–23 ns at 360 MHz. The design is pipelined, allowing for a new region to be processed every clock cycle, before processing of the previous one was finished.

5.3.2 The jet and sum finder

The firmware of the jet finder was designed to be flexible and configurable in order to match various histogram and jet configurations. In this section, N^{η}_{slice} will be used to refer to the number of bins of a ϕ slice; N^{ϕ}_{jet} will be used to refer to the number used as side of the jet clustering window.

The jet and sum finder is a pipelined firmware component that receives a ϕ slice each clock cycle. A diagram showing an overview of the jet finder logic is shown in Fig. 5.5. The data on which the jet finder is run is held in a temporary cache of size $N^{\eta}_{\text{slice}} \times N^{\phi}_{\text{jet}}$ units, implemented as a shift register in the ϕ dimension. ϕ slices must be sent sorted in ϕ. The jet finder stores ϕ slices in the register for the first N^{ϕ}_{jet} clock cycles, in order to fill the cache. After N^{ϕ}_{jet} clock cycles, the firmware has received a contiguous detector slice large enough to perform jet finding.

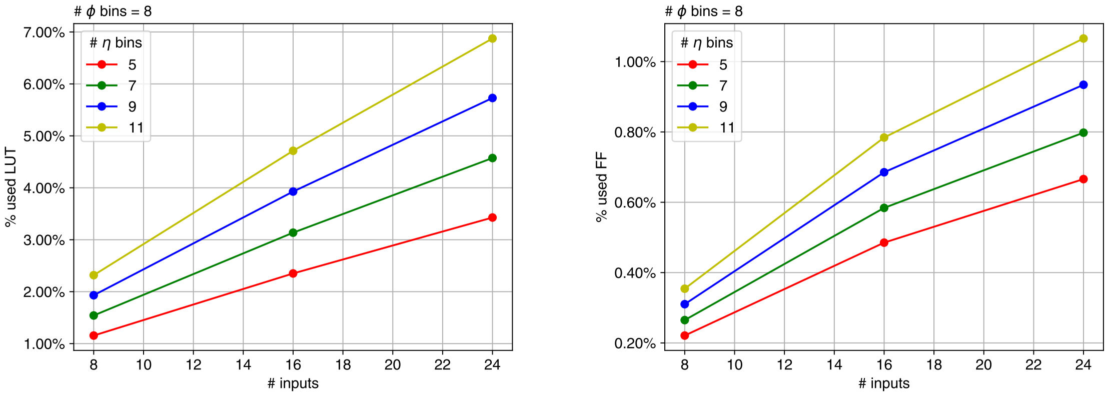

(a) LUT usage

(b) FF usage

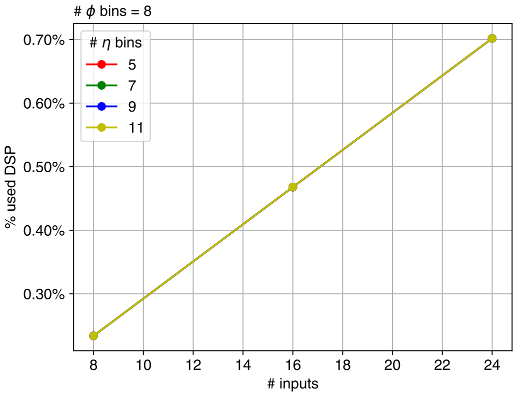

(c) DSP usage

Figure 5.4: Resource usage of the histogrammer as a function of the number of inputs and η bins. The number of ϕ bins was fixed at 8. The LUT and FF usage scales linearly with the number of η bins and inputs. The same linear increase was observed as a function of the number of ϕ bins. DSP usage rises with the number of inputs.

N^{η}_{slice} modules containing memory and logic able to apply the seed mask of Fig. 4.1 to a bin and compute the total energy around it are implemented. Each module is assigned to a different bin in the central ϕ slice of the cache, highlighted in red in Fig. 5.5. Finally, the modules output jets that can be sent to the next stage of the trigger via optical links.

New jets are found every clock cycle as new ϕ slices are received (orange slice in Fig. 5.5) and old ones are overwritten by the shift register (gray slice in Fig. 5.5) until the end of the event. The algorithm stores the first $N^{\phi}_{\text{jet}} - 1$ ϕ slices in an additional cache. These slices are stitched to the ones received in the final part of the event, once all the ϕ slices have been received, in order to find jets around $\phi = \pi$. Jet energy corrections were not implemented in firmware in this prototype, but they can be introduced as a large LUT storing them, as it is currently done in the Phase-1 L1T.

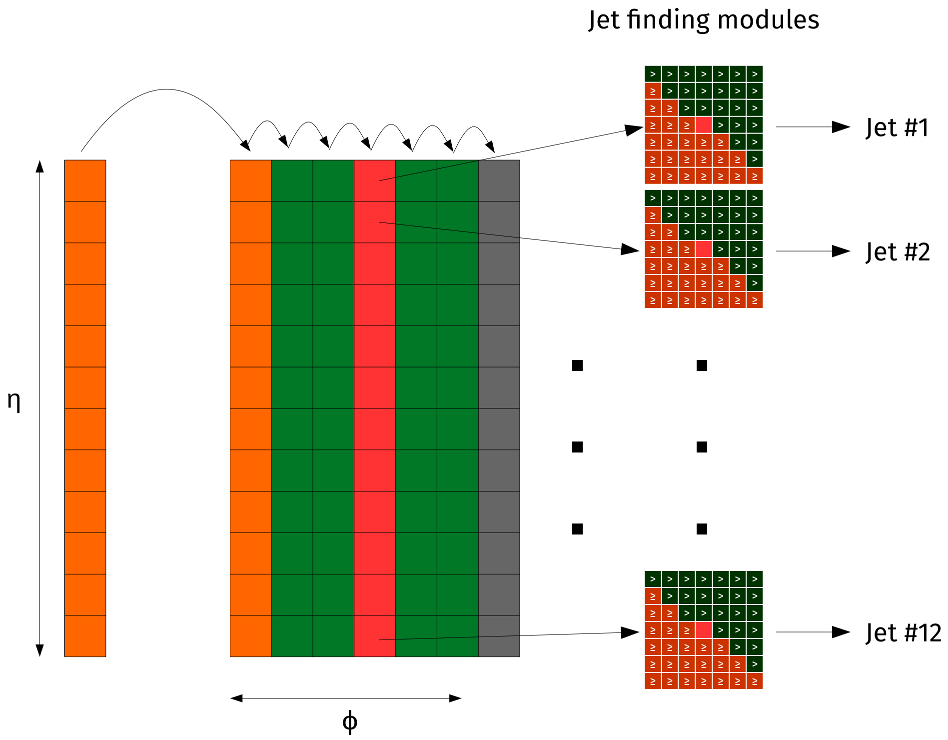

Figure 5.5: Diagram of the jet finder logic. The jet finder cache is implemented as a shift register. Data shifts to the right as new ϕ slices are received. The rightmost slice (gray) is overwritten to make space for the incoming one (orange). The red slice is the ϕ slice where seeds are searched for. A jet finding module is assigned to each bin in the centre of the register.

Jets are saved in a 32-bit word, with a 16-bit and two 8-bit integers holding the ip_T, $i\eta_\mathrm{jet}$, and $i\phi_\mathrm{jet}$, respectively. The η_bin and ϕ_bin of the jet seed are saved as its coordinates.

Sums were implemented by having three registers. Two of them store the total p_x and p_y in the event ($p_\mathrm{x,tot}$ and $p_\mathrm{y,tot}$) from histogram bins as ϕ slices are received. Another register stores the total H_T after jets are found. The total p_x and p_y of ϕ slice are obtained by first computing its total p_T and then multiplying it by the corresponding sine and cosine, which are stored in LUTs. The $p_\mathrm{T}^\mathrm{miss}$ is obtained by computing $E_\mathrm{T}^\mathrm{miss} = \sqrt{p_{x,\mathrm{tot}}^2 + p_{y,\mathrm{tot}}^2}$, which involves computing a square root. Computing a square root on a FPGA is not a trivial operation. The coordinate rotation digital computer (CORDIC) algorithm [96] was used. CORDIC is an iterative method that computes the square root by running a constant number of successive approximations.

Figure 5.6 shows the LUT and FF usage of the jet and sum finder as a function of the number of η bins, i.e. the size of the ϕ slice, and the jet size. A number of jet finder modules equivalent to the size of the incoming ϕ slice must be allocated in the FPGA. Consequently, the LUT and FF usage linearly increases with the number of η bins. The number of comparison and additions required to find a jet scales with the area of the jet, hence the LUT and FF usage scales with the window size. The jet finder also uses 4 DSP units. Two of them are required in order to multiply the total p_T of

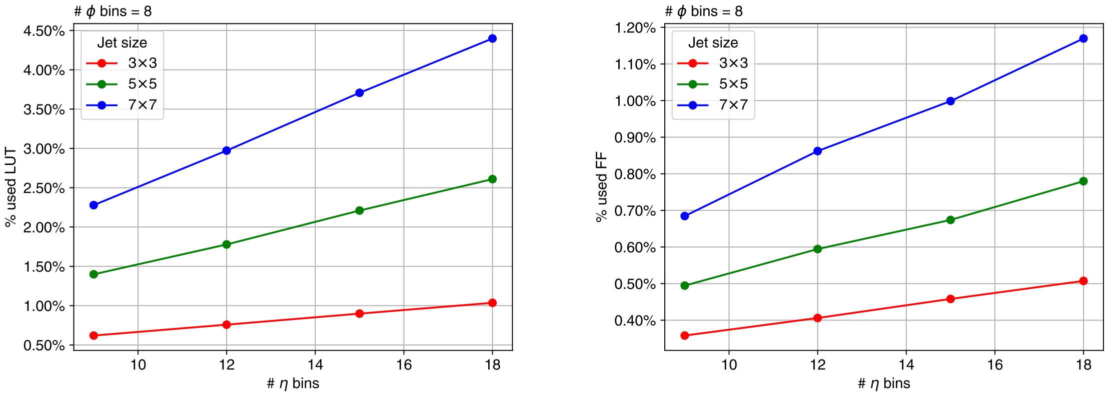

(a) LUT usage (b) FF usage

Figure 5.6: Resource usage of the jet and sum finder as a function of the number of η bins and jet size. The number of ϕ bins was kept constant at 8. The LUT and FF usage scales linearly with the number of η bins, quadratically with the jet size. No dependence on the number of ϕ bins was observed.

a ϕ slice by the relative sin and cos value and break it down in its x and y components. The other two are used to compute the squares in $E_{\mathrm{T}}^{\mathrm{miss}} = \sqrt{p_{x,\mathrm{tot}}^2 + p_{y,\mathrm{tot}}^2}$. The CORDIC algorithm uses only LUTs and FFs as the algorithm computes the square root via bitshift operations. Increasing the number of ϕ bins does not affect resource usage, since this just increases the number of ϕ slices and the total time required to process a single event. The latency of the algorithm, defined as the number of clock cycles between the first input and the first output, was found to be around 50 clock cycles for jets built using a window made of 9×9 bins, corresponding to ~ 139 ns at 360 MHz.

5.4 The jet trigger demonstrator

The proof-of-concept demonstrator will be presented in this section. The goal of the demonstrator is to show that the algorithm can be loaded in hardware, and verify that it produces correct results. Building the demonstrator enables discovering and investigating issues and difficulties that may be encountered when preparing the final version of the algorithm. A Serenity board hosting a Xilinx KU15P FPGA, running at 240 MHz was used (Fig. 5.7). A conservative clock speed was selected in this first prototype.

5.4.1 Inputs

PF candidates in the η range 0–1.5 and ϕ range 0–0.7 of the detector, corresponding to a part of its barrel, were used to demonstrate the capabilities of the jet finder. According to Fig. 5.2, this area is divided to two regions:

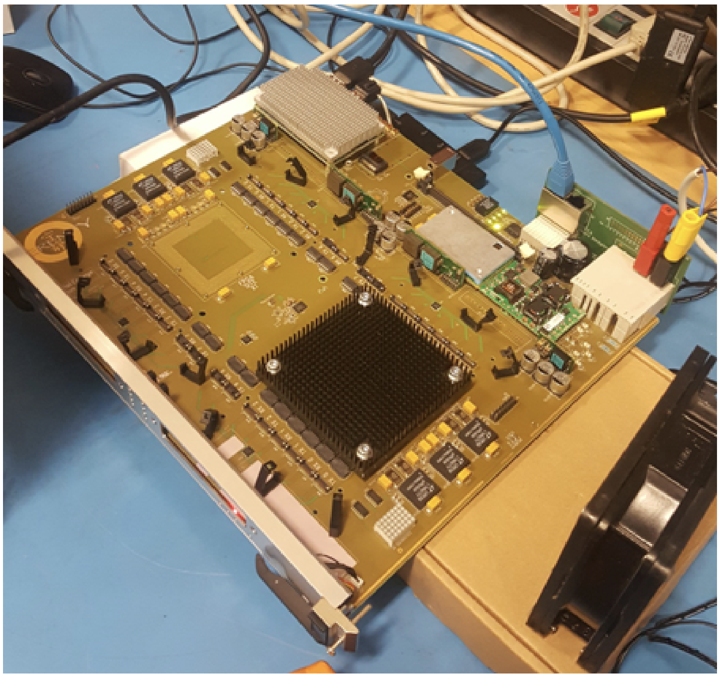

Figure 5.7: A picture of the Serenity board located in the laboratory of the University of Bristol that was used to run the demonstrator algorithm. The board hosts a Xilinx KU15P FPGA.

Region 1: $0 \leq \eta < 0.75$ and $0 \leq \phi < 0.7$.

Region 2: $0.75 \leq \eta < 1.5$ and $0 \leq \phi < 0.7$.

Inputs in the first region were sent in the first clock of each event, and inputs in the second region in the successive one. A larger region could not be investigated due to the long time and large amount of memory required to produce the firmware.

5.4.2 Implementing the jet trigger demonstrator

The jet trigger was set up to reconstruct jets with the 0.6×0.6 jet configuration presented in Section 4.3.

The histogrammer was configured to bin each region in 9×8 bins in $\eta \times \phi$. Bin were 19×20 internal units big, corresponding to 0.083×0.087 in the physical $\eta \times \phi$ when converted with Eq. 5.1.

A buffer was built to receive bins from the two regions, which are sent by the histogrammer over two consecutive clock cycles, and connect them together side-to-side in a single memory area. The ϕ slices resulting from uniting the histograms are sent sorted in ϕ in ascending order over eight clock cycles, i.e. the total number of ϕ bins.

The jet finder was configured to work with a 18×8 histogram, i.e. resulting histogram size in the buffer, by receiving ϕ slices that are 18-bin long. The 7×7 bin window size was selected, which is equivalent to the 0.6×0.6 jet configuration in Section 4.3. The window made of 9×9 bins, corresponding to the 0.8×0.8 jet configuration in Section 4.3, could not be used to cluster jets due to the limited size of the histogram in the ϕ direction.

Post-synthesis and post-implementation resource usage estimates of each algorithm component obtained from HLS are shown in Table 5.1 together with the latency. The total latency of the algorithm is 57 clock cycles.

The three algorithm modules were linked together, integrated within the EMP framework to interface with the board components, and imported in Vivado to generate firmware to load on the Serenity board in Fig. 5.7. Figure 5.8 shows the floorplan of the FPGA logic. The blue area represents the physical location of the FPGA resources that are used by the firmware. The red rectangle with the label "payload" highlights the area taken by the logic of the jet trigger algorithm. The resource usage of the algorithm is shown in the "Firmware" row of Table 5.1. The resources used by the EMP framework are not included in this number as they do not depend on the algorithm. The table shows that synthesis typically over-estimates the LUT and FF usage, sometimes by a significant margin. On the other hand, the post-implementation estimates obtained from HLS appear to quite accurate, as the predicted figure is very close to the one actually used by the generated firmware.

Table 5.1: Latency and estimated resource usage broken down in each component of the jet trigger demonstrator running on a Xilinx KU15P FPGA at the frequency of 240 MHz. The sum of the three components is shown under the "Total" row. The resources actually required by the algorithm firmware on a board are shown in the "Firmware" row.

Component	Latency	Synthesis			Implementation		
		DSPs	FFs	LUTs	DSPs	FFs	LUTs
Histogrammer	6	2.4%	1.8%	12%	2.4%	1.5%	6.3%
Buffer	6	0%	2.5%	20%	0%	1%	1.7%
Jet finder	45	0.2%	2.7%	9.9%	0.2%	1.8%	4.1%
Total	**57**	**2.6%**	**7%**	**24%**	**2.6%**	**4.3%**	**12.1%**
Firmware	**57**				**2.6%**	**4.3%**	**12.0%**

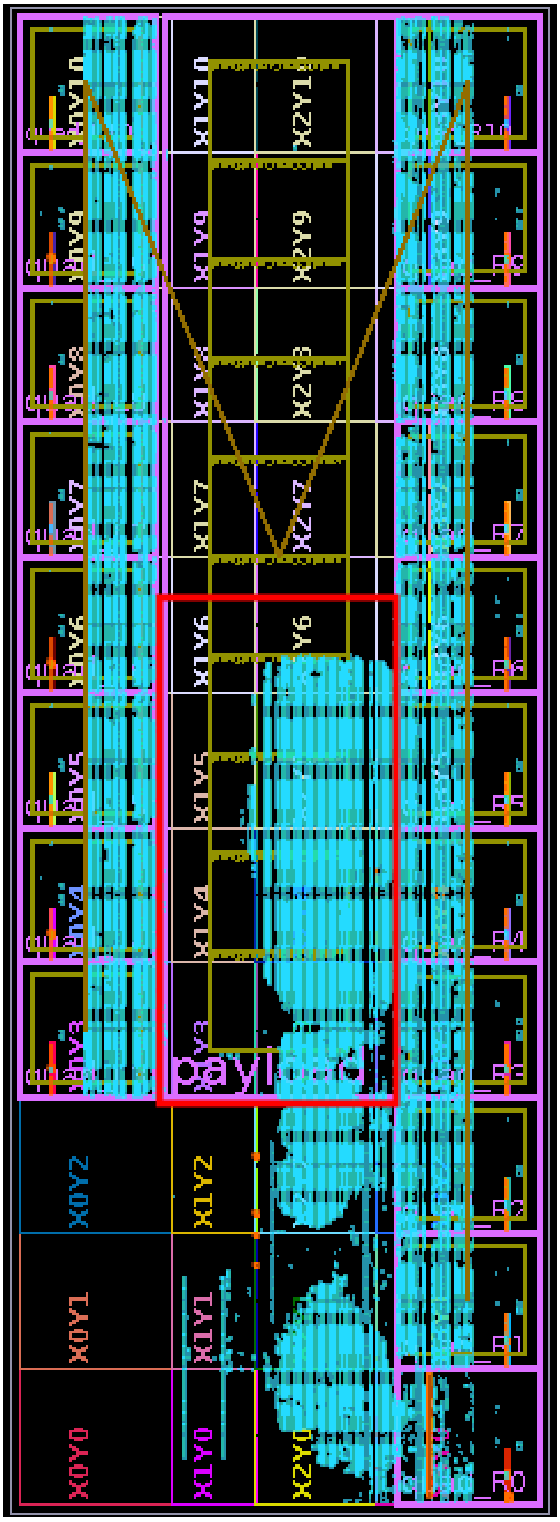

Figure 5.8: Floorplan of the jet trigger algorithm integrated with the EMP framework on the Xilinx KU15P used as a demonstrator. The blue region inside the red “payload” rectangle is the area containing the jet trigger algorithm logic. Result produced by author with the collaboration of Aaron Bundock, Emyr Clement, and Katie Walkingshaw-Pass.

5.4.3 Validation of the jet trigger algorithm demonstrator

The output of the demonstrator was validated by comparing it to the results of the jet and sum algorithm emulator implemented in the CMS simulations run on the same events. The CMS simulation was adjusted to find jets and compute sums only over the demonstrator region. Calibrations were not applied to jets. PF candidates from 50000 $t\bar{t}$ events at pile-up 200, of which 28000 had at least one PF candidate in one of the two regions, were run in both CMS simulation and demonstrator board.

The output jets and sums from the hardware and software algorithm versions were compared and differences between the two used to understand and fix bugs until a satisfactory agreement was obtained. Figure 5.9 shows the final p_{T} , η, and ϕ distributions of jets for both hardware and emulator. Figure 5.10 displays the same type of comparison for $p_{\mathrm{T}}^{\mathrm{miss}}$ and H_{T} .

The jet and sum agreement rate was obtained in events with at least a reconstructed jet or a non-zero sum, based on the algorithm under verification. The jet output of a event from the hardware was considered to be in agreement with the one from the emulator if every jet in the hardware output was cross-matched with $\Delta R < 0.01$ to a jet in the emulator output and had identical momentum. The hardware and emulator H_{T} were considered in agreement in an event if identical; as for $p_{\mathrm{T}}^{\mathrm{miss}}$, hardware and emulator were considered in agreement if their difference was lower than 1 GeV. The jet, $p_{\mathrm{T}}^{\mathrm{miss}}$, and H_{T} agreement rate was found to be 95.0%, 94.8%, and 97.7% respectively.

The remaining events in disagreement were investigated. The main remaining source of disagreements was found to be in the different variable type used to represent the η and ϕ position of the PF candidates in the emulator and firmware. This discrepancy caused some inputs in the emulator to be assigned to an adjacent bin to that assigned in the firmware. In addition, less than 1% of events were found to have more than 24 inputs per region, which is greater than the designed maximum amount of inputs, as explained in Section 5.2. The emulator does not include input truncation, leading to a different behaviour compared to the hardware. Inputs are expected to be sent sorted by p_{T} in the future, reducing the amount of energy lost by truncating the input list.

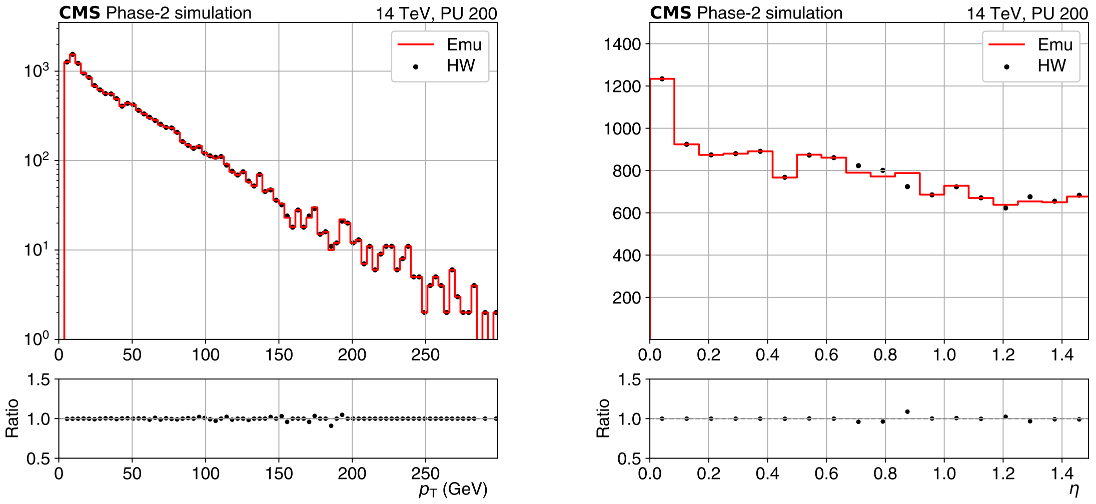

(a) p_{T}

(b) η

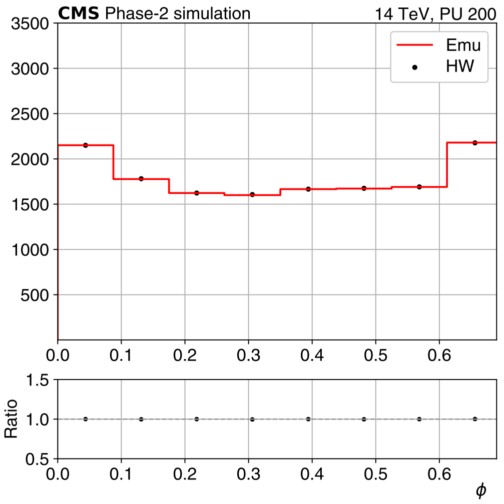

(c) ϕ

Figure 5.9: Hardware-emulator comparison of the p_{T} , η, and ϕ distributions of jets in ~ 28000 $t\bar{t}$ events at pile-up 200. An agreement rate of 95.0% was achieved. Results produced by author with the collaboration of Aaron Bundock, Emyr Clement, and Katie Walkingshaw-Pass.

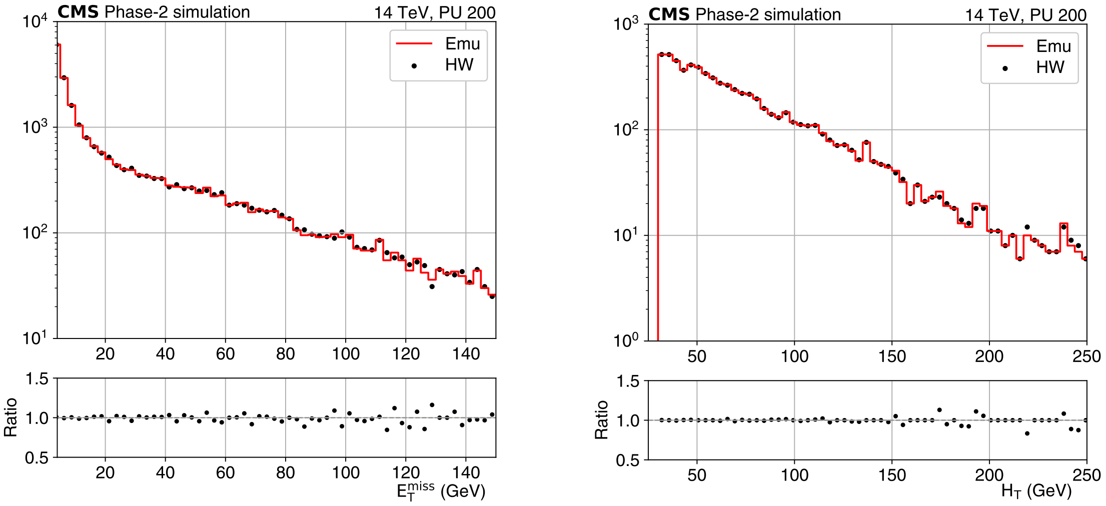

(a) p_T^{miss}

(b) H_T

Figure 5.10: Hardware-emulator comparison of p_T^{miss} and H_T distributions in $\sim$ 28000 $t\bar{t}$ events at pile-up 200. An agreement rate of 94.8% and 97.7% was achieved for p_T^{miss} and H_T , respectively. Results produced by author with the collaboration of Aaron Bundock, Emyr Clement, and Katie Walkingshaw-Pass.

5.5 Scaling to the final design

An estimate of the resource usage of the full-detector version of the jet and sums trigger algorithm was obtained by combining the results from the demonstrator usage in Section 5.4.2 and the scaling shown in Sections 5.3.1 and 5.3.2.
Estimates were computed from the post-implementation usage estimates of the demonstrator design obtained from HLS targeting a Xilinx VU9P FPGA running at 360 MHz. Usage figures of each component were scaled to the full-detector version based on the following criteria:

Histogrammer: The first layer or the correlator trigger is expected to process four regions in parallel, therefore four histogrammers will be required. The size of the region changes based on the detector area and is binned using 6×8, 9×8, or 12×8 bins in the $\eta \times \phi$ space based on the region size. If appropriate load balancing is used, it is expected that each histogrammer will require the amount of resources of a 9×8 histogrammer on average. Consequently, the final usage of this component was be obtained by multiplying by four the usage of the 9×8 histogrammer used in the demonstrator.

Buffer: The buffer logic strongly depends on the order the input regions are sent to the second layer, which must be defined in order to predict the hardware usage. In first approximation the usage can be assumed to linearly depend on the detector area covered by the buffer.

Jets built using a 7 × 7 bin window requires a row of regions at the same ϕ to be buffered in order to run, i.e. an area that covers 120 × 8 bins in $\eta \times \phi$. The buffer will have to be eight times bigger than the one used in the demonstrator. A even larger buffer will be required in order to find jets with a 9 × 9 bin window. This corresponds to the 0.8 × 0.8 jet configuration, which has the best reconstruction performance. The buffer will have to store 120 × 16 bins in order to run the algorithm. The resource usage of this configuration is difficult to predict, as figures might not linearly scale. Therefore, usage estimates for 9 × 9 jets were not obtained.

Jet finder: The jet finder must process a number of ϕ slices that depends on the time multiplexing period. The shorter the time multiplexing period is, the more data needs to be processed by the jet finder in order to fit time constraints, thus increasing usage. A time multiplexing period of six bunch crossings corresponds to 54 clock cycles at 360 MHz. The entire calorimeter histogram must be sent to the jet finder within this time limit. The histogram is made of a total of 8640 bins, requiring at least 160 bins to be sent per clock cycle to the jet finder. The jet finder receives bins in ϕ slices, which are made of 120 bins in the full design. Two ϕ slices per clock cycle will have to be sent to the jet finder in order to fit in the time limits, corresponding to 240 bins per clock. The FF and LUT usage of the jet finder linearly increases with the size of the ϕ slice and the same can be assumed for the number of ϕ slices in input. In conclusion, the FF and LUT resource usage of the full-scale algorithm was obtained from the demonstrator by scaling by the number of bins in input per clock cycle, i.e. $240/18 \approx 13.3$. As for the DSP usage, two DSPs are required per ϕ slice to break down the total p_{T} of each slice in its component, and two to calculate $p^2_{x,\mathrm{tot}}$ and $p^2_{y,\mathrm{tot}}$. Consequently, a usage of six DSPs was considered.

Table 5.2 shows the latency and post-implementation resource usage estimates of the demonstrator design running on a Xilinx VU9P FPGA at the frequency of 360 MHz, together with the corresponding full-detector FPGA usage projections. The final design is expected to use 41.5% of LUTs, 11.6% of FFs, and 2.9% of DSPs of a Xilinx VU9P FPGA. The total latency of the full-scale algorithm is expected to be between 60 and 70 clock cycles at 360 MHz, i.e. 167–195 ns.

Table 5.2: Latency, estimated post-implementation resource usage, and full-detector design projections of each component of the jet and sum trigger. A Xilinx VU9P FPGA running at the frequency of 360 MHz was targeted. The sum of the three components is shown under the “Total” row.

Component	Latency	Demonstrator			Full detector		
		DSPs	FFs	LUTs	DSPs	FFs	LUTs
Histogrammer	7	0.7%	0.7%	2.6%	2.8	2.6%	10.3%
Buffer	6	0%	0.5%	0.7%	0%	4.1%	5.8%
Jet finder	47	0.1%	0.7%	1.9%	0.2%	4.9%	25.4%
Total	**60**	**0.8%**	**1.9%**	**5.2%**	**2.9%**	**11.6%**	**41.5%**

5.6 Future work

Future improvements to the algorithm should focus on: optimising its design to reduce its high LUT usage; developing the 0.8×0.8 jet algorithm; preparing a multi-board demonstrator; testing the algorithm at 360 MHz.

A significant fraction of LUTs are used to run additions and comparisons in the histogrammer and jet finder, hence the number of these operations must be reduced in order to save LUTs. Both histogrammer and the jet finder run redundant sums and comparisons, therefore there is potential for further optimisations that can reduce the usage. The number of sums run by the histogrammer can be computed using Eq. 5.4 and is much larger than the number of inputs, which is the minimum number of sums required to fill the histogram. This strategy used in implementing the histogrammer enables for a low-latency and highly-parallelised histogram fill, at the cost of a significant increase in the LUT usage. The number of additions can be reduced by filling an histogram with fewer inputs in parallel. A temporary input buffer is required to do this, as the histogrammer has to save the inputs that have not yet been added. Future work should investigate this strategy and verify that the overhead of an input cache is lower than the resources required by a fully-parallel histogram fill.

The LUT usage of the jet finder could be improved by reducing the number of jet finder modules used in the design. The current implementation of the jet finder assigns a jet finder module to each bin in the centre of the component's cache. However, the actual maximum number of jets that can be found in the cache is much lower than the implemented number of jet finder modules. For instance, a maximum of five jets built with a 7×7 bin window can be found in the 7×18 internal memory of the component. Therefore, the algorithm could be redesigned to reduce the number of redundant comparisons and additions, saving LUTs.

Implementing a 9×9 jet finder, corresponding to the 0.8×0.8 jet configuration, is more complicated than developing a 7×7 one due to the larger buffer size. Increasing the buffer size using HLS was not possible due to the substantial computing resources that the tool required to perform this operation. For the same reason it was not possible to develop of a demonstrator able to find jets on a larger area. Computational limits might be overcome by redesigning the buffer, or by splitting it into smaller units which can be independently produced by the tool. Alternatively, this component could be implemented using a hardware description language such as VHDL, which might be the best solution, as HDLs are typically more suited for buffering and routing data.

Preparing and testing a demonstrator setup where multiple boards from different trigger subsystems are connected together via optical links is a fundamental step towards understanding the performance of the system and solving wider trigger issues. An initial test with a multi-board demonstrator was set up by loading the particle-flow algorithm running on the first layer of the correlator trigger onto a Serenity board and connecting it via optical links to another Serenity board running the histogrammed jet algorithm. Three consecutive $t\bar{t}$ events out of fifty output from the demonstrator were in agreement with the emulator. The results indicate that a temporary communication problem had occurred, and suggest that the boards successfully synchronised for a brief period, as few events were successfully processed. Future work should be put in investigating the issue and produce a multi-board system with a higher agreement rate. Finally, the demonstrator was configured to run at 240 MHz, as a conservative clock speed. The final design is expected to run at 360 MHz. Future tests should confirm that the demonstrator returns correct results at the increased clock frequency.

5.7 Conclusions

The implementation in hardware of a trigger algorithm able to find jets and compute $p_{\mathrm{T}}^{\mathrm{miss}}$ and H_{T} was presented in this chapter. The firmware resource usage was understood, and strengths and weaknesses of the algorithm identified. A demonstrator system running the 0.6×0.6 version of the jet trigger algorithm on a section of the CMS detector was prepared and implemented on a Xilinx KU15P FPGA. Its output was validated against software emulation in CMS simulations, obtaining an agreement rate of 95.0%, 94.8%, and 97.7% for jets, $p_{\mathrm{T}}^{\mathrm{miss}}$, and H_{T} , respectively. Disagreements were found to be mainly caused by the different representation of the position of the inputs in the hardware and emulator.

The latency and resource usage estimates of the 0.6×0.6 jet trigger algorithm running on the full detector were obtained for a Xilinx VU9P FPGA running at a clock frequency of 360 MHz. The algorithm is expected to use around 42% LUTs, 12% FFs and 3% DSPs; a latency between 167 and 195 ns is expected. Possible optimisations to reduce LUT usage, and strategies to implement the 0.8×0.8 jet algorithm were discussed and presented.

CHAPTER 6

TRIGGERS AT THE FUTURE CIRCULAR COLLIDER HADRON COLLIDER

The trigger studies undertaken for the Future Circular Collider (FCC) in hadron configuration will be presented in this chapter. An introduction to the FCC projects will be given in Sections 6.1 and 6.2, in which the technical specifications of the projects with their physics goals will be presented. In Section 6.3, challenges that the trigger and data acquisition have to face at the FCC will be introduced. Two different estimates of trigger rates obtained with different methods will be described in Sections 6.4 and 6.5 alongside with their impact on the physics reach of a proposed particle detector at FCC-hh. Finally, possible solutions to the triggering problem based on the projected trigger rates will be discussed.

6.1 The FCC-ee and FCC-eh projects

The FCC is a 100-km long particle collider project that will operate in the post-LHC era [3, 4]. A schematic of the accelerator complex is shown in Fig. 6.1: the system will exploit the preexisting infrastructure at CERN to accumulate and boost particles before injecting them in the FCC accelerator ring. Three possible collider options are under consideration: an electron-positron collider (FCC-ee), a proton-proton collider (FCC-hh) and a proton-electron collider (FCC-eh). This work focuses on the proton-proton collider, which will be presented in a more extensive manner in Section 6.2.

6.1.1 FCC-ee

FCC-ee will collide e^+e^- at $\sqrt{s}$ in the 88 – 365 GeV range. Four collision energy regimes are of particular interest: $\sqrt{s} \approx 91$ GeV, corresponding to the Z pole; $\sqrt{s} > 160$ GeV, corresponding

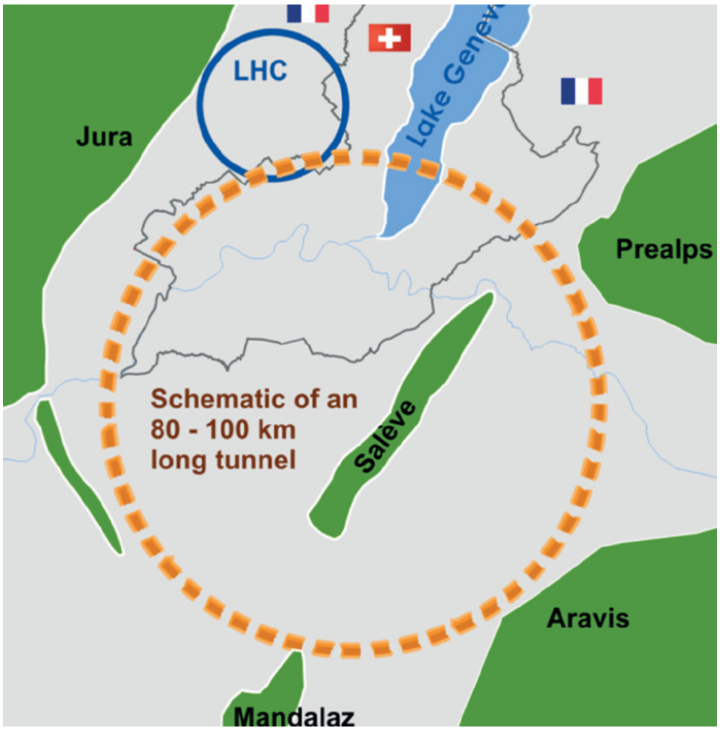

Figure 6.1: Schematic of the FCC accelerator and potential location. Taken from Ref. [3].

to the $W^{\pm}$ pair-production threshold; $\sqrt{s} \approx 240$ GeV, corresponding to the peak cross section of the ZH production; $\sqrt{s} > 340$ GeV, corresponding to the $t\bar{t}$ pair-production threshold. Due to power limitations coming from synchrotron radiation losses, the instantaneous luminosity must be reduced as the centre-of-mass energy increases. The minimum peak $\mathscr{L}_{\text{inst}}$ will be 1×10^{34} cm^{-2} s^{-1} using $\approx$ 30 bunches at $\sqrt{s} \approx 340$ GeV, two orders of magnitude higher than the peak LEP2 instantaneous luminosity of 1×10^{32} cm^{-2} s^{-1} obtained using 4 bunches [14]. At the Z pole, where the maximum peak $\mathscr{L}_{\text{inst}}$ is achieved, FCC-ee will deliver $\mathscr{L}_{\text{inst}} \approx 2.3 \times 10^{36}$ cm^{-2} s^{-1} using $\approx$ 16000 bunches.

FCC-ee will open the possibility for a large set of precision electroweak and Higgs physics measurements to be performed in a controlled, well-predicted environment. New physics process that couple to the electroweak bosons produce small perturbative corrections to observables predicted by the Standard Model. FCC-ee will enable experiments to substantially reduce the uncertainty on these observables in order to increase the sensitivity to these deviations from the theory. At the Z pole, FCC-ee will be able to produce 10^5 times more integrated luminosity that at LEP, potentially reducing the statistical uncertainties to 300 times less than at LEP. At the $W^{\pm}$ pair production threshold, FCC-ee is expected to achieve a precision of 0.5 MeV and 1.2 MeV on the W boson mass and decay width, respectively. At the $t\bar{t}$ pair production threshold, a precision of 17 MeV and 45 MeV for the top-quark mass and decay width will be achievable. During the FCC-ee operation at least one million Higgs boson will be produced in order to push the statistical uncertainty on its properties down to at least few per mil and be sensitive to correction to the Higgs couplings. Additional details on the physics program of FCC-ee can be found in Ref. [4].

6.1.2 FCC-eh

FCC-eh will collide 60 GeV electrons with 50 TeV protons; the centre-of-mass energy will be 3.5 TeV. This collider can operate during the same time span as FCC-hh. Its high energy and instantaneous luminosity will enable a broad set of goals to be achieved: precision QCD and parton distribution function measurements; Higgs boson measurements; precision electroweak and top physics measurements; new particle discoveries. More details on FCC-eh can be found in Ref. [3].

6.2 FCC-hh experiment

The FCC-hh [3] accelerator will be equipped with 16 T dipoles to steer and collide protons at $\sqrt{s} = 100$ TeV . In the first years of operation FCC-hh will deliver $\mathscr{L}_{\text{inst}} = 5 \times 10^{34}$ cm^{-2} s^{-1} and $\langle \text{PU} \rangle \approx 200$. In its second phase, the instantaneous luminosity will be increased up to 30×10^{34} cm^{-2} s^{-1}, corresponding to $\langle \text{PU} \rangle \approx 1000$. Protons will be initially accumulated and boosted by the SPS and LHC, and later transferred to the FCC-hh in order to reach the final collision energy and luminosity. In the current design, collisions will be delivered to two high-luminosity experiments and to two other experiments located at the injection points, similarly to the LHC design. In this section an overview of the FCC-hh goals, physics, and detector design will be given.

6.2.1 QCD physics at FCC-hh

Minimum bias events dominate the central region of particle detectors in terms of object production, as described in Section 2.2.2.1. By combining estimates from many physics generators using different event production techniques, the total inelastic cross-section at FCC-hh is predicted to be $\sigma_{\text{inel}} = 105.1 \pm 2.0$ mb [97], around 35% higher that measured at LHC, which is 78.1 ± 3.0 mb [48]. Particle multiplicity in the central region at $\sqrt{s} = 100$ TeV is expected to almost have a twofold increase compared to $\sqrt{s} = 13$ TeV, with the former being $\left.\frac{\text{dN}_{\text{ch}}}{\text{d}\eta}\right|_{\eta=0} = 9.6 \pm 0.2$ [97] and the latter being $\left.\frac{\text{dN}_{\text{ch}}}{\text{d}\eta}\right|_{\eta=0} = 5.31 \pm 0.18$ [98]. The average transverse momentum in the $|\eta| \approx 0$ region is expected to be $\langle p_{\text{T}} \rangle \approx 0.76 \pm 0.07$ GeV, 40% higher than at $\sqrt{s} = 8$ TeV, which is $\langle p_{\text{T}} \rangle \approx 0.55 \pm 0.16$ GeV. Events at FCC-hh will have around 35% more pile-up interactions and around 270% higher particle density than events at the same $\mathscr{L}_{\text{inst}}$ at 13 TeV at LHC. At $\mathscr{L}_{\text{inst}} = 30 \times 10^{34}$ cm^{-2} s^{-1}, around 100 thousand charged particle tracks per bunch crossing are expected, representing an extreme background environment in which signals will have to be identified.

6.2.2 Goals

Obtaining an accurate measurement of the Higgs boson properties is of primary importance at FCC-hh. In particular, obtaining an accurate estimate of the Higgs boson cubic self coupling via the pair production of Higgs bosons is of specific interest. The cross section of this process at $\sqrt{s} = 100$ TeV is $\sigma_{\mathrm{gg}\to\mathrm{HH}} \approx 1.2$ pb [99], 40 times larger than at $\sqrt{s} = 13$ TeV [60]. Despite the higher energy, the cross section remains small, requiring a large integrated luminosity in order to reach sufficient statistical significance. By the end of their operation, experiments at FCC-hh are expected to have collected a combined integrated luminosity of 30 ab^{-1}. This is to be compared with the expected total from LHC, 3 ab^{-1}. The higher integrated luminosity and cross section will be sufficient to obtain a measurement with 5% precision on the Higgs boson cubic self coupling and will enable a broad range of studies and searches for new physics at this energy scale to be performed.

New frontiers for direct and indirect discovery of dark matter and new particles will be open thanks to the higher energy and large dataset. Weakly interacting massive particles whose mass is too large to be observed at the LHC may be produced; the precision of the SM parameters measured at the HL-LHC may be improved to search for deviations from their predictions. Studies have shown that a five fold increase in the discovery reach for SUSY particles compared to HL-LHC is expected [3, 100].

6.2.3 FCC-hh detector

As discussed in Section 2.3.2, design choices for a detector operating at $\sqrt{s} = 100$ TeV were led by the physics at this energy. Figure 2.11 [59] displays a comparison of the pseudorapidity distribution at 14 and 100 TeV for two interesting physics signals. Figure 2.11(a) shows the distribution of the most forward lepton in events containing a Higgs boson decaying into four leptons; Fig. 2.11(b) shows the distribution of the most forward jet in events containing a Higgs boson produced via vector-boson fusion. Both distributions show that the interesting physics tends to be located at higher pseudorapidity as the centre-of-mass energy increases. Therefore, the detector must cover a higher η range in order to measure interesting physics events and fulfil the FCC-hh physics program. A reference physics detector for FCC-hh was designed, based on the ATLAS, CMS, and LHCb detectors [3], and is shown in Figs. 6.2 and 6.3. The detector is 50 m long and has a diameter of 20 m. The central part of the detector covers up to $|\eta| = 2.5$ and features a 4 T solenoid with a diameter of 10 m. The tracking system, the electromagnetic (ECAL) and the hadron (HCAL) calorimeter are contained within the solenoid. A barrel muon system is located outside the central solenoid. Two forward detector systems are located along the beam line, similar to LHCb, extending the detector coverage to $|\eta| = 6$. Each forward system features: a 4 T solenoid with a inner radius of 2.5 m containing the forward tracker; a forward electromagnetic and hadron calorimeter; a forward muon system. The tracking system is designed to provide fine granularity in order to deal with the high particle density. The tracker must be able to separate

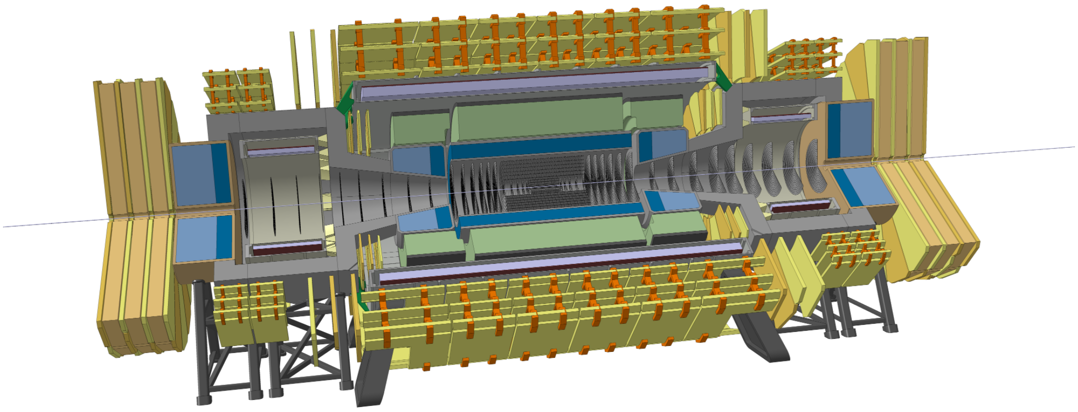

Figure 6.2: Design of the FCC-hh reference detector. Taken from Ref. [3].

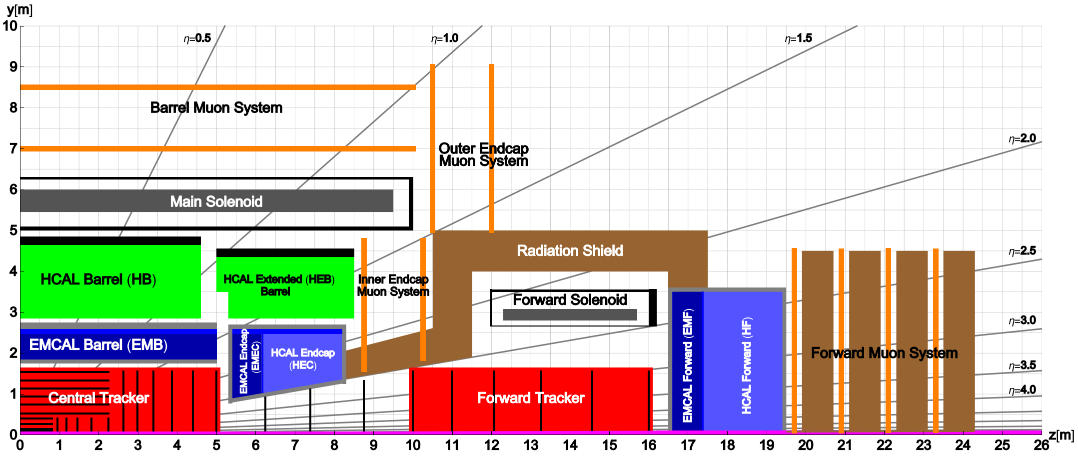

Figure 6.3: 2D cross-section diagram of the FCC-hh reference detector. Taken from Ref. [3].

tracks, and have good vertex and momentum resolution. The ECAL, the endcap HCAL and the forward HCAL are based on liquid argon due to its radiation hardness, while the barrel HCAL uses scintillating tiles with steel and lead absorbers. Muon systems are designed to run more as a identification system, with less focus on its standalone performance, due to the excellent performance of the inner tracking system which provides a good momentum resolution when used in combination with the muon chambers.

6.3 Triggering at FCC-hh

Figure 1.1(a) and Table 6.1 respectively show the cross-section and the rates of a few interesting standard model processes at FCC-hh compared to HL-LHC. A typical event at $\langle \text{PU} \rangle \approx 1000$ at FCC-hh will be extremely busy: each bunch crossing is expected to generate around 20 $\mathrm{b\bar{b}}$ pairs and three jets with $p_\mathrm{T} > 50$ GeV. High granularity detectors that produce large amount of data will be required at FCC-hh in order to reconstruct events with the required precision. Around 10 Pb/s of data are expected to be produced by the detector, if read at the full bunch crossing rate [101]. The FCC-hh trigger systems will have to face the arduous task of maintaining identification capabilities similar to or better than the ATLAS and CMS trigger systems in events with an occupancy at least ten times higher than at LHC. New more sophisticated algorithms using state-of-the-art technology and the full granularity of the detector, as well as innovative triggering strategies and architectures will have to be developed to face this challenge.

Table 6.1: Rates of a few interesting physics processes at different energy and luminosity values. Taken from Ref. [3].

Process	Unit	HL-LHC $\sqrt{s} = 14$ TeV	Phase-1 FCC-hh $\sqrt{s} = 100$ TeV	Phase-2 FCC-hh $\sqrt{s} = 100$ TeV
$\mathrm{b\bar{b}}$	MHz	25	125	750
$\mathrm{b\bar{b}}$ $p_\mathrm{T}^\mathrm{b} > 30$ GeV/c	MHz	0.08	1.3	8
Jets $p_\mathrm{T}^\mathrm{jet} > 50$ GeV/c	MHz	1.1	15	90
$\mathrm{W^+ + W^-}$ production	kHz	10	65	390
$\mathrm{W^+} \rightarrow l + \nu$	kHz	0.6	3.8	23
$\mathrm{W^-} \rightarrow l + \nu$	kHz	0.5	2.7	19
Z production	kHz	3	20	120
$\mathrm{Z} \rightarrow ll$	kHz	0.1	0.7	4.2
$\mathrm{t\bar{t}}$ production	kHz	0.05	1.8	11

6.3.1 Trigger architectures at FCC-hh

Developing a trigger architecture for a detector at FCC-hh is a difficult task. It is hard to predict how technology will develop in the next 20 years. A possible way to understand this is to consider how the various technologies have evolved over the years and extrapolate. Constraints on the trigger architecture can be assumed based on the projections. Looking at the trigger architectures currently used at LHC, two main choices stand out: a trigger system similar to the one used in ATLAS and CMS, or one similar to ALICE and LHCb. In the former, one or more layer of hardware triggers filter data before sending it to a HLT running on a computing cluster. In the latter, the detector is fully read out every bunch crossing and its data sent to a HLT. A purely software-based trigger enables for more flexible and powerful trigger algorithms, however it requires an infrastructure able to cope with the massive data rates coming from the detector. Data rates at ALICE and LHCb are low enough to permit this, however this is not the case for

ATLAS and CMS.

Material budget and the power consumption of the CMS tracker, for instance, strongly limit the amount of data that can be readout from the device [69]. The tracker is equipped with around 15000 links requiring a total power of 13 kW to be operated. Additional links must introduced to read out the tracker every bunch crossing. However, in order to dissipate the thermal power produced by the readout electronics, a larger cooling infrastructure has also to be introduced. The material budget added by the optical links and cooling system causes a non-acceptable degradation of the reconstruction performance, ultimately imposing a limit on the data that can be read out.

A similar limit applies to the FCC-hh detector. The detector is expected to generate around 10 Pb/s of data, if every event is fully read out. About 6.5 Pb/s are expected to come from the tracker [3, 102]. A 10 Gb/s LpGBT link requires around 1 W to be operated [69]. Therefore, a tracker equipped with ≈ 650000 optical links will dissipate around 650 kW. The material introduced by the links and the cooling system will negatively affect the performance of the FCC-hh detector, unless a major breakthrough in the technology enables greatly increasing the communication speed and reducing the number of links.

Consequently, a system based on a triggered readout of the detector was investigated. Focus was put on studying the L1T, which can be technically very challenging due to many constraints such as data rates, efficiency and available technologies. Using the CMS trigger as a reference, trigger rates and physics acceptance for a L1T of a detector at FCC-hh were investigated in order to understand the scale of the problem and of possible trigger rates that the data acquisition system may have to sustain.

6.3.2 Trigger inputs

Due to bandwidth limitations, the FCC-hh L1T is expected to receive data from a subset of detectors. Subdetectors can send trigger primitives carrying either full or reduced granularity information, depending on bandwidth limits. Input from the FCC-hh calorimeters is expected to be required. It is not yet clear if reduced granularity data will be enough to provide sufficient discrimination capabilities. Muons have always been a reliable trigger, thanks to their identification ease, therefore inputs from the muon chambers are necessary in order to provide a complete trigger menu.

An open question is whether partially reading out the tracker will be required. Benefits of including the tracker can be seen in the CMS Phase-2 L1T upgrade presented in Chapter 3: reconstructing tracks and the primary vertex is crucial in high pile-up environments. Tracks enable powerful reconstruction algorithms and pile-up rejection techniques to be run at trigger-level: particle flow [87] can be employed to reconstruct single particles in the detector with great precision; objects in the calorimeter can be identified with increased efficiency; photons and electrons can be separately identified; the longer lever arm improves the muon resolution, which is fundamental in the FCC-hh detector, as mentioned in section 6.2.3; algorithms such as PUPPI [87] can be used to remove pile-up particles and weigh the momentum of the remaining particles based on the pile-up level.

However, it was also shown that the use of tracks drastically increases trigger complexity. Introducing the tracker implies introducing a new trigger subsystem, significantly increasing the number of boards required in the L1T and requiring more manpower to commission and maintain the system. In addition, more bandwidth in output from the detector is required in order to read out data from the tracker. The number of links and power must be increased, with an impact on the material budget and cooling system of the detector, as previously mentioned.

Although experience with the ATLAS and CMS detector shows that tracks are fundamental in maintaining a good balance between physics acceptance and data rates in the trigger, it is important to investigate whether it is possible to use the calorimeter and muon system to build a L1T system with sufficient rejection capabilities. The system could be followed by the HLT to perform the final selection, or, alternatively, by a second level of triggering that reads out tracks at a reduced rate.

In the next sections an estimation of rates at FCC-hh for a L1T system with and without tracks in input will be presented to investigate both scenarios.

6.4 Estimation of trigger rates using a scaling method

Understanding whether a hardware trigger receiving a complete set of inputs from the detector can provide satisfactory performance is of fundamental importance before delving into more detailed trigger studies. An initial first estimate of trigger rates for a L1T system receiving inputs from tracker, calorimeter and muon system was computed to this purpose. The physics acceptance of this trigger system was studied by generating a number of interesting physics events, understanding the required L1T thresholds in order to accept those events, and studying the relative background trigger rates.

The method used to estimate trigger rates at FCC-hh was a simple rescaling of the CMS Phase-2 L1T rates to FCC-hh luminosity. Although simple, this method provided a rough estimates of rates in a short time span. Rates of jets, muons, electrons and $p_{\mathrm{T}}^{\mathrm{miss}}$ triggers were computed at $\sqrt{s} = 100$ TeV and $\mathscr{L}_{\mathrm{inst}} = 5 \times 10^{34}\ \mathrm{cm}^{-2}\ \mathrm{s}^{-1}$.

Trigger rates of the CMS L1T were scaled to FCC-hh under the assumption that jets affect and drive a large fraction of the trigger rates. The electron rate is dominated by misidentified jets. The muon rate is led by jets reaching the muon detectors and hadrons decaying into muons. The $p_{\mathrm{T}}^{\mathrm{miss}}$ rate is largely determined by jet momentum mismeasurements. The procedure used to run this scaling was identical for each trigger object type that was studied and can be summarised as follows:

1. For a variety of p_{T} thresholds, scaling factors $\rho(p_{\mathrm{T}})$ are computed:

   $$\rho(p_{\mathrm{T}}) = \frac{R^{\mathrm{CMS}}_{\mathrm{object}}(p_{\mathrm{T}})}{R^{\mathrm{CMS}}_{\mathrm{jet}}(p_{\mathrm{T}})} \tag{6.1}$$

   where $R^{\mathrm{CMS}}_{\mathrm{object}}(p_{\mathrm{T}})$ is the rate of a specific trigger object as a function of p_{T} , and $R^{\mathrm{CMS}}_{\mathrm{jet}}(p_{\mathrm{T}})$ is the rate of the single-jet trigger as a function of p_{T} at the same luminosity in CMS.

2. Single-jet trigger rates at FCC-hh, $R^{\mathrm{FCC}}_{\mathrm{jet}}(p_{\mathrm{T}})$, are estimated by running a simulation of the FCC-hh detector.

3. Rates of the trigger object at FCC-hh, $R^{\mathrm{FCC}}_{\mathrm{object}}(p_{\mathrm{T}})$ are obtained by multiplying the single-jet trigger rate by the scaling factors:

   $$R^{\mathrm{FCC}}_{\mathrm{object}}(p_{\mathrm{T}}) = \rho(p_{\mathrm{T}}) \cdot R^{\mathrm{FCC}}_{\mathrm{jet}}(p_{\mathrm{T}}) \tag{6.2}$$

6.4.1 Computing the scaling factors

Scaling factors were computed by dividing the jet rate by the other object rates at constant p_{T} threshold. The technical design report of the Phase-2 upgrade of the CMS L1T [31] had not been published at the time this work was done and jet trigger rates for the CMS Phase-2 L1T were not available. Consequently, the Phase-2 single-jet rate was estimated from the Phase-1 single-jet rate. Single-jet trigger rates are dominated by real jets coming from the hardest interaction in a bunch crossing. Therefore, the effect of pile-up combinatorics and detector differences between Phase-1 and Phase-2 CMS on single-jet rates are negligible and the Phase-2 rate can be obtained by scaling the Phase-1 L1T single-jet rate to $\mathscr{L}_{\mathrm{inst}} = 5 \times 10^{34}\ \mathrm{cm}^{-2}\ \mathrm{s}^{-1}$.

Figure 6.4 shows rates of various jet triggers, including single-jet, as a function of the trigger threshold at $\sqrt{s} = 13$ TeV and $\mathscr{L}_{\mathrm{inst}} = 1.15 \times 10^{34}\ \mathrm{cm}^{-2}\ \mathrm{s}^{-1}$ for Phase-1 CMS. Single-jet rates in Fig. 6.4 were scaled by the luminosity ratio to match $\mathscr{L}_{\mathrm{inst}} = 5 \times 10^{34}\ \mathrm{cm}^{-2}\ \mathrm{s}^{-1}$ at HL-LHC. Rates above 31.4 MHz, i.e. the maximum bunch crossing frequency in HL-LHC fills, were capped at 31.4 MHz.

The Phase-2 L1T rates for single-muon, single-electron, and $p_{\mathrm{T}}^{\mathrm{miss}}$ are shown in Fig. 6.5. These rates are taken from the technical proposal for the Phase-2 upgrade of the CMS detector [85], as the technical design report of the Phase-2 upgrade of the CMS L1T [31] had not been published yet at the time this work was done. The algorithms used to reconstruct Phase-2 L1T objects in the technical proposal are a simplification of the actual Phase-2 algorithms. Phase-2 muons are reconstructed by extrapolating tracks of muons in the muon chamber to the tracker. Each extrapolated muon is then matched to the closest track in the tracker. The p_{T} of the track in the tracker is assigned as the muon p_{T} . Phase-2 electrons are identified by matching tracks whose p_{T} is larger than 10 GeV to energy clusters in the electromagnetic calorimeter.

The scaling factors $\rho(p_{\mathrm{T}})$ were computed as in Eq. 6.1 and are shown in Fig. 6.6. At higher p_{T} thresholds, where no rate estimations were available, $\rho(p_{\mathrm{T}})$ was computed by fitting a linear function to $\rho(p_{\mathrm{T}})$ at lower p_{T} and extrapolating.

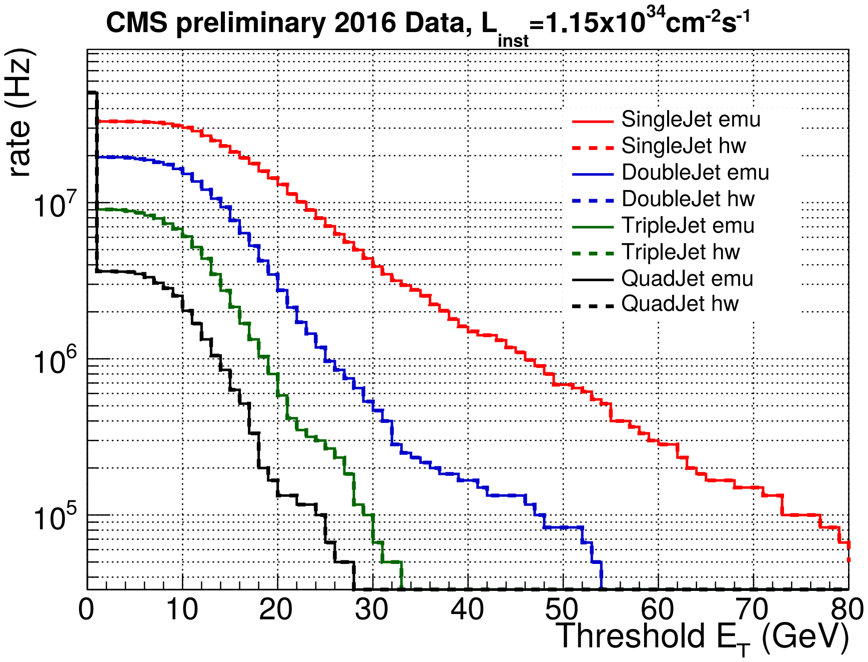

Figure 6.4: Rates for a variety of jet triggers in hardware (“hw”) and emulator (“emu”) in CMS at a centre-of-mass energy of 13 TeV and instantaneous luminosity of 1.15×10^{34} cm^{-2} s^{-1}. Taken from Ref. [103].

.

6.4.2 Generating 100 TeV events and computing the 100 TeV rates

Minimum bias events at $\sqrt{s} = 100$ TeV were generated using Pythia 8.223 [49]. The detector response to these events was simulated using Delphes [105]. Delphes is a fast simulation tool that runs a parameterised simulation of a particle detector response and its reconstruction. In a parameterised simulation the detector performance is modeled by a set of operative parameters. The Delphes simulation of the FCC-hh detector is able to: propagate tracks in a magnetic field, simulate a tracking system; compute the response of the electromagnetic and hadron calorimeters; simulate a muon identification system. The detector response simulation is then used to compute a variety of quantities, such as calorimeter deposits, and physics objects. Delphes is less accurate than simulating the full detector response using a software such as GEANT4 [92], but on the other hand it is much faster.

The single-jet trigger rate was computed using jets reconstructed by Delphes with the particle-flow algorithm [106], under the assumption that the performance of the jet reconstruction algorithm run by the trigger is not significantly different from the offline one. The jet trigger rate at a specific p_{T} threshold, $R_{\mathrm{jet}}^{\mathrm{FCC}}(p_{\mathrm{T}})$, was computed as:

$$R_{\mathrm{jet}}^{\mathrm{FCC}}(p_{\mathrm{T}}) = r(p_{\mathrm{T}}) \cdot \mathscr{L}_{\mathrm{inst}} \cdot \sigma_{\mathrm{inel}} \tag{6.3}$$

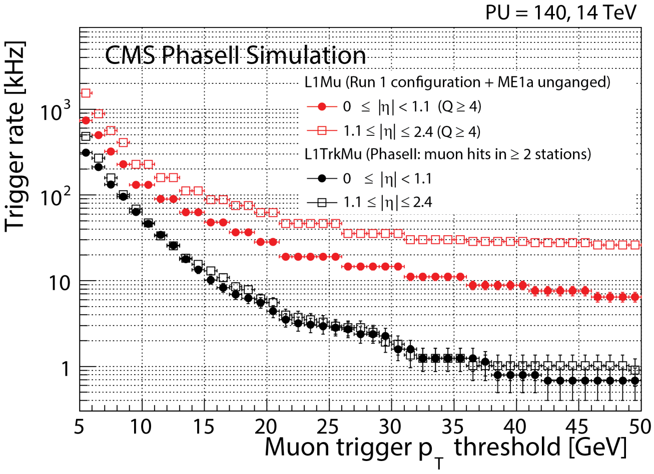

(a) Muon

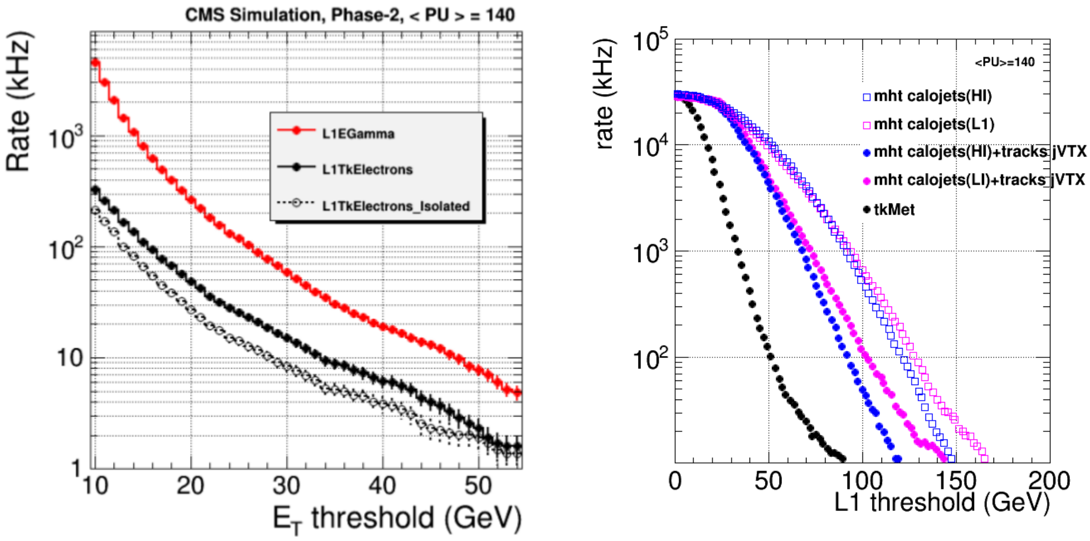

(b) Electron

(c) $p_{\mathrm{T}}^{\mathrm{miss}}$ (tkMet in the plot)

Figure 6.5: Phase-2 CMS object rates that were used as a reference for the FCC extrapolation. Muon and electron rate plots are taken from Ref. [85]. The $p_{\mathrm{T}}^{\mathrm{miss}}$ plot is taken from Ref. [104].

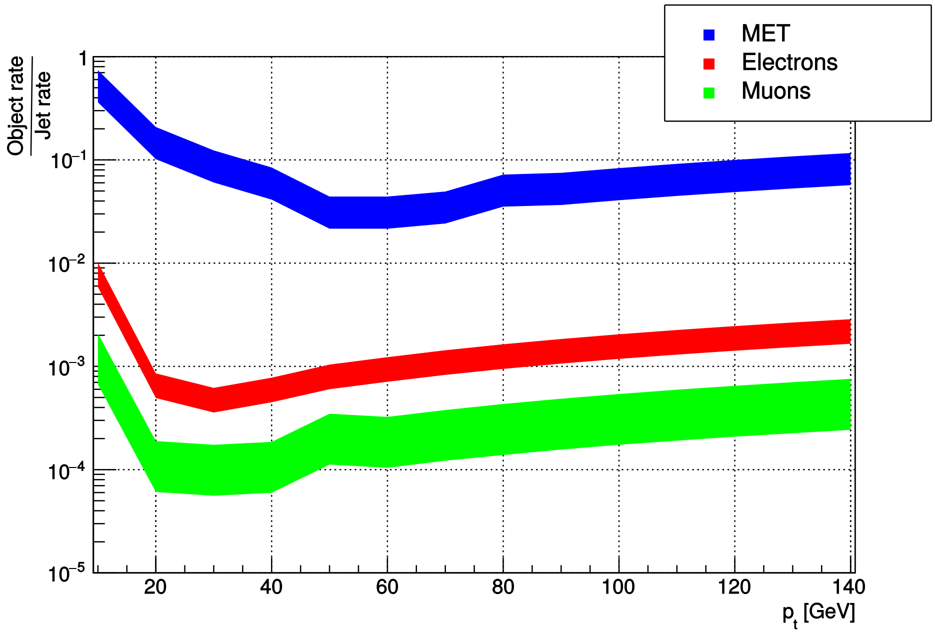

Figure 6.6: Ratios between single-jet trigger rate and single-electron (green), single-muon (red), and MET (blue) trigger rates as a function of the trigger p_{T} threshold for the CMS Phase-2 L1T at a instantaneous luminosity of 5×10^{34} cm^{-2} s^{-1} and $\sqrt{s} = 14$ TeV . The width of the band represents the uncertainty.

where $r(p_{\mathrm{T}})$ is the fraction $r(p_{\mathrm{T}})$ of minimum bias events that have at least one jet with p_{T} greater than the p_{T} threshold, $\mathscr{L}_{\mathrm{inst}}$ is the instantaneous luminosity, and σ_{inel} is the minimum bias cross section.

Rates of jet triggers at the luminosity of 5×10^{34} cm^{-2} s^{-1} are displayed in black in Fig. 6.7; rates of electron, muon, and MET triggers are respectively shown in green, red, and blue in Fig. 6.7 and were obtained by multiplying the jet rate by the scaling factors in Fig. 6.6. This method can not give predictions for triggers using p_{T} thresholds lower than 30 GeV due to saturation of the jet trigger rate. In addition, due to limited statistics, trigger rates at p_{T} thresholds greater than 140 GeV could not be estimated.

6.4.3 Generating the benchmark physics

The sensitivity of a set of benchmark physics channels as a function of the trigger p_{T} threshold and rate was investigated in order to understand the impact on physics reach of the p_{T} thresholds. More specifically, events with W, Z, and Higgs boson production in their leptonic final states at $\sqrt{s} = 100$ TeV were generated using Pythia 8.223:

- Z → ee

- $\mathrm{W} \to \mathrm{e}\nu_{\mathrm{e}}$

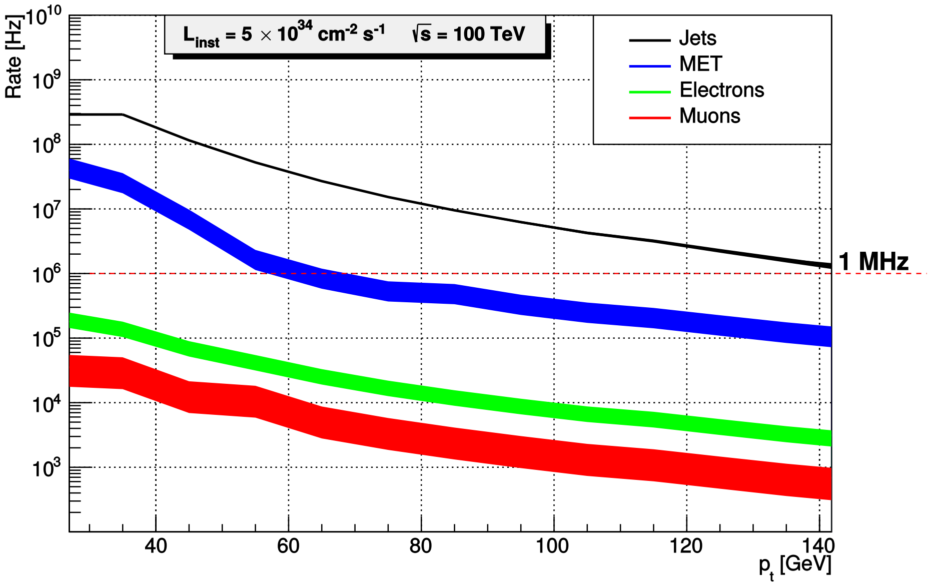

Figure 6.7: Single-jet (black), single-electron (green), single-muon (red), and MET (blue) trigger rates as a function of the trigger p_T threshold for a L1T system having similar performance to the CMS Phase-2 L1T system at an instantaneous luminosity of 5×10^{34} cm^{-2} s^{-1} and $\sqrt{s} = 100$ TeV . The width of the band represents the uncertainty. A line showing the 1 MHz threshold was added as a reference.

- $\mathrm{H} \to \mathrm{ZZ} \to \mathrm{eeee}$
- $\mathrm{H} \to \mathrm{WW} \to \mathrm{e}\nu_e \mathrm{e}\nu_e$
- $\mathrm{Z} \to \mu\mu$
- $\mathrm{W} \to \mu\nu_\mu$
- $\mathrm{H} \to \mathrm{ZZ} \to \mu\mu\mu\mu$
- $\mathrm{H} \to \mathrm{WW} \to \mu\nu_\mu\mu\nu_\mu$

Based on the decay channel, the distribution of the leading electron or muon p_T was computed for each one of them. Figure 6.8 shows the p_T distribution of the leading electron. A similar distribution was observed for the leading muon. The physics acceptance for a specific type of event at various p_T thresholds was computed by dividing the number of events whose leading object p_T was above the corresponding trigger threshold by the total number of generated events. Figure 6.9 shows the efficiency of processes listed above as a function of the electron and muon p_T thresholds. Fig. 6.10 displays the fraction of accepted events as a function of the trigger rate, which was computed by replacing the p_T thresholds of Fig. 6.9 with their corresponding rates from Fig. 6.7.

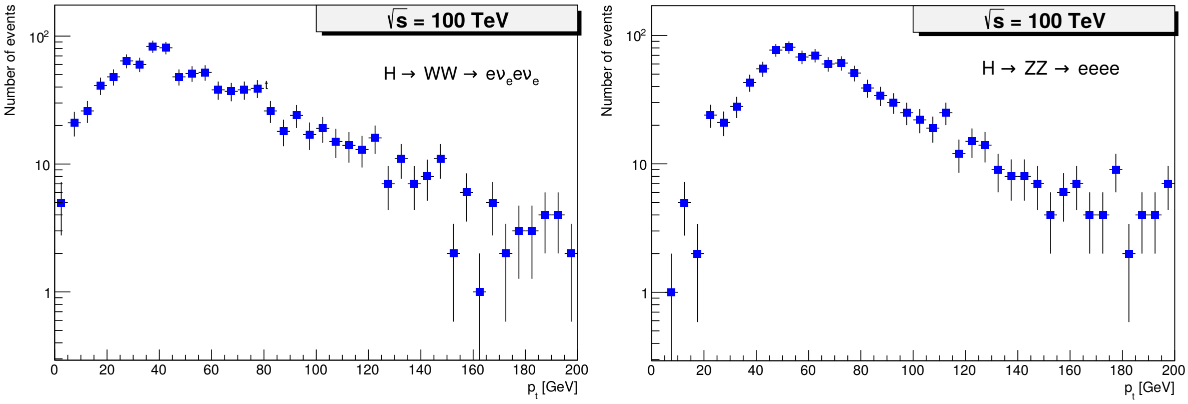

(a) $H \to WW \to e\nu_e e\nu_e$ (b) $H \to ZZ \to eeee$

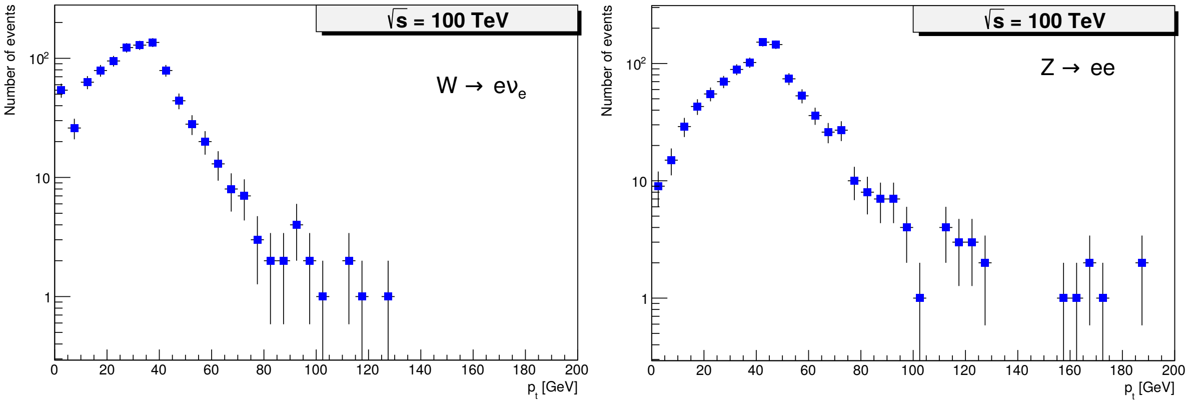

(c) $W \to e\nu_e$ (d) $Z \to ee$

Figure 6.8: p_T distribution of the leading electron in electroweak events. Distribution were obtained from 1000 events in each process type.

6.4.4 Discussion of results

Raising the centre-of-mass energy from $\sqrt{s}$ = 13 TeV to $\sqrt{s}$ = 100 TeV causes a significant increase in rates. A comparison between Figs. 6.7 and 6.4 shows that the single-jet trigger rate has increased by around 20 to 40 times depending on the threshold, thus increasing all the other object rates by the same amount. The results presented in this section can be studied under three different points of view in order to find candidate p_T thresholds.

First of all, it can be assumed that the same bandwidth allocations as in the CMS Phase-2 L1T menu will be applied to the FCC-hh L1T to determine p_T thresholds. The resulting thresholds between the two experiments can be compared. According to the trigger menu presented at page 32 of Ref. [107], candidate p_T thresholds for the CMS Phase-2 L1T are: 31 GeV for the single-electron trigger, firing with a background rate of 38 kHz; 18 GeV for single-muon trigger, with a background rate of 27 kHz; 200 GeV for the p_T^{miss} trigger, with background rate of 18 kHz. According to Fig. 6.7, thresholds at FCC-hh for the electron and muon trigger will approximately

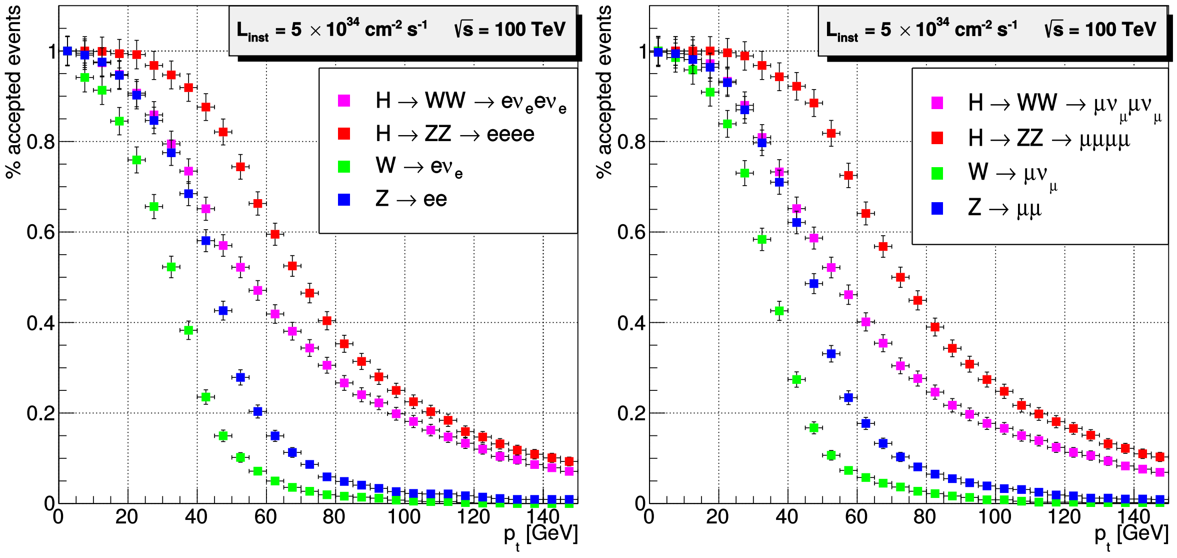

(a) Electron (b) Muon

Figure 6.9: Fraction of accepted events for a set of physics processes as a function of the p_T threshold at $\sqrt{s} = 100$ TeV and instantaneous luminosity of 5×10^{34} cm^{-2} s^{-1} .

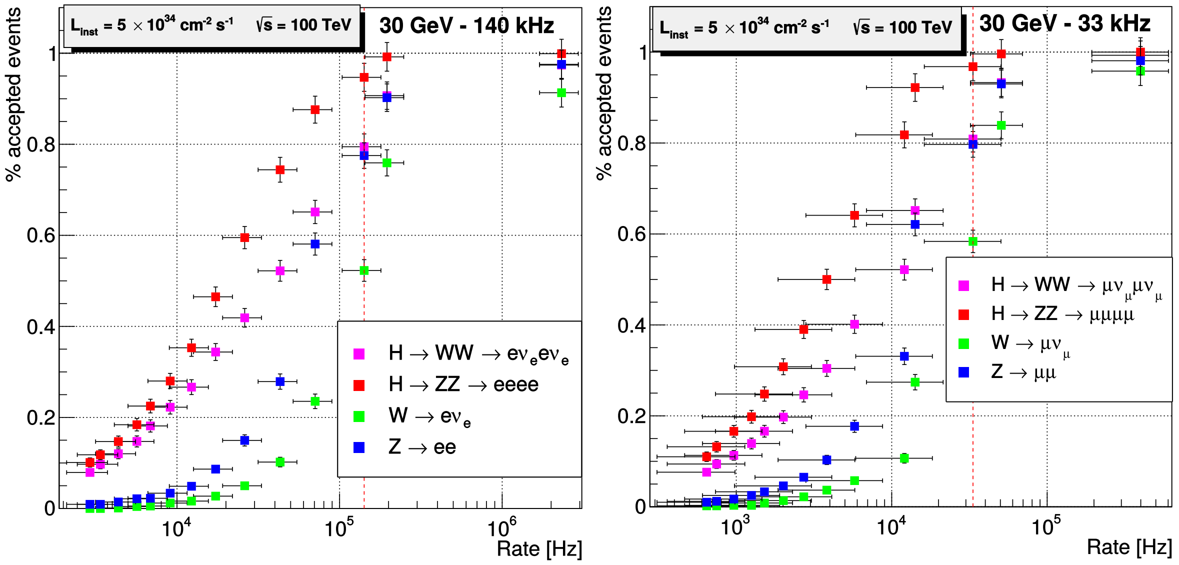

(a) Electron (b) Muon

Figure 6.10: Fraction of accepted events for a set of physics processes as a function of the trigger rate at $\sqrt{s} = 100$ TeV and $\mathscr{L}_{\text{inst}} = 5 \times 10^{34}$ cm^{-2} s^{-1} . A line showing a possible trigger threshold and the relative rate was added for reference.

have a twofold increase to 70 GeV and 40 GeV, respectively. The $p_{\mathrm{T}}^{\mathrm{miss}}$ trigger will roughly be unchanged, if the trend shown between 60 and 140 GeV is extrapolated to higher p_{T} thresholds. Secondly, potential p_{T} thresholds can be found assuming that single-object triggers will be used to select electroweak physics. Single-muon triggers can maintain sensitivity to these processes while keeping reasonable rates: a p_{T} threshold of 30 GeV can retain good physics acceptance with a rate of 33 kHz, shown in the red dotted line in Fig. 6.10(b). Jets are more often misidentified as electrons than as muons, as shown in Fig 6.6, which leads to higher rates for single electron triggers. Consequently, the same p_{T} threshold as the single-muon trigger can be achieved with a single-electron rate of 140 kHz, leading to a similar fraction of accepted events for the channels under study, as shown in Fig. 6.10(a).

Lastly, thresholds can be determined by dividing the total available rate between the various objects that were studied in this section to build a possible menu. Assuming that the level-1 trigger will have a maximum accept rate of 750 kHz, as in the CMS Phase-2 L1T, and keeping a safety margin of 50%, 375 kHz is the total available rate budget. Around 30 and 140 kHz could be respectively assigned to single muon and electron triggers in order to accept electroweak physics, while the remaining 200 kHz be equally shared between single jet and $p_{\mathrm{T}}^{\mathrm{miss}}$ triggers. The 100 kHz p_{T} threshold for jets is around 200 GeV, if the trend between the 80 GeV to 140 GeV in Fig. 6.7 is extrapolated to higher p_{T} thresholds. The $p_{\mathrm{T}}^{\mathrm{miss}}$ threshold is 140 GeV, if the remaining 100 kHz are allocated in the $p_{\mathrm{T}}^{\mathrm{miss}}$ channel, obtaining the same threshold as CMS.

This study seems to show that rates are manageable at FCC-hh at the base luminosity of 5×10^{34} cm^{-2} s^{-1} . The final luminosity of 30×10^{34} cm^{-2} s^{-1} was not considered, however scaling rates by a factor 6, i.e. the ratio between the base and ultimate luminosity, shows that single-object triggering may not be sufficient for electroweak and Higgs boson physics, while staying within the rate limits. Cross-object triggers will be crucial in rejecting background events while maintaining lower rates and good physics acceptance at high pile-up. This study uses a simple rescaling of CMS rates method to help understanding the scale of the challenge of triggering at FCC-hh. The impact of using more complex triggers is hard to study with this technique.

This work has a limited scope of prediction: it does not predict rates for p_{T} thresholds below 30 GeV, which is a very interesting range to study; it does not provide a reliable rate estimation above 140 GeV, due to the lack of data; it uses a simple scaling of rates, effective to get a first understanding of the problem, but a more solid method is required to have a more conclusive answer. In the next section, a more sophisticated method based on a simulation of the trigger will be used to predict rates in order to circumvent part of the limits of the rescaling method.

6.5 Estimation of trigger rates using a parameterised simulation

The goal of the work presented in this section is to obtain a more robust estimate of trigger rates by developing a parameterised simulation of a detector and trigger system at FCC-hh which has the same performance as CMS. More specifically, a simulation of the Phase-1, e/γ, and muon trigger was initially built; in a second stage, simulation of the Phase-2 jet trigger was also added. An e/γ is an object that is compatible in the trigger with either an electron or a photon, as, having no tracks, no discrimination between the two is possible in the Phase-1 L1T. Using a parameterisation solved some of the issues of the rescaling method, provided a better understanding of the main background physics processes and issues in triggers at hadron colliders, and returned a more reliable estimate of trigger rates.

In the next sections, two object types will be referred to: generator-level and trigger-level objects. The former are products in output from the event generator, their properties will be denoted by the superscript “gen”. The latter are objects reconstructed by the L1T; the superscript “L1T” will be use to mark their properties. The superscript “EG” will be used to refer to properties of e/γ objects.

6.5.1 Overview of the method

Using a full simulation of the FCC-hh detector response to events at $\sqrt{s}$ = 100 TeV was not possible due to computing limits, lack of detailed detector design and relative GEANT4 description. Therefore, a parameterised simulation was used, due to its greater speed and simplicity.

The set of steps listed below was followed for each trigger object type in order to build, validate, and run the simulation:

1. The main contributions to the trigger rate were understood and each one associated to a specific generator-level object in the event.

2. A set of parameters to model the contribution based on the generator-level objects identified in step 1 was defined.

3. Events with the contributing processes were generated in Pythia at $\sqrt{s}$ = 13 TeV and the CMS detector response was computed using a full GEANT4 simulation [92].

4. Trigger-level objects were cross-matched to generator-level objects from which they will result.

5. Parameters chosen in step 2 were computed based on the object pairs obtained in step 4.

6. The parameterisation was validated by running closure tests at 13 TeV.

7. Correction factors were computed to take account for any small differences between the two simulations.
8. Minimum bias events at $\sqrt{s} = 100$ TeV were generated and run in the parameterised simulation to obtain preliminary single-object trigger rates.
9. The correction factors computed in step 7 were applied to obtain the final rates.
10. Statistical and systematic rate uncertainties were estimated.

6.5.2 Parameter definition and calculation

Each rate-contributing process was modeled in the simulation by building two parameters. The first parameter is a probability ε that a trigger-level object will be produced by a generator-level object, as a function of $p_{\mathrm{T}}^{\mathrm{gen}}$. The second parameter is either a p_{T} distribution of the trigger-level objects or a p_{T} resolution, again as a function of $p_{\mathrm{T}}^{\mathrm{gen}}$.

Parameters were computed from pairs of generator and trigger-level objects that were cross-matched together in a GEANT4 simulation of the CMS experiment with $\Delta R < 0.3$.

The probability to reconstruct a trigger-level object ε was computed in $p_{\mathrm{T}}^{\mathrm{gen}}$ bins and was defined as:

$$\varepsilon = \frac{N_{\mathrm{matched}}^{\mathrm{gen}}}{N_{\mathrm{tot}}^{\mathrm{gen}}} \tag{6.4}$$

where $N_{\mathrm{matched}}^{\mathrm{gen}}$ is the number of matched generator-level objects in the bin, and $N_{\mathrm{tot}}^{\mathrm{jet,\,gen}}$ is the total number of generator-level objects, both matched and unmatched, in the same bin.

Momentum resolutions were obtained by grouping object pairs in $p_{\mathrm{T}}^{\mathrm{gen}}$ bins, and computing the distribution of $p_{\mathrm{T}}^{\mathrm{L1T}} - p_{\mathrm{T}}^{\mathrm{gen}}$ in each bin. Alternatively, $p_{\mathrm{T}}^{\mathrm{L1T}}$ distributions were obtained by grouping pairs in $p_{\mathrm{T}}^{\mathrm{gen}}$ bins, and then computing the distribution of $p_{\mathrm{T}}^{\mathrm{L1T}}$ in each bin.

The parameters were obtained from CMS Monte Carlo samples that were produced in the context of the Phase-2 detector studies and only included a response of the Phase-2 calorimeter. The CMS Phase-2 calorimeter is the same as the Phase-1 only in the barrel section, i.e. up to $|\eta| < 1.44$, as the Phase-1 endcap is replaced by HGCAL in the Phase-2 upgrade. Therefore, emulation of the Phase-1 L1T calorimeter trigger was only available in the barrel. Parameters computed from Phase-1 calorimeter trigger objects were only obtained on the barrel data due to this limitation, and later extended to the whole detector η coverage in the FCC-hh simulation.

In the next sections details on the backgrounds and parameterisation of each trigger object type will be presented.

6.5.2.1 Phase-1 jet trigger parameterisation

Genuine hadron jets produced in non-elastic QCD interactions reconstructed by the L1T system were considered to be the main contribution to the jet trigger rate. The jet reconstruction performance of the CMS Phase-1 L1T was parameterised by computing the jet identification probability and p_{T} resolution. Details on the algorithm used to reconstruct jets in the Phase-1 L1T are given in Section 4.2 and in Ref. [93].

Generator-level jets were cross-matched to trigger-level ones in a CMS detector response simulation to QCD events containing at least one jet with p_{T} ranging from 15 GeV to 7000 GeV at $\langle \mathrm{PU} \rangle = 140$.

However, only pairs including leading generator-level jets in an event were selected for parameter calculation, as sub-leading jets typically have worse reconstruction performance. In addition, jet pairs whose $p_{\mathrm{T}}^{\mathrm{jet,\,gen}} < 25$ GeV were excluded since low-momentum jets are hard to model due to high pile-up contribution and do not affect rates in the p_{T} thresholds of interest. A distribution of the distance ΔR for two different $p_{\mathrm{T}}^{\mathrm{jet,\,gen}}$ bins is shown in Fig. 6.11.

Figure 6.12(a) shows the jet identification probability $\varepsilon_{\mathrm{jet}}$ obtained using Eq. 6.4. Two jet p_{T} resolutions in two different $p_{\mathrm{T}}^{\mathrm{jet,\,gen}}$ bins are shown in Fig. 6.12(b). An offset to the jet p_{T} resolution can be observed. The source of the shift was ascribed to pile-up, which was too high for the pile-up correction techniques used in the Phase-1 trigger to compensate.

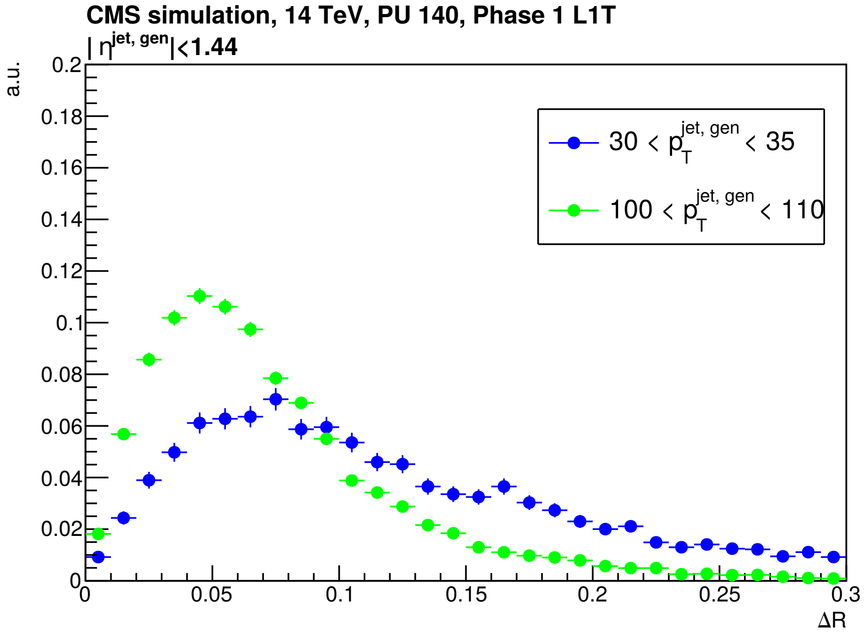

Figure 6.11: Distribution of the distance ΔR between the matched jets in two $p_{\mathrm{T}}^{\mathrm{jet,\,gen}}$ bins. Distributions are normalised to unit area.

6.5.2.2 Histogrammed jet trigger parameterisation

The development and performance of a new jet trigger algorithm, called the histogrammed jet algorithm, for the Phase-2 upgrade of the level-1 trigger of the CMS experiment was presented in Chapter 4. An estimation of the single-jet trigger rate using the histogrammed jet algorithm at

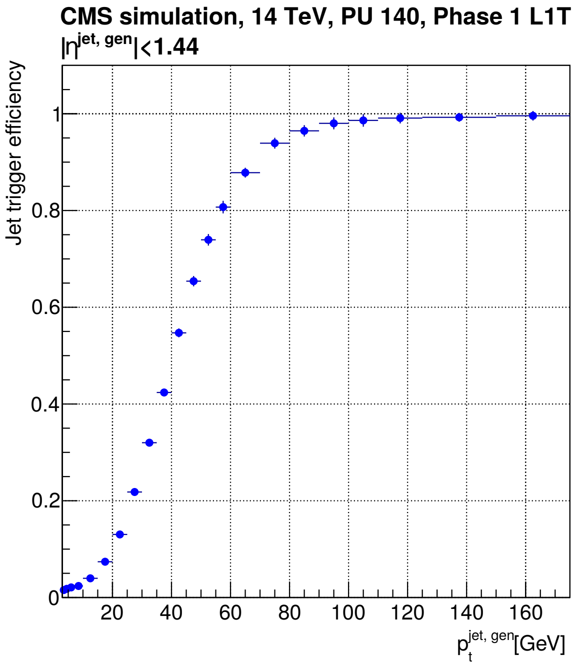

(a) Identification efficiency

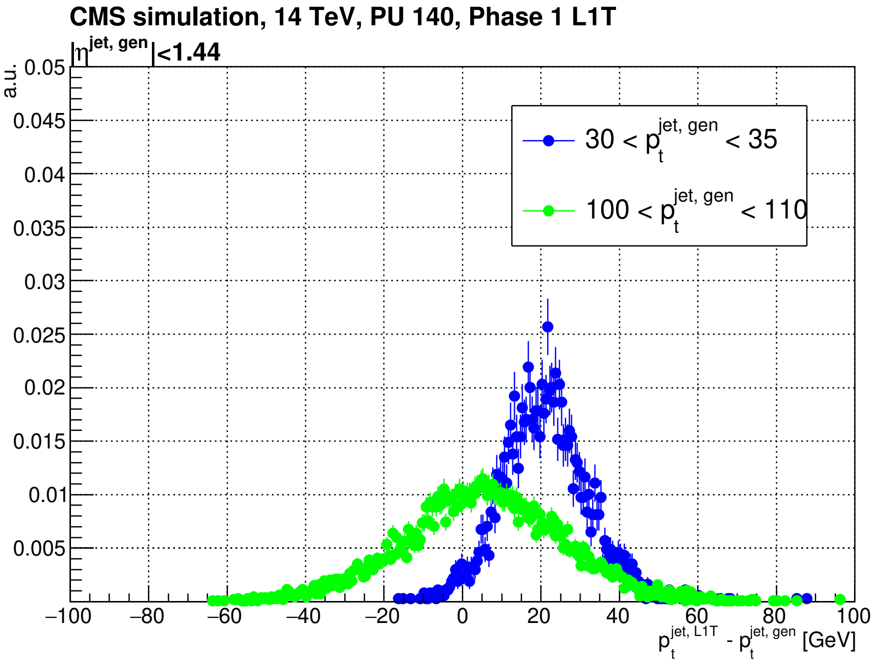

(b) p_T resolution

Figure 6.12: Jet trigger identification efficiency and resolution parameterisation obtained from the parameter calculation procedure. Distributions are normalised to unit area.

FCC-hh was computed to understand the impact of the improved response from use of tracking in the L1T on rates.

Parameters for the simulation were obtained in the same fashion to the Phase-1 jet trigger. The momentum resolution and identification probability were obtained by cross-matching histogrammed jets to generator-level ones in a sample containing QCD events containing at least a jet with p_T ranging from 15 to 7000 GeV at $\langle \mathrm{PU} \rangle \approx 200$. Pairs with $p_\mathrm{T}^\text{jet, gen} < 50$ GeV were excluded; an higher exclusion threshold compared to Phase-1 jets was chosen in order to compensate for the increased pile-up background. The jet trigger p_T resolution and identification probability are shown in Fig. 6.13. Figure 6.14 shows that the histogrammed jet algorithm has higher identification probability than the Phase-1 algorithm. The resolution curves in Fig. 6.13(b) are centred on zero as the algorithm has jet energy correction factors that compensate for pile-up contributions.

6.5.2.3 EGamma trigger parameterisation

Hadrons mistakenly identified as e/γ objects by the L1T system were considered to be the main contribution to the e/γ trigger rate. Generator-level jets were considered in modeling this process, as a proxy for their components. The probability for a hadron jet to produce a fake e/γ and its momentum distribution as a function of $p_\mathrm{T}^\text{jet, gen}$ were obtained. Generator-level jets were cross-matched to e/γ in the same QCD sample used for the Phase-1 jet parameterisation. The same selections described in Section 6.5.2.1 were applied in the matching stage, with the only difference that pairs whose $p_\mathrm{T}^\text{jet, gen} > 3$ GeV were considered. Differently from the jet case, low-pt jets have a non-negligible probability to be reconstructed as e/γ in the $p_\mathrm{T}^\text{EG, L1T}$ range of interest, therefore they had to be included in the parameterisation.

Figure 6.15(a) shows the ε_EG used in the simulation. The plot shows a feature around 128 GeV that require an understanding of the CMS e/γ trigger to be explained. e/γ are identified in the CMS level-1 trigger by looking for specific energy deposit patterns in the calorimeter. Thresholds on the H/E ratio, i.e. the ratio between the energy that is deposited in the hadron and electromagnetic calorimeter in the pattern, are used to distinguish e/γ from jets for energies below 128 GeV, where the jet rate is high. The identification criterion is relaxed above this energy threshold, as the jet contribution becomes negligible, causing every valid pattern that is found by the e/γ trigger algorithm to be identified as e/γ regardless of its H/E ratio. In conclusion, the probability shown in Fig. 6.15(a) is led by the H/E selection criterion for $p_\mathrm{T}^\text{jet, gen} < 128$ GeV; a larger fraction of the jets forms clusters whose energy is greater than 128 GeV as the the jet p_T increases, which leads to the rise in the probability above this $p_\mathrm{T}^\text{jet, gen}$ value.

$p_\mathrm{T}^\text{EG, L1T}$ distributions were obtained by grouping pairs in the same $p_\mathrm{T}^\text{jet, gen}$ bins, and then computing the distribution of $p_\mathrm{T}^\text{EG, L1T}$ in each bin. Smaller $p_\mathrm{T}^\text{jet, gen}$ bins than the ones used in the jet trigger work were required, which led to lower statistics in each bin, larger statistical fluctuations in the $p_\mathrm{T}^\text{EG, L1T}$ distributions, and artifacts in the trigger rates resulting from the

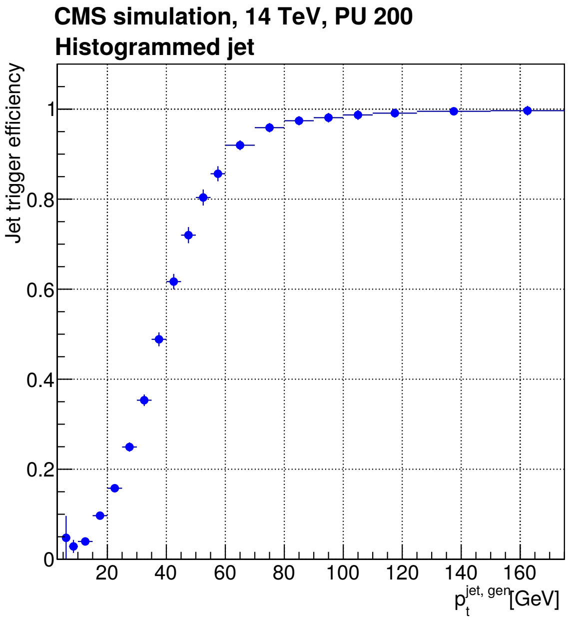

(a) Identification probability

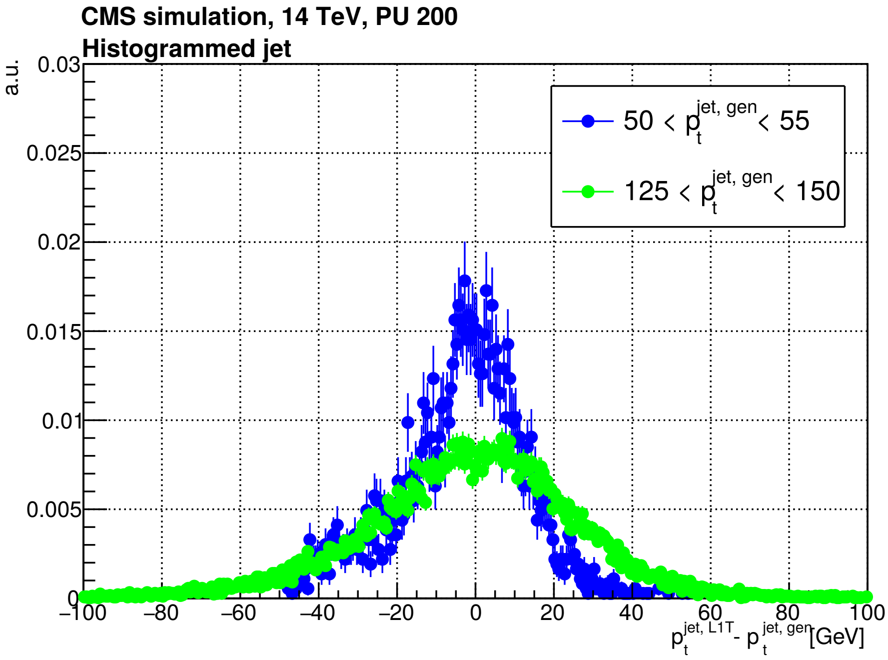

(b) p_T resolution

Figure 6.13: Identification efficiency and resolution parameterisation of the histogrammed jet trigger. Distributions are normalised to unit area.

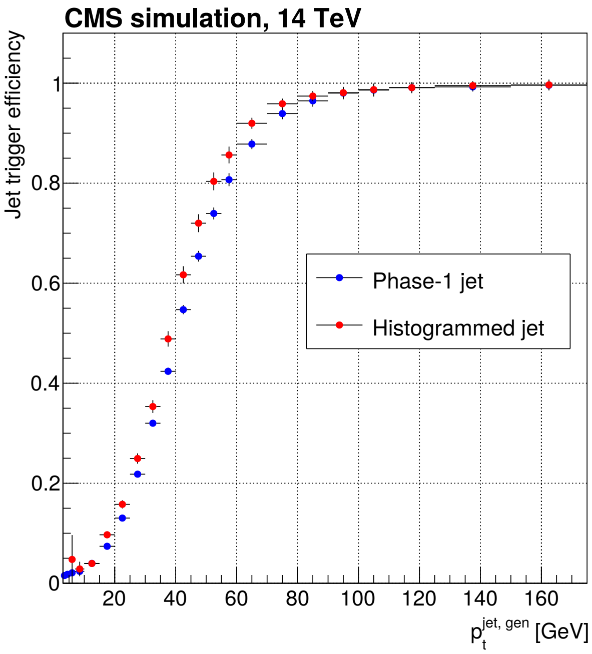

Figure 6.14: Comparison between the phase-1 and the histogrammed jet trigger identification probability.

parameterisation. To reduce fluctuations, a data smoothing procedure was applied to the $p_T^{\text{EG, L1T}}$ distributions. The smoothing method implemented in the data analysis framework ROOT [108], based on the technique described in Ref. [109], was used. Two distributions in two different $p_T^{\text{jet, gen}}$ bins are shown in Fig. 6.15(b).

6.5.2.4 Muon trigger parameterisation

Three processes were identified as main contributions to the muon trigger rates:

- muons produced in electroweak processes and decays of short-lived, heavy quark flavours, this phenomenon will be referred to as “prompt muons”;
- muon produced in in-flight decays of long-lived hadronic states, i.e. pions and kaons, which will be referred to as “decay-in-flight muons”;
- hadron jets punching-through the detector that reach the muon chambers, which will be referred to as “punch-through muons”.

Although both processes generate actual muons reaching the muon chambers, prompt and decay-in-flight muon contributions were treated separately, as the generator-level information in the CMS samples did not include muons coming from decays of pions and kaons. Two different sets of parameters were produced, one describing the prompt muons, and one describing the

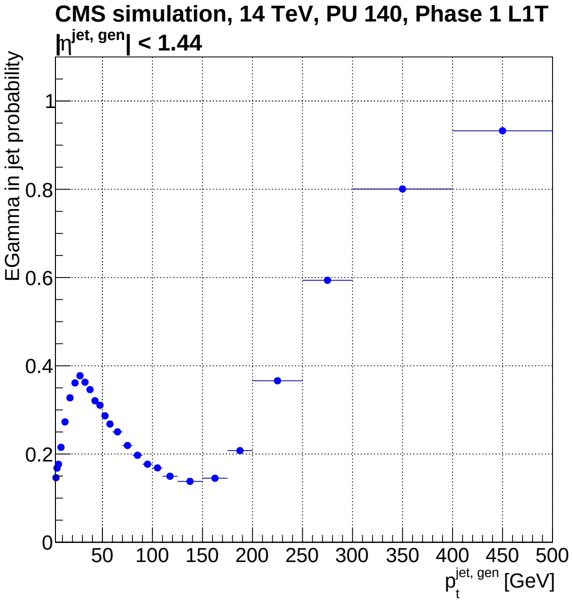

(a) Jet misidentification probability

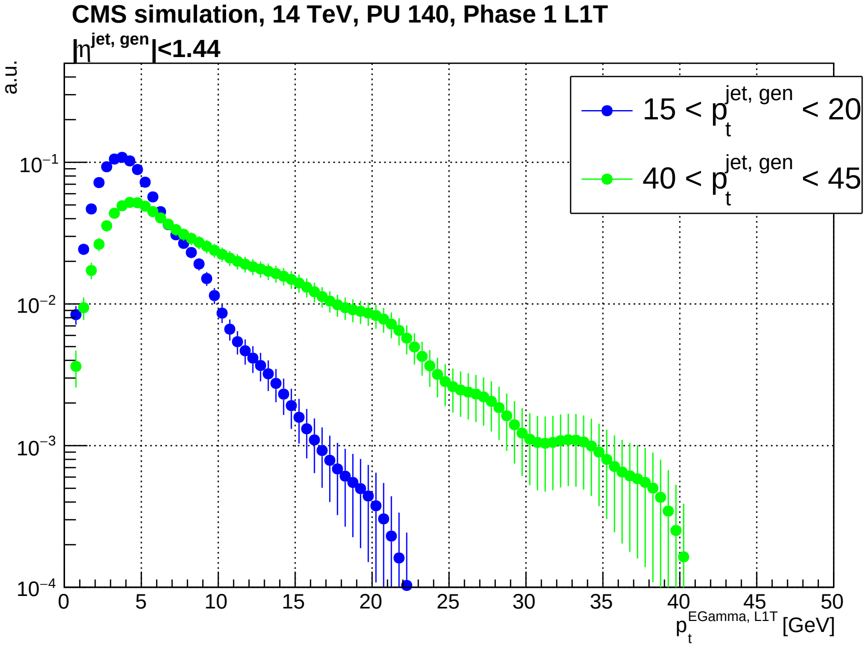

(b) e/γ p_{T} distribution

Figure 6.15: Jet misidentification probability and e/γ p_{T} distribution parameterisation obtained from the parameter calculation procedure.

decay-in-flight and punch-through muons at the same time. The prompt muon component was implemented in the simulation by computing the muon identification probability and p_{T} resolution of the L1T. Generator-level muons were cross-matched to trigger-level muons in a sample containing the CMS detector response to muons with p_{T} between 0 and 100 GeV in absence of pile-up, as the response of the muon chambers to muons does not depend on the pile-up level in first approximation. A larger matching radius than in the jet case, ΔR= 0.9, was used in order to take into account for the bending of the muon tracks in the ϕ direction due to magnetic field in the detector. Figure 6.16(a) shows that the average ΔR is higher for generator-level muons at low p_{T} . An additional constraint on the pseudorapidity difference $\Delta\eta$ was made by requiring $|\eta^{\mu,\,\mathrm{L1T}} - \eta^{\mu,\,\mathrm{gen}}| < 0.3$, to improve the quality of the match as η is generally not affected by the magnetic field. $\Delta\eta$ distributions are displayed in Fig. 6.16(b). It will be later shown that muons

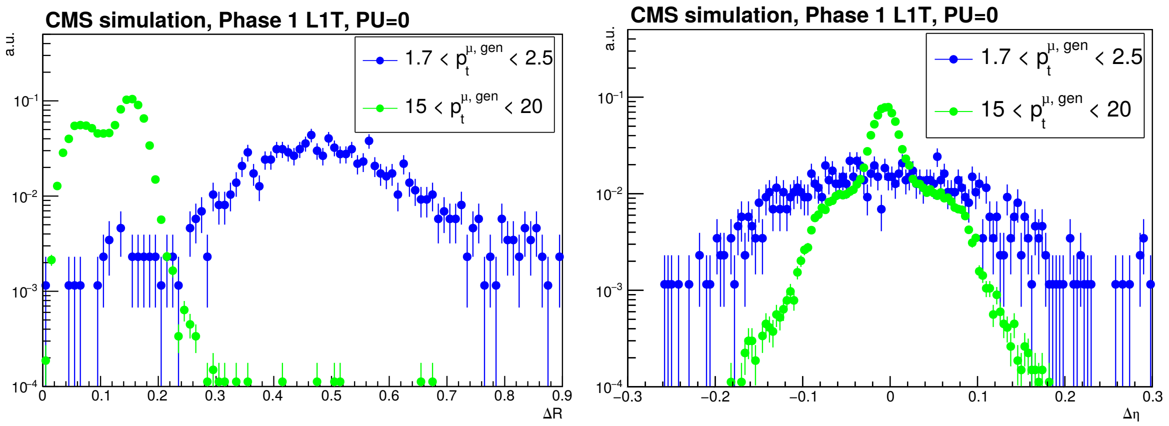

(a) ΔR

(b) $\Delta\eta$

Figure 6.16: Distribution of the quantities used in the muon matching. Data is normalised to the area.

with $p_{\mathrm{T}} < 2.5$ GeV can not be detected by the CMS muon detectors in the barrel, therefore the blue data series in Fig. 6.16 includes muons only reaching endcap muon detectors, while the green series includes contributions from both detector regions. A flatter distribution in $\Delta\eta$ can be observed in the endcap region of the detector, which is explained by the non-uniform magnetic field in the region which bends tracks in the η direction as well.

The muon identification probability was computed separately in the barrel and endcap detectors, in order to better take account for the differences in performance. A two-dimensional binning in $\eta^{\mu,\,\mathrm{gen}}$ -$p_{\mathrm{T}}^{\mu,\,\mathrm{gen}}$ was applied to muon pairs to compute ε_μ using the formula in Eq. 6.4. Muon pairs with $|\eta^{\mu,\,\mathrm{gen}}| < 1.1$ were assigned to the barrel bin, while those with $1.1 < |\eta^{\mu,\,\mathrm{gen}}| < 2.44$ were assigned to the endcap bin.

Figure 6.17 shows the identification probability in barrel and endcap. The identification probability does not increase for $p_{\mathrm{T}}^{\mu,\,\mathrm{gen}}$ up to around 2.5 and 1 GeV in the barrel and endcap, respectively. This feature is explained by the geometry of the CMS muon chambers. Barrel muon detectors are located at a distance of around 4 metres from the interaction point, while the endcap ones at a distance of a metre. At very low p_{T} , the diameter of the circular trajectory of the muons in the CMS detector magnetic field is less than the distance of the detectors from the beam pipe. Therefore, muons in this condition do not reach the detectors and can not be identified.

The muon trigger p_{T} resolution was computed by dividing pairs only in $p_{\mathrm{T}}^{\mu,\,\mathrm{gen}}$ bins, merging barrel and endcap bins for simplicity. Figure 6.18 shows the p_{T} resolution in two $p_{\mathrm{T}}^{\mu,\,\mathrm{gen}}$ bins. Muon p_{T} resolutions have long non-Gaussian tails, showing that the p_{T} of muons can be largely overestimated, due to muons scattering at a large angle in the muon chambers. Therefore, low-p_{T} generator-level muons can have a significant impact on much higher p_{T} thresholds, and can not be excluded in the simulation.

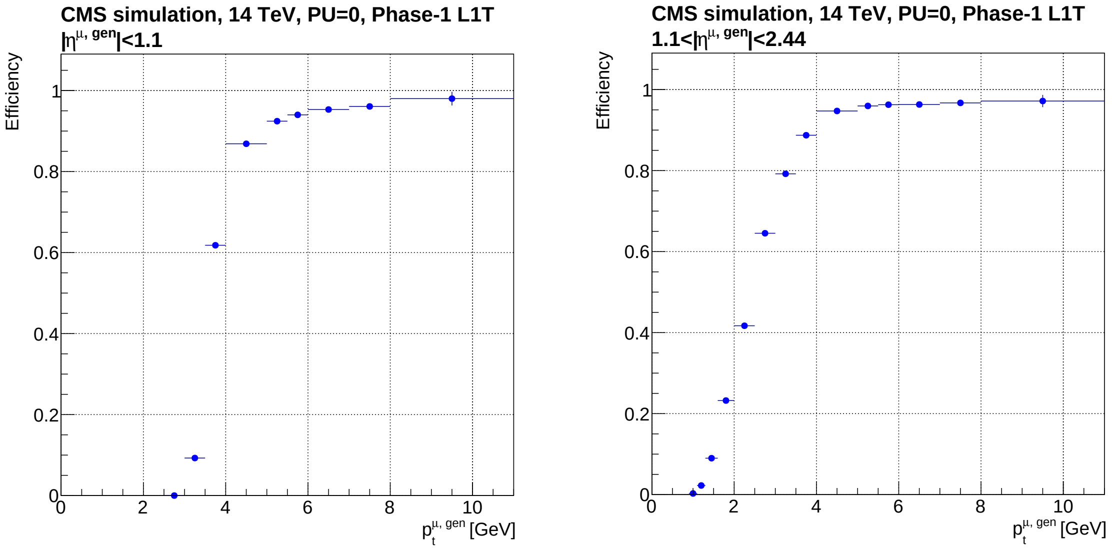

(a) Barrel

(b) Endcap

Figure 6.17: Prompt muon identification probabilities in barrel and endcap.

Decay-in-flight and punch-through muon backgrounds were modeled using a common set of parameters. The decay-in-flight muons are associated to the production and decay of pions and kaons, punch-through muons to hadron jet reaching the muon chambers. Pions and kaons are typically contained in hadron jets, therefore the parameters that describe both muon backgrounds were built by pairing trigger-level muons with generator-level jets. QCD events containing at least a jet with p_{T} ranging from 15 to 7000 GeV at $\langle \mathrm{PU} \rangle = 0$ were studied. A veto on generator-level muons was applied to exclude events containing prompt muons. Initially, a parameterisation strategy similar to that for e/γ objects was attempted by computing a parameter describing the probability for a generator-level jet to cause a trigger-level muon, and another describing the relative $p_{\mathrm{T}}^{\mu,\,\mathrm{L1T}}$ distribution. Punch-through muons are typically reconstructed close to the generator-level jet causing them. However, decay-in-flight muons can be found at large distance from the jet, as muons coming from pion and kaon decays can be produced with a very large angle. Therefore,

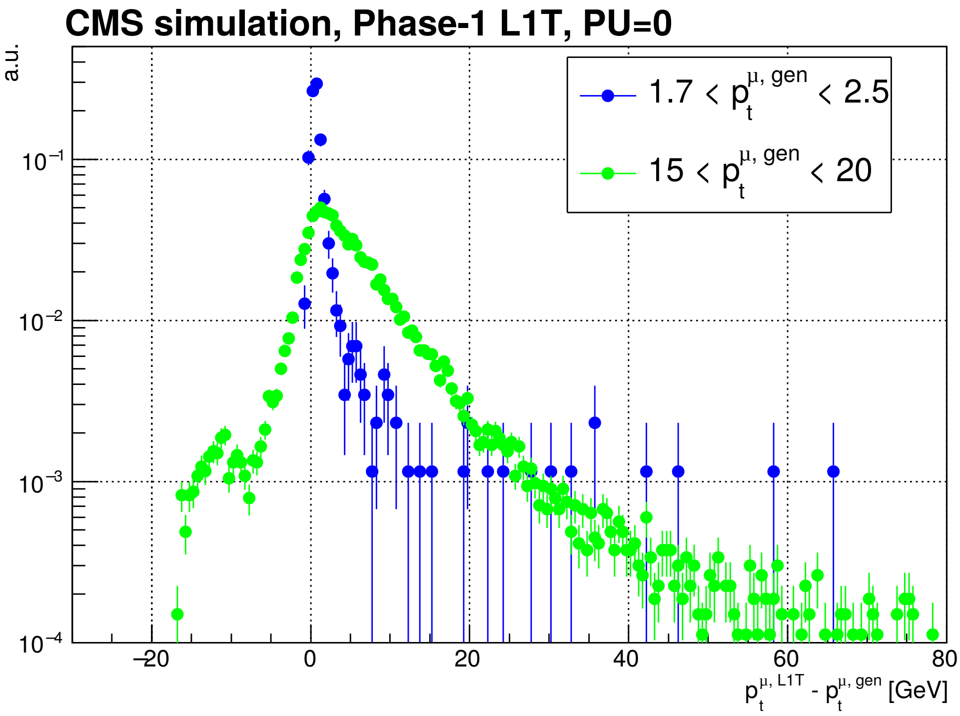

Figure 6.18: Muon trigger p_T resolution.

understanding from which jet the muon was produced using distance criteria was not possible without any additional generator-level information. A variety of alternative methods were investigated to build a parameterisation. Ultimately, two parameters based on event properties, rather than object, were built: the probability to have a non-prompt trigger-level muon in an event, and its momentum distribution. Both parameters were computed as a function of the p_T of the leading generator-level jet in the event, which was used as a proxy for the topology and energy scale of the interaction. Pairs with the leading trigger-level muon and leading generator-level jet in an event, regardless of their distance in η-ϕ space, were obtained and used to compute the parameterisation. Figure 6.19(a) shows the probability $\varepsilon_{\mu,\text{ non-prompt}}$ to have a non-prompt muon as a function of the momentum of the leading generator-level jet. Two muon momentum distributions in two different p_T bins are shown in Fig. 6.19(b).

6.5.3 Applying the parameterisation

Trigger-level objects were computed through a two-step procedure. In the first step, for each generator-level object that can contribute to a trigger rate, an accept-reject algorithm was run to determine whether the corresponding trigger-level object was produced. In the second step, the p_T of trigger-level object was computed. A number distributed as either the p_T resolution or the momentum distribution was generated using the numerical inverse transform method implemented in the ROOT [108] data analysis tool, to obtain the momentum of the trigger-level

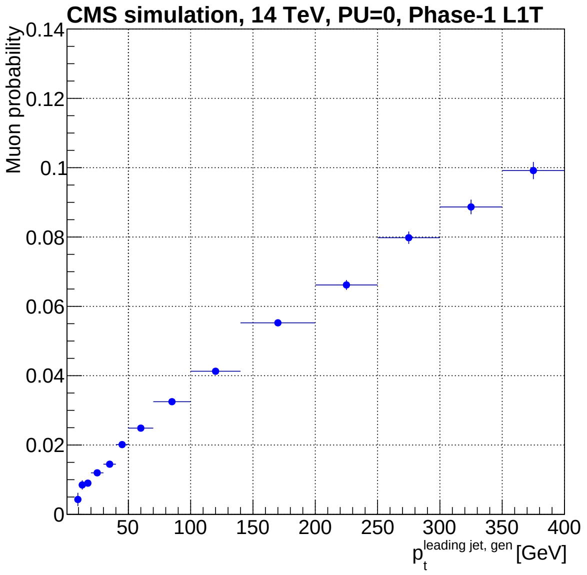

(a) Muon probability

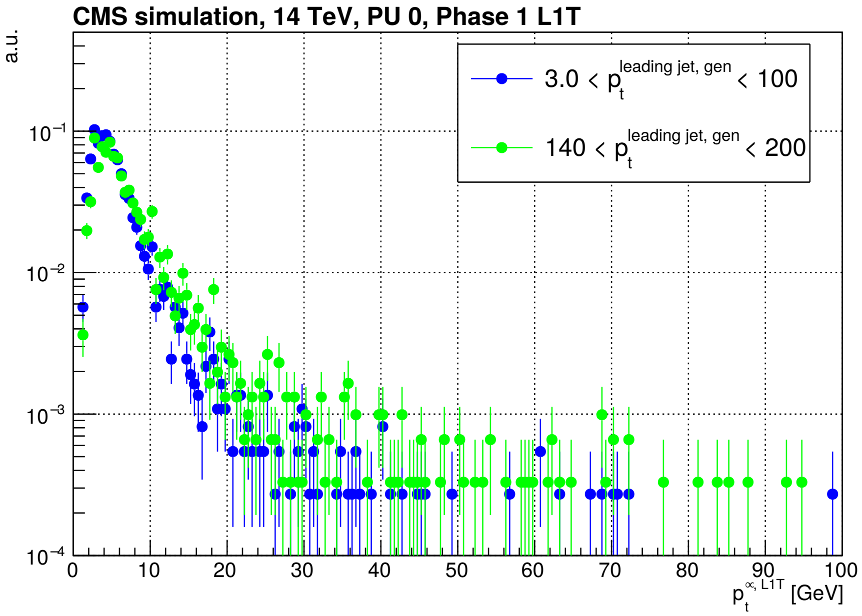

(b) Muon p_{T} distribution

Figure 6.19: Non-prompt muon probability and momentum distribution.

object. If the number was obtained from a p_{T} resolution curve, then it was added to $p_{\mathrm{T}}^{\mathrm{gen}}$, before assigning it as $p_{\mathrm{T}}^{\mathrm{L1T}}$.

Two different closure tests on the momentum distributions of the objects in output from the simulation were run to verify the quality of the parameterisation. The first was used to validate the momentum assignment and the relative parameter in the simulation. The momentum parameter was applied to matched generator-level objects. The resulting $p_{\mathrm{T}}^{\mathrm{L1T}}$ distribution was compared to the p_{T} distribution of the matched CMS trigger-level objects. The second was run to validate both the probability and momentum parameters of the simulation at the same time. Every generator-level object in the CMS simulation was used as input to the parameterised simulation. As in the first test, the resulting p_{T} distribution was compared to that of the matched trigger-level objects.

6.5.3.1 Phase-1 jets

Figure 6.20 shows the results of the closure tests: good agreement was obtained between the two distributions in both tests, thus validating the parameters and confirming that the simulation correctly applies them. The simulation seems to accurately reproduce the $p_{\mathrm{T}}^{\mathrm{jet,\,L1T}}$ distribution in the CMS simulation within a 10% difference up to 300 GeV. Above 300 GeV, the distributions have a 20% difference.

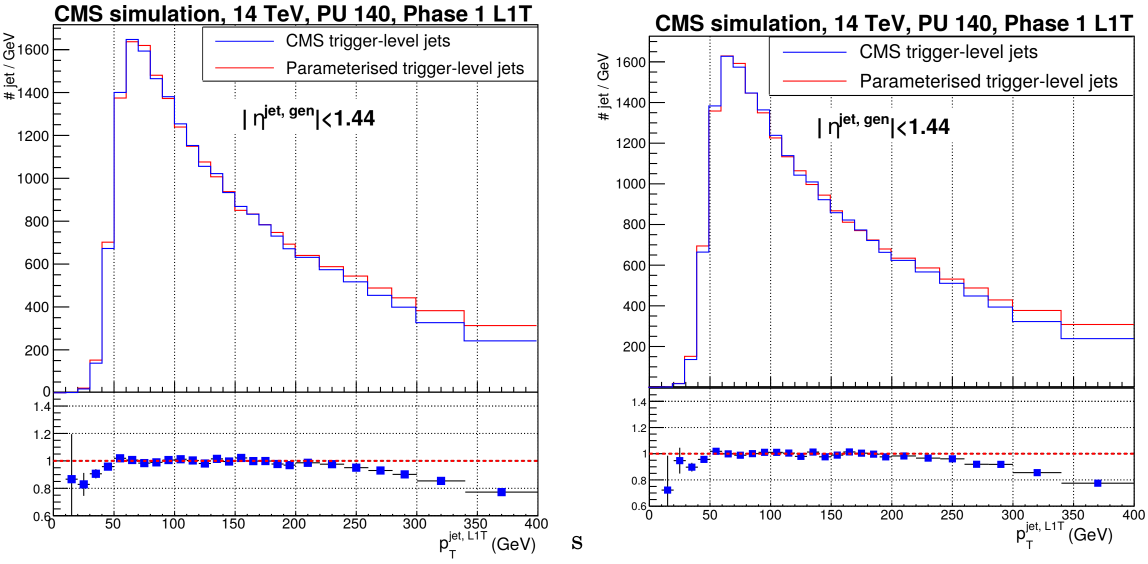

(a) Smearing

(b) Efficiency and smearing

Figure 6.20: Jet trigger parameterisation closure tests. Good agreement between the original CMS simulation and the parameterised trigger-level jets was obtained.

6.5.3.2 EGamma

Figure 6.21 shows good agreement between the $p_{\mathrm{T}}^{\mathrm{EG,\,L1T}}$ distribution in the two simulations for p_{T} up to 100 GeV. Differences arise above this value due to the smoothing technique that was applied. This is demonstrated by Fig. 6.22, which shows a comparison of the same CMS distribution with one obtained using non-smoothed $p_{\mathrm{T}}^{\mathrm{EG,\,L1T}}$ distributions. The $p_{\mathrm{T}}^{\mathrm{EG,\,L1T}}$ distributions exhibit two interesting features of the algorithm: the relaxation of the identification criterion and the energy saturation threshold. The former is explained in Section 6.5.2.3 and appears as a sudden increase in the number of e/γ objects around 128 GeV. The latter is due to the maximum p_{T} that e/γ objects can have in the CMS L1T, which is 255 GeV. The p_{T} of e/γ is stored in a 8-bit integer, where 1 unit corresponds to 1 GeV. Any e/γ with energy higher than 255 GeV is capped at that value, hence the sharp peak. In conclusion, the closure tests show that the parameterisation accurately represents the jet misidentification process up to 128 GeV. The e/γ p_{T} distribution above that value strongly depends on the features of the identification algorithm, and is not accurately represented by parameterisation due to the smoothing. Therefore, the parameterised simulation is not expected to reproduce the same e/γ background and rates as the CMS trigger for p_{T} thresholds above 128 GeV.

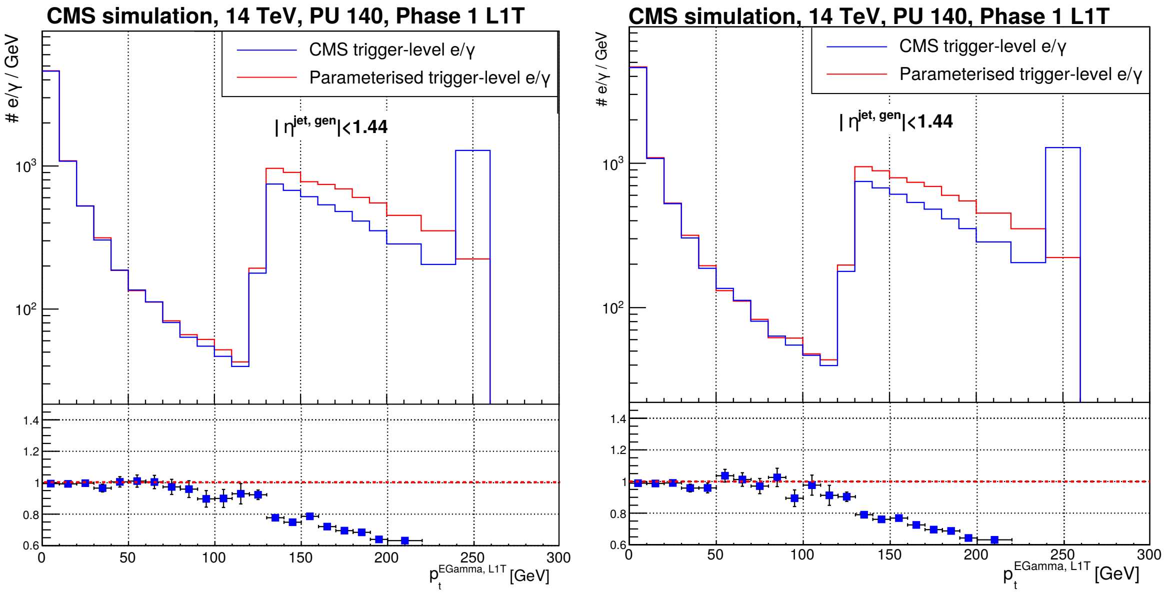

(a) $p_{\mathrm{T}}^{\mathrm{EG,\,L1T}}$ generation (b) Jet misidentification and $p_{\mathrm{T}}^{\mathrm{EG,\,L1T}}$ generation

Figure 6.21: e/γ trigger parameterisation closure tests. Discontinuities in the CMS $p_{\mathrm{T}}^{\mathrm{EG,\,L1T}}$ distributions are due to the relaxation of the identification criterion, and energy saturation threshold. Disagreements above 120 GeV between distributions in the plots are observed and caused by the smoothing that was applied to the $p_{\mathrm{T}}^{\mathrm{EG,\,L1T}}$ distribution parameterisation.

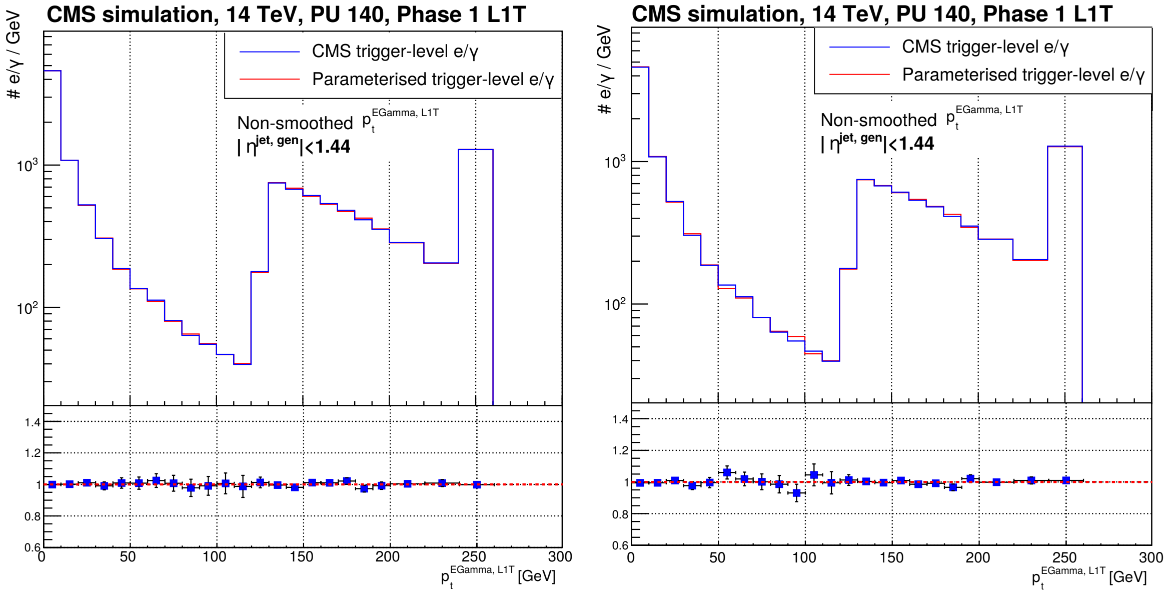

(a) $p_T^{\text{EG, L1T}}$ generation

(b) Jet misidentification and $p_T^{\text{EG, L1T}}$ generation

Figure 6.22: e/γ trigger parameterisation closure tests using $p_T^{\text{EG, L1T}}$ distribution with no smoothing. Discontinuities in the CMS $p_T^{\text{EG, L1T}}$ distributions are due to the relaxation of the identification criterion, and energy saturation threshold. Good agreement between distributions in the plots is observed demonstrating that the differences between distributions shown in Fig. 6.21 are caused by the smoothing of the $p_T^{\text{EG, L1T}}$ distribution parameterisation.

6.5.3.3 Muons

Figures 6.23 and 6.24 show closure tests for the two muon trigger backgrounds. Good agreement between the $p_T^{\mu, \text{L1T}}$ distributions from CMS full and parameterised simulations was observed.

6.5.4 Generating and validating events for the rate closure test

A comparison between the single-object rates in output from the CMS full simulation and parameterisation was obtained, as a final closure test. Rates were obtained from a sample of a CMS GEANT4 simulation that contained events at pile-up 140 and 200. A new sample with similar object distributions was produced using Pythia 8.223 and used as input to the parameterised simulation, instead of running on the same events. By confirming that a valid sample at $\sqrt{s}$ = 13 TeV was generated, knowledge of how to produce the same sample type at $\sqrt{s}$ = 100 TeV was obtained. The newly-generated $\sqrt{s}$ = 13 TeV data sample was validated by comparing the distributions of p_T , η, and multiplicity, i.e. the number of objects per event, of generator-level jets and muons to those in the CMS full simulation. Figures 6.25 and 6.26 show good agreement between the distributions from the CMS event generator and the parameterised simulation. Only a small disagreement on the number of events with more than four muons

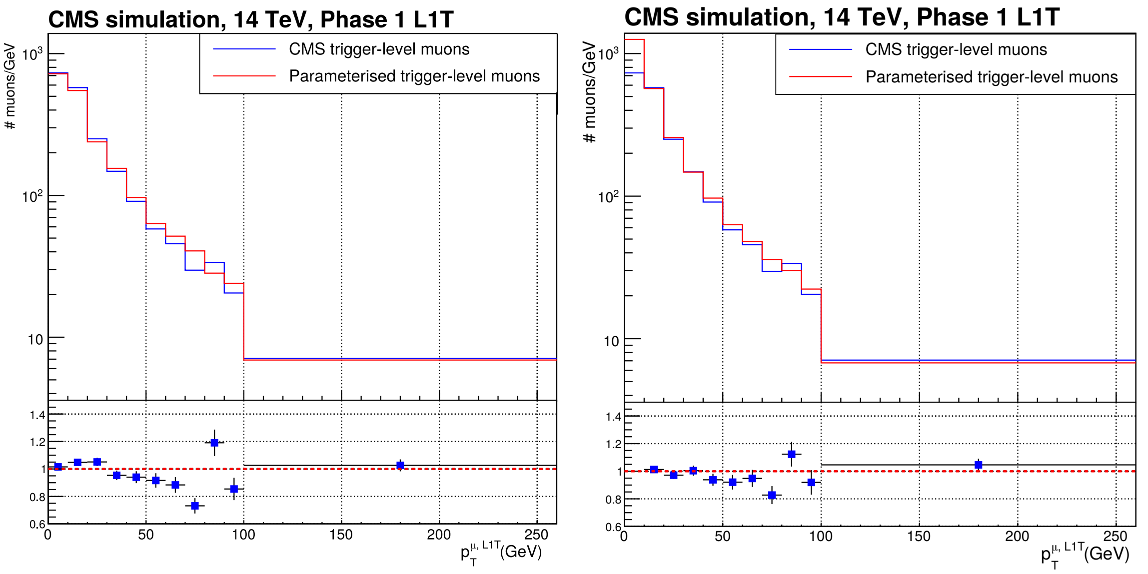

(a) $p_{\mathrm{T}}^{\mu,\,\mathrm{L1T}}$ generation

(b) Muon identification and $p_{\mathrm{T}}^{\mu,\,\mathrm{L1T}}$ generation

Figure 6.23: Closure tests of the parameterisation of the prompt muon contribution. Good agreement was observed between the two $p_{\mathrm{T}}^{\mu,\,\mathrm{L1T}}$ distributions.

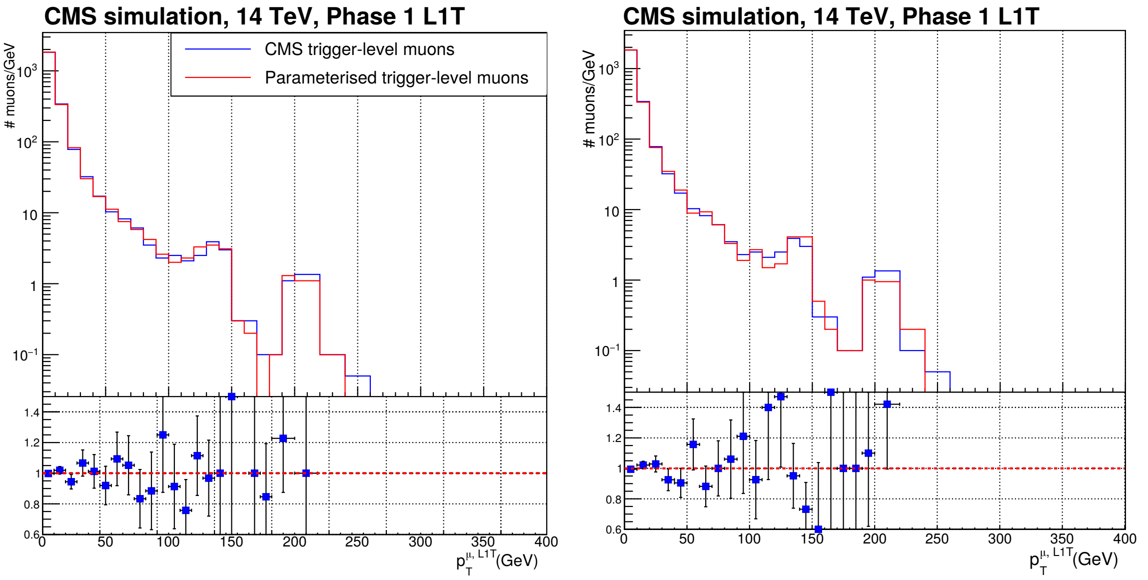

(a) $p_{\mathrm{T}}^{\mu,\,\mathrm{L1T}}$ generation

(b) Muon identification and $p_{\mathrm{T}}^{\mu,\,\mathrm{L1T}}$ generation

Figure 6.24: Closure tests of the parameterisation of the decay-in-flight and punch-through muon contributions. Good agreement was observed between the two $p_{\mathrm{T}}^{\mu,\,\mathrm{L1T}}$ distributions.

was observed. The source of this was not found, but the difference was deemed small enough to continue.

6.5.5 Rate closure test and correction factors

Trigger rates at an instantaneous luminosity of 5×10^{34} cm^{-2} s^{-1} and $\sqrt{s} = 13$ TeV were computed by first running the simulation on minimum bias events. Results were then scaled to $\langle \mathrm{PU} \rangle \approx 140$, or 200 for the histogrammed jets. This technique enabled computation of rates at different luminosity levels by scaling results, instead of reprocessing all the events.
Rates were computed by first obtaining the probability for a single minimum bias event to pass the trigger selection from the simulation, p_{pp}:

$$p_{\mathrm{pp}} = \frac{N_{\mathrm{pass}}}{N_{\mathrm{tot}}} \tag{6.5}$$

where N_{pass} is the number of minimum bias events passing the trigger in the simulation and N_{tot} is the total number of minimum bias events. A binomial distribution $B(p_{\mathrm{pp}}, \langle \mathrm{PU} \rangle, x)$, with x being the number of proton-proton interactions passing the trigger in a bunch crossing, was used to calculate the probability that an event at pile-up $\langle \mathrm{PU} \rangle$ will pass the same selection ($p_{\langle \mathrm{PU} \rangle}$):

$$p_{\langle \mathrm{PU} \rangle} = B(p_{\mathrm{pp}}, \langle \mathrm{PU} \rangle, x > 0) = 1 - B(p_{\mathrm{pp}}, \langle \mathrm{PU} \rangle, x = 0) = 1 - (1 - p_{\mathrm{pp}})^{\langle \mathrm{PU} \rangle} \tag{6.6}$$

This probability was then used to calculate the trigger rate using the formula:

$$R = f_{\mathrm{BX}} \cdot p_{\langle \mathrm{PU} \rangle} \tag{6.7}$$

where f_{BX} is the bunch crossing frequency.
It should be noted that if p_{pp} is sufficiently low that the probability of two simultaneous proton-proton interactions passing a trigger is negligible, Eq. 6.6 can be written as:

$$P_{\langle \mathrm{PU} \rangle} = 1 - (1 - p_{\mathrm{pp}})^{\langle \mathrm{PU} \rangle} \approx \langle \mathrm{PU} \rangle \cdot p_{\mathrm{pp}} \tag{6.8}$$

In this regime, the probability for a bunch crossing to pass a trigger, hence the trigger rate, linearly scales with the luminosity. Error propagation was applied to Eq. 6.8 to obtain the statistical uncertainty on the rate.
A comparison between the rate from CMS full simulation and the parameterisation for each trigger object that was studied is presented from Fig. 6.27 to Fig. 6.30. The bottom plot displays ratios between the two rates. These ratios were used as correction factors for FCC-hh rate estimation to compensate for any difference between the CMS full and parameterised simulations. In the next sections a short discussion of the comparison of each trigger object type will be given.

6.5.5.1 Phase-1 jets

The parameterised simulation accurately reproduces CMS rates up to p_{T} thresholds of 150 GeV. Above that threshold, the parameterised simulation tends to underestimate rates, up to a factor

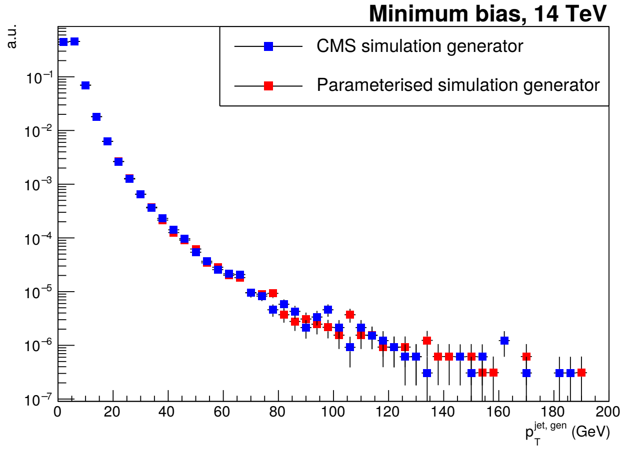

(a) $p_T^{\text{jet, gen}}$

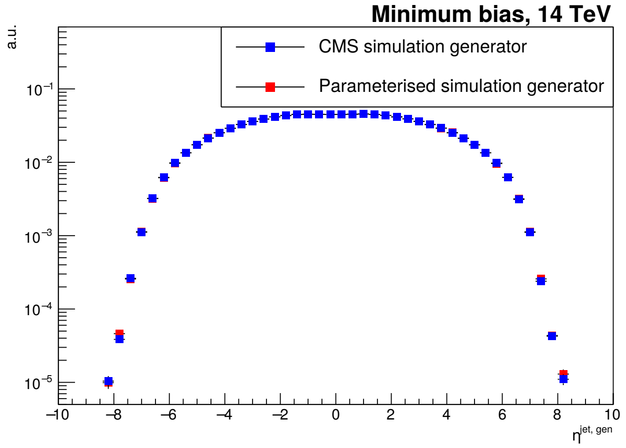

(b) $\eta^{\text{jet, gen}}$

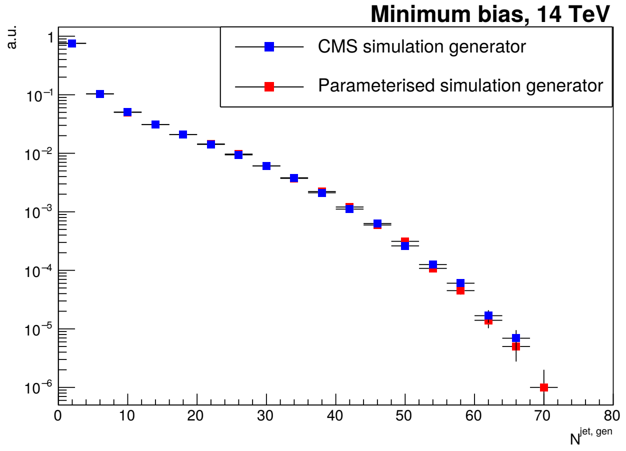

(c) Multiplicity

Figure 6.25: $p_T^{\text{jet, gen}}$, $\eta^{\text{jet, gen}}$ and jet multiplicity distribution comparison between CMS full-simulation and the parameterised simulation. The good agreement between the two shows that Pythia 8.223 was tuned correctly in the parameterised simulation.

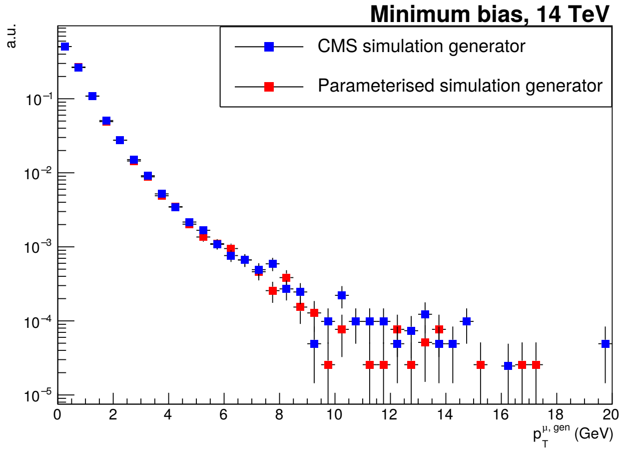

(a) $p_{\mathrm{T}}^{\mu,\text{ gen}}$

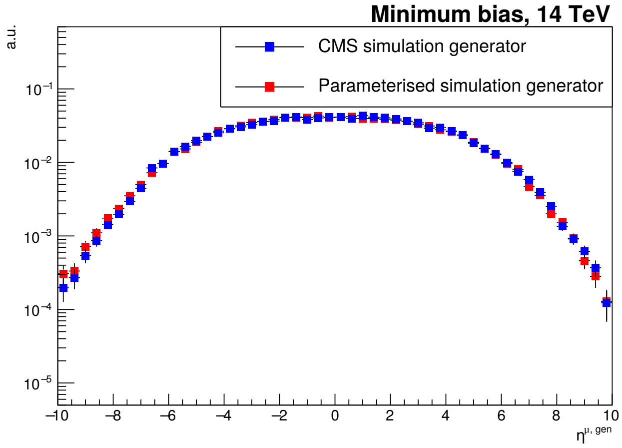

(b) $\eta^{\mu,\text{ gen}}$

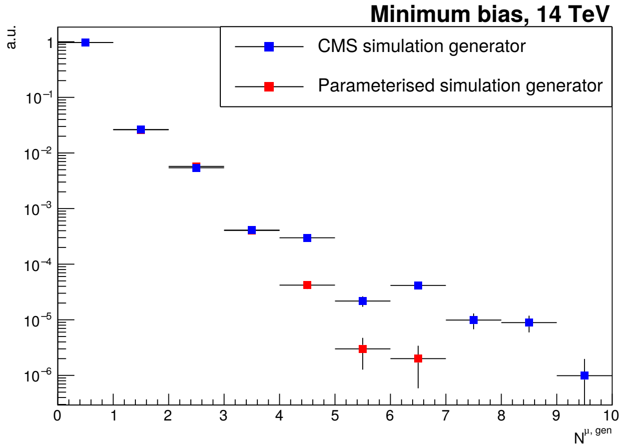

(c) Multiplicity

Figure 6.26: $p_{\mathrm{T}}^{\mu,\text{ gen}}$, $\eta^{\mu,\text{ gen}}$ and muon multiplicity distribution comparisons between CMS full-simulation and the parameterised simulation. Good agreement was observed in general, although a small underestimation in the number of events with more than four muons was found in the newly generated sample.

two. Although this may seem a significant difference, it should be observed that due to the exponential relation between rates and p_{T} thresholds, a factor two in rate difference corresponds to underestimating p_{T} thresholds by 10%. This was considered satisfactory for the FCC-hh study requirements.

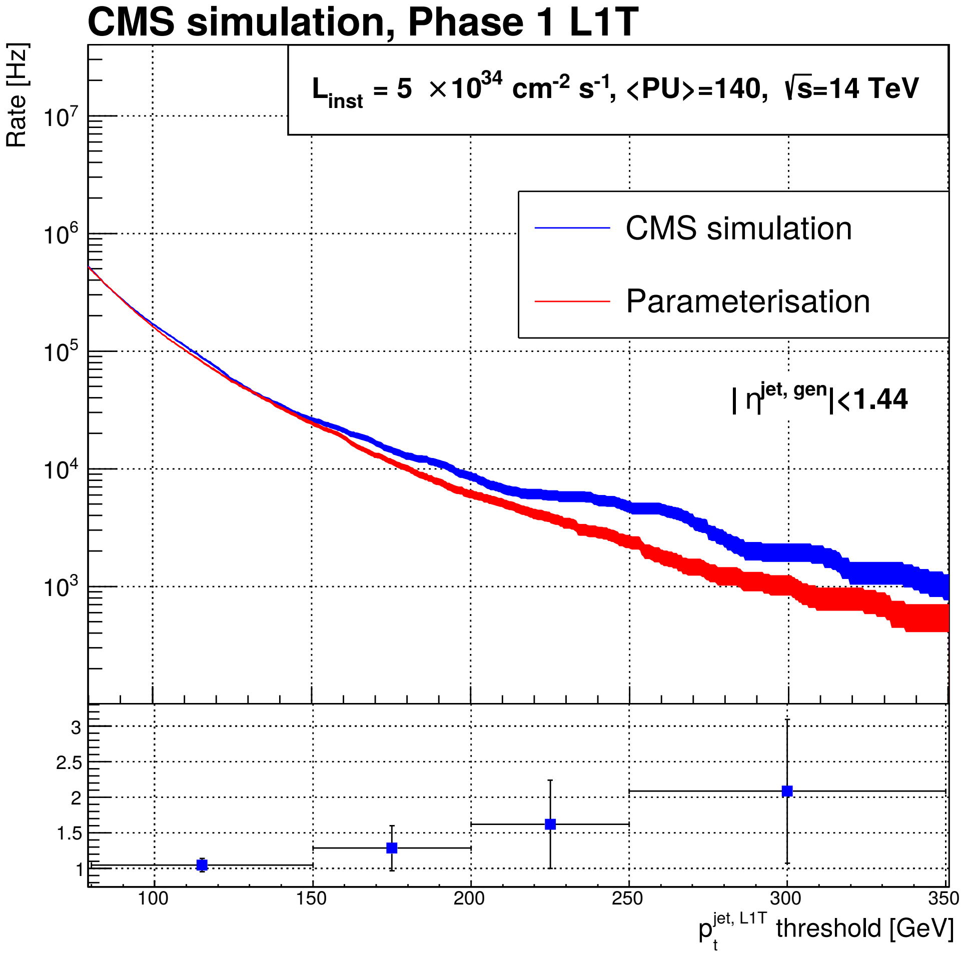

Figure 6.27: Upper plot: closure test of the jet trigger rate using the Phase-1 jet trigger parameterisation. Good agreement up to 150 GeV was obtained. Above 150 GeV the parameterised simulation increasingly underestimates rates. Bottom plot: scaling factors used in the FCC-hh rate estimation.

6.5.5.2 Histogrammed jets

The parameterised simulation seems to overestimate rates by around 25%, corresponding to a 10% overestimate of p_{T} thresholds.

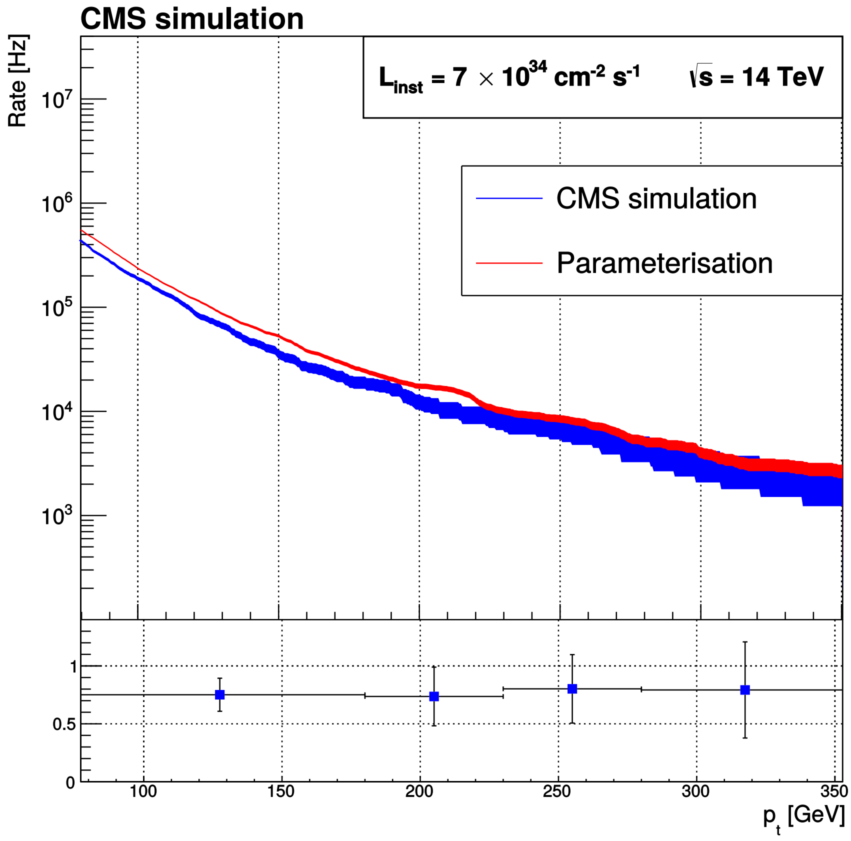

Figure 6.28: Upper plot: closure test of the jet trigger rate using the histogrammed jet trigger parameterisation. The parameterised simulation overestimates rate by around 25% over the p_T thresholds of interest. Bottom plot: scaling factors used in the FCC-hh rate estimation.

6.5.5.3 EGammas

Except for p_T thresholds below 20 GeV, the parameterised simulation constantly underestimates the rate by around 30%. Rates in both simulations reach a plateau of 5 kHz in the 80 – 130 GeV $p_T^{\text{EG, L1T}}$ range. The plateau rate is led by the relaxation of the H/E identification threshold at 128 GeV. Disagreements could be caused by the falling $p_T^{\text{jet, gen}}$ distribution in the QCD sample that causes the low $p_T^{\text{EG, L1T}}$ part of the momentum distribution to be over-represented. The issue could be solved by either using finer $p_T^{\text{jet, gen}}$ bins or by generating and simulating the detector response to a QCD sample with a more uniform $p_T^{\text{jet, gen}}$ spectrum. The first solution was not feasible due to the small statistics; the second required long and unpractical computing time to simulate the detector response. The problem was not further investigated, as this closure test also showed that rates are dominated by the H/E relaxation working point. This working point is carefully studied to suit the needs of CMS and would have to be tuned to match the new energy and luminosity conditions in a e/γ trigger at FCC-hh. Consequently, this leaves a large uncertainty in the e/γ rates at FCC-hh as they are dominated by the reconstruction algorithm configuration. In the light of this, the disagreements shown in the rate closure test were considered acceptable.

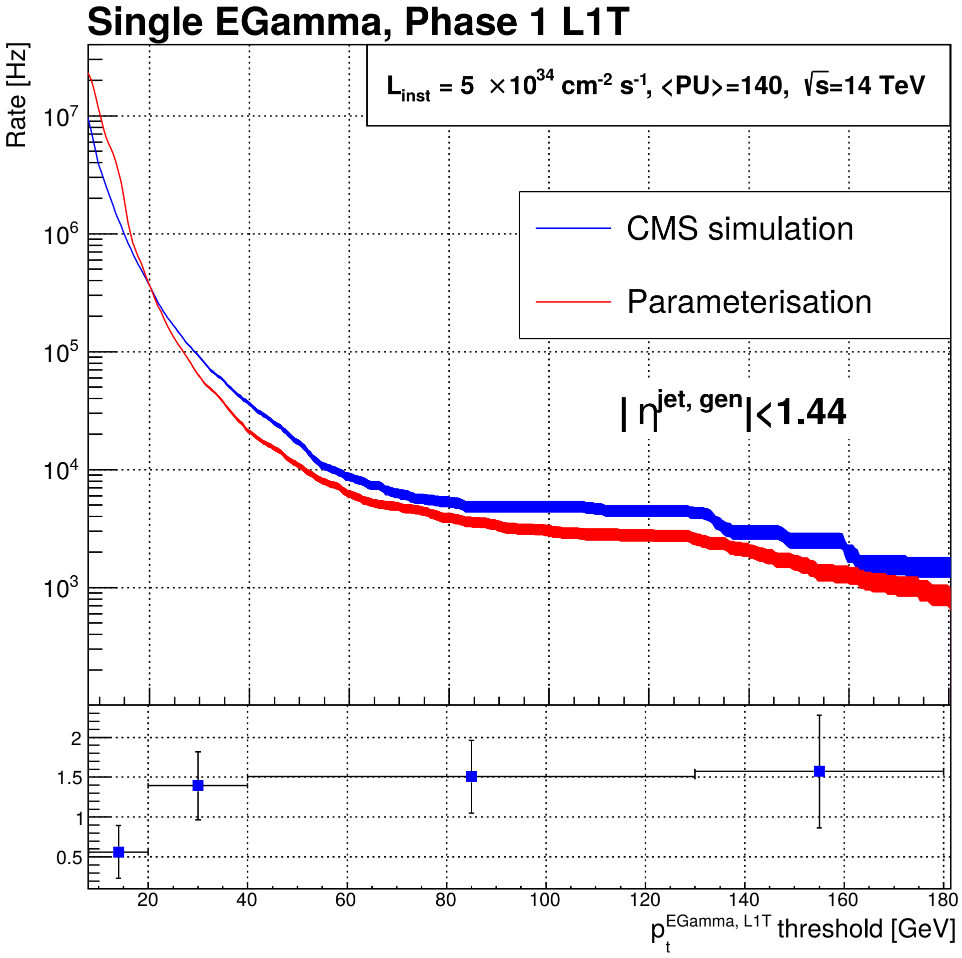

Figure 6.29: Upper plot: closure test of the e/γ trigger rate. Rates are underestimated by the parameterised simulation by 30%. Bottom plot: scaling factors used in the FCC-hh rate estimation.

6.5.5.4 Muons

Good agreement between the rate in output from the CMS full and parameterised simulation is observed. Prompt muons were found to account for around 50% of the rate.

6.5.6 Rates at 100 TeV

The parameterised simulation was configured to apply the CMS parameterisation to the FCC-hh detector presented in Section 6.2.3. The performance of the CMS jet and e/γ trigger in the barrel

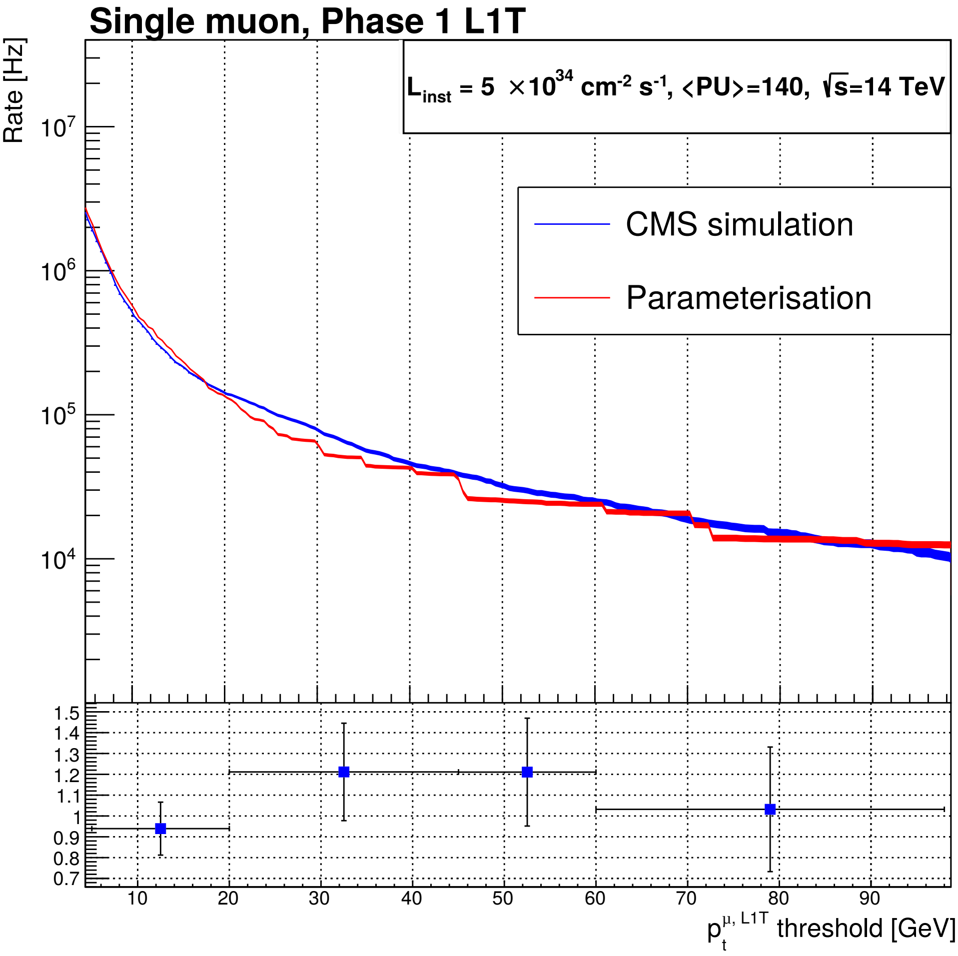

Figure 6.30: Upper plot: closure test of the muon trigger rate. Bottom plot: scaling factors used in the FCC-hh rate estimation.

was assumed to be the same over the entire FCC-hh detector, covering a pseudorapidity up to 6. The barrel muon detector was configured to cover $|\eta| < 1$. The barrel muon chambers of the FCC-hh detector are farther away from the beam line than in CMS, meaning the minimum p_T required to reach the detectors is greater than in CMS. The identification probability for any muon in the barrel with $p_T^{\mu,\text{ gen}} < 3.9$ GeV was set to null to take the larger radius into account, based on the information reported in Ref. [110]. The endcap muon detector was set to cover up to $|\eta| < 6$, with the same endcap detector performance as CMS. The probability of a proton interaction to give rise to a decay-in-flight or punch-through muon was increased by a factor 3.4, to take into account the increased multiplicity in the number of jets and particles at the higher centre-of-mass energy. The method described in Section 6.5.5 was used to compute rates and their statistical uncertainty. Finally, correction factors and their errors were applied in order to obtain the final estimation of rates at FCC-hh.

Results for each object type will be presented in the next sections, together with a short discussion.

6.5.6.1 Phase-1 jets

Rates obtained from the parameterised simulation, shown in Fig. 6.31, can be compared with those in Fig. 6.7. The 1-MHz p_{T} threshold was found to be 180 ± 20 GeV in the former and 150 GeV in the latter. The rate menu presented in page 32 of the technical design report of the Phase-2 CMS L1T [107] quotes a single jet rate of 42 and 69 kHz using a p_{T} threshold of 173 GeV at pile-up 140 and 200, respectively. The expected rate at the same p_{T} threshold in FCC-hh is 1.0 ± 0.2 MHz. The increase in rate is strongly led by physics: events at $\sqrt{s} = 100$ TeV have higher average transverse momentum and particle multiplicity, which impacts on the average number of jets and their average energy.

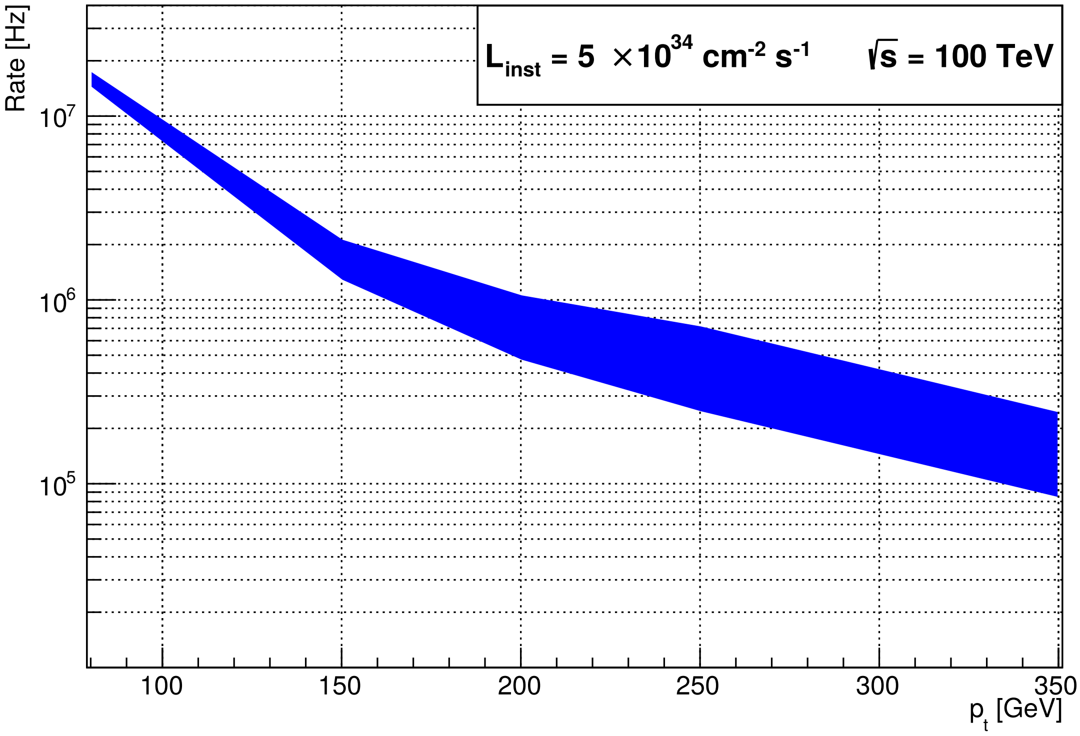

Figure 6.31: Single-jet trigger rate at FCC-hh for a jet trigger whose performance is the same as the CMS barrel jet trigger. The width of the band represents the rate uncertainty.

6.5.6.2 Histogrammed jets

Figure 6.32 presents rates obtained from the parameterised simulation. Comparing this result with the rate estimate in Fig. 6.31 shows that the histogrammed jet trigger algorithm can reduce rates by a factor two. The rate reduction can be explained by a multiple factors: the resolution curves of the histogrammed jet algorithm parameterisation are centred on zero, as the jet energy is corrected for pile-up contributions; the Phase-2 algorithm sums energy contributions over a smaller area than the Phase-1, therefore including less pile-up energy; using particle-flow inputs built with pile-up rejection techniques improves the jet trigger performance. Even if halved, the single-jet rates using the improved Phase-2 algorithm are high: a rate of approximately 600 kHz is expected using a p_{T} threshold of 173 GeV, as in the CMS Phase-2 L1T menu. A p_{T} threshold in the 300 – 350 GeV range is expected, if a bandwidth of 70 kHz is allocated to single-jet triggers.

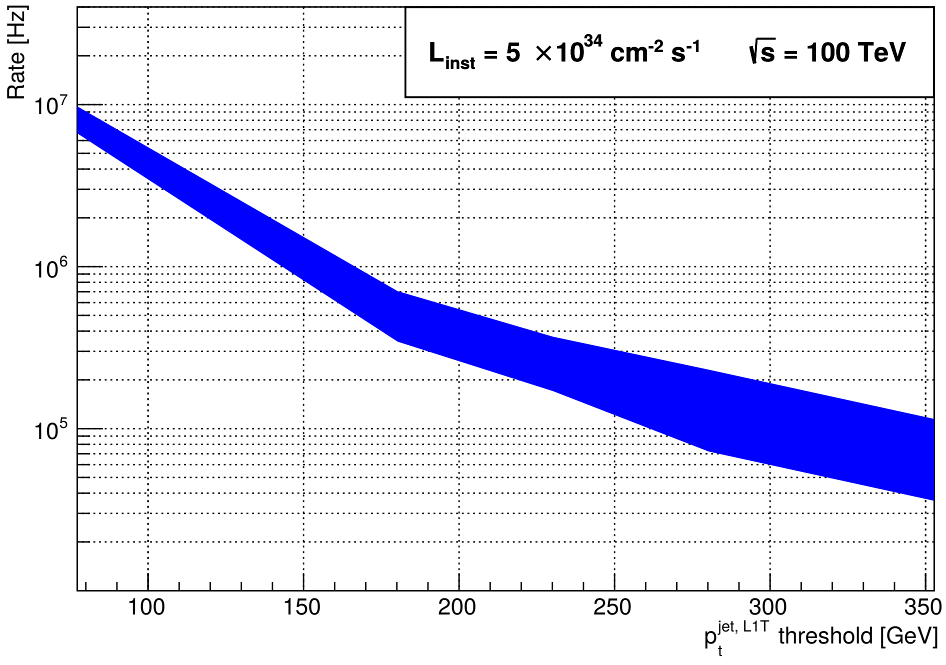

Figure 6.32: Single-jet trigger rate at FCC-hh using a parameterisation of the histogrammed jet trigger performance. The width of the band represents the rate uncertainty.

6.5.6.3 EGammas

Rates at FCC-hh are shown in Fig. 6.33. The 100-kHz p_{T} threshold is located at 175 GeV. The rise in the cross-section of QCD physics and jet energy significantly contributes to the increase in rate with the centre-of-mass energy. As the pile-up and energy increases, a larger fraction of jets passes the 128 GeV threshold, after which the H/E identification criteria is relaxed. Ideally, this working point and threshold would have to be tuned in an experiment at FCC-hh with a substantial impact on the e/γ object rates. Input from the tracker can improve the power of e/γ identification and pile-up rejection algorithms, strongly reducing rates.

6.5.6.4 Muons

Figure 6.34 shows that rates from the parameterised simulation are two orders of magnitude larger than those in Fig. 6.7 that were obtained using the scaling method. Trigger rates are over

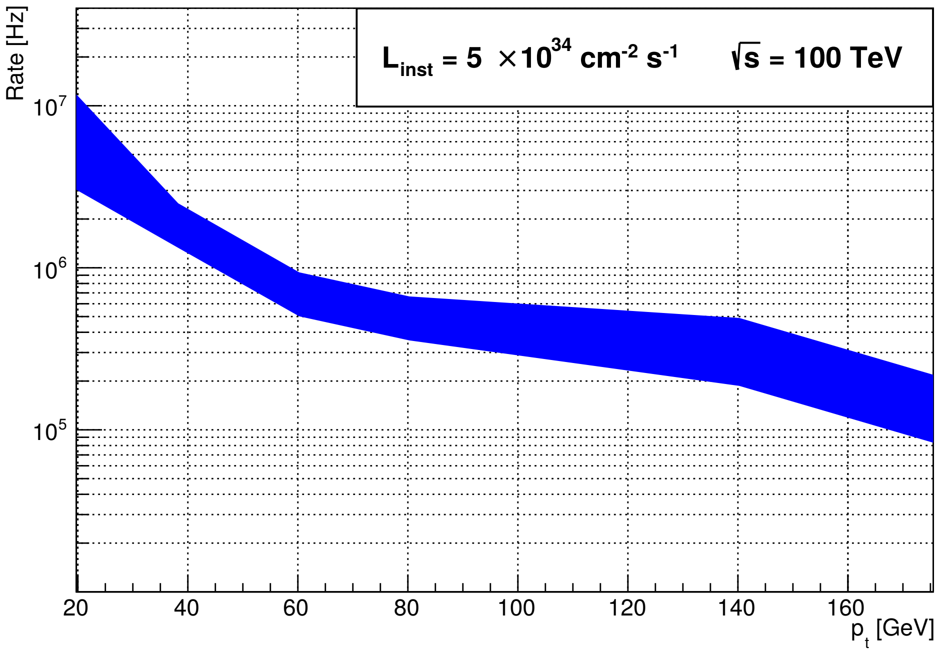

Figure 6.33: Single-e/γ trigger rate at FCC-hh. The width of the band represents the rate uncertainty.

100 kHz up to p_{T} thresholds of 90 GeV. The p_{T} resolution of the muon system strongly determines rates: the long tails displayed in Fig. 6.18 cause low-p_{T} muons to be reconstructed with much higher momentum. The p_{T} resolution becomes worse at high p_{T} as it becomes harder to measure the curvature of tracks. This causes rates to flatten for p_{T} thresholds above 70 GeV. Including information from the inner tracker greatly improves the muon reconstruction performance, and strongly mitigates this effect.

As mentioned in Section 6.2.3, the FCC-hh detector is expected to put less emphasis on standalone muon spectroscopy than CMS, with more focus on combining inner and outer tracks in the detector to measure the momentum of muons. Therefore, the issues seen in this study are expected to be worse in the actual FCC-hh detector as it is designed.

6.5.7 Conclusions and limits of the study

A comparison between the thresholds in Fig. 6.9 and the relative e/γ and muon trigger rates respectively shown in Figs. 6.33 and 6.34 indicates that triggering on electroweak physics using single-object triggers is not going to be possible without tracks in input. The study presented in Section 6.4 pointed out that this might be possible using a track trigger. Future work should investigate electron and muon triggers with tracks in input.

The parameterised simulation can be improved to better reproduce rates. More accurate para-

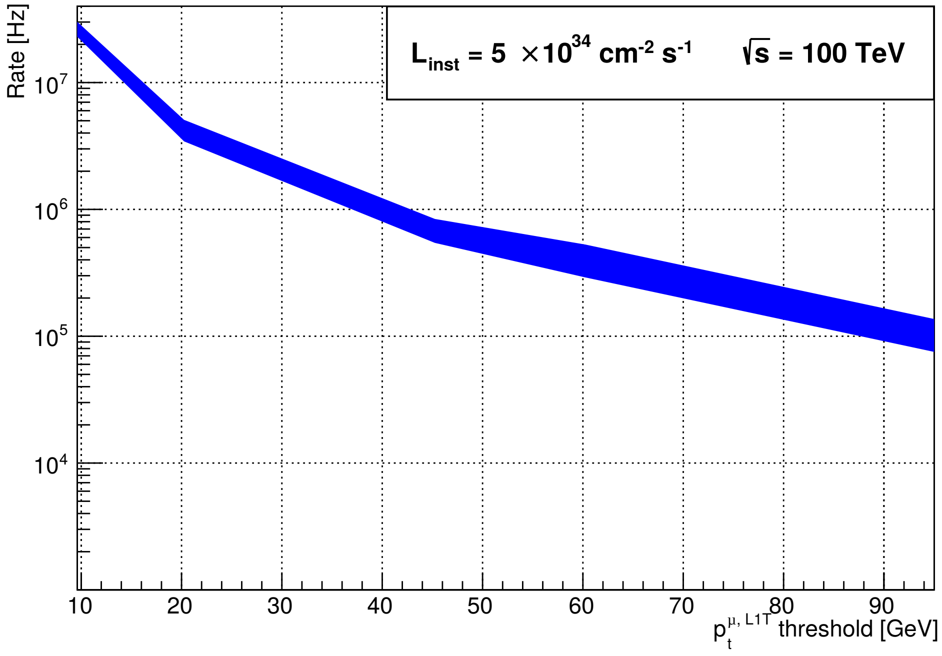

Figure 6.34: Single-muon trigger rate at FCC-hh using the new muon trigger parameterisation. The width of the band represents the rate uncertainty.

meters could be obtained by increasing the number of events used in the object matching step. Building an accurate muon trigger simulation was the most difficult task due to the complexity of the contributing processes. The decay-in-flight and punch-through component of the muon rate was parameterised using event properties due to the difficulties in extracting detailed decay information from the full-simulation. Finding a method to parameterise the two backgrounds by relating them to generator-level objects would improve the parameterisation and make it more flexible. Punch-through muons could be parameterised by computing muons starting from generator-level jets; decay-in-flight muons could be parameterised by studying properties of pion and kaon decays in a physics generator such as Pythia.

In any case, the parameterised simulation can be only used to have a first estimate of rates. Trigger systems are extremely susceptible to detector effects: material budget, non-sensitive detector regions, the reconstruction algorithms used, and many other factors affect rates in a non-trivial manner. A complete simulation of these effects will be required in order to finalise the design of the trigger architecture of a detector at FCC-hh.

6.6 Conclusions

An estimation of rates of a number of single-object triggers at FCC-hh at the instantaneous luminosity of 5×10^{34} cm^{-2} s^{-1} was presented in this chapter using two different methods. A simple method based on rescaling of rates of level-1 trigger of the CMS detector was used to compute a preliminary estimation of trigger rates at FCC-hh. A parameterised simulation of the CMS level-1 trigger was built to obtain a more solid estimate of trigger rates. The results based on the rescaling indicated that a trigger receiving tracks in input might be able to accept interesting physics events using single-object triggers while remaining within the rate limits of the system. The parameterised simulation showed that doing the same will be very hard without using data from the tracker.

The ultimate luminosity at FCC-hh, 30×10^{34} cm^{-2} s^{-1} , was not investigated, however a simple scaling of the results by the luminosity suggest that triggering with single-object triggers will not be possible even with input from the tracker. It is highly likely that a deeper shift in paradigm in trigger algorithms will be required to face the challenges at FCC-hh. Single-object triggers will have to be abandoned, or retained with high p_{T} thresholds, in favour of complex multi-object triggers. For instance, an algorithm that triggers on top quark production based on reconstructing and correlating the relative decay products could be designed and run on hardware. Larger FPGAs will be produced in the future, enabling more sophisticated and larger multi-object algorithms to be run in the level-1 trigger. Packages, such as HLS4ML [111], able to build and implement machine-learning algorithms on FPGA were developed in recent years. These techniques are expected to improve the object identification capabilities of the trigger. Further studies should be done to understand the extent of the improvements that can be obtained by using such techniques.

CONCLUSIONS

The trigger is a fundamental component of a particle detector that defines its physics reach. The processing power and selection quality of a trigger system must match the instantaneous luminosity of a collider and the signal-to-background ratio of the interesting physics processes.

The high-luminosity upgrade of the LHC will deliver an instantaneous luminosity up to $7 \times 10^{34}\ \mathrm{cm^{-2}\ s^{-1}}$, corresponding to an average pile-up of 200. A major upgrade of the CMS detector, including its trigger system, is scheduled in order to maintain its physics sensitivity at the increased luminosity. The upgraded level-1 trigger will be equipped with high-speed optical links and large field programmable gate arrays (FPGAs). The system will be able to run the particle flow algorithm for the first time. A trigger algorithm able to cluster hadron jets and compute energy sums starting from particle flow inputs was designed and the reconstruction performance studied. The jet algorithm was found to have similar performance to the anti-k_T algorithm with $\Delta R = 0.4$ run on the same inputs. Candidate offline p_T thresholds for the single jet, H_T, and $p_\mathrm{T}^\mathrm{miss}$ triggers were found to be 180, 450, and 200 GeV, respectively, each one corresponding to a trigger rate of 70, 11, and 18 kHz. These p_T thresholds are similar to the ones currently used at the instantaneous luminosity of $2 \times 10^{34}\ \mathrm{cm^{-2}\ s^{-1}}$, allowing CMS to retain its physics sensitivity at the much higher luminosity. The trigger algorithm was implemented in firmware targeting Xilinx FPGAs. The firmware was tested on a small-scale demonstrator setup running on a Xilinx KU15P FPGA and validated against software emulation, obtaining an agreement rate of 95.0%, 94.8%, and 97.7% for jets, $p_\mathrm{T}^\mathrm{miss}$, and H_T, respectively. Results from the demonstrator were used to compute estimates of the latency and resource usage of a full-scale algorithm running on a Xilinx VU9P FPGA. Around 42% LUTs, 12% FFs, and 3% DSPs are required to run the full-scale algorithm.

The FCC-hh is a project for a future hadron collider running at $\sqrt{s} = 100\ \mathrm{TeV}$, delivering a base instantaneous luminosity of $5 \times 10^{34}\ \mathrm{cm^{-2}\ s^{-1}}$, which will be raised to $30 \times 10^{34}\ \mathrm{cm^{-2}\ s^{-1}}$ in a second phase, corresponding to an average pile-up of 1000. The amount of information produced by the detector and the enormous pile-up background will pose a severe challenge to the trigger and data acquisition systems. Rates of single-object triggers were estimated by scaling CMS L1T rates and by building a parameterised simulation of the CMS L1T. The simulation showed that, at the instantaneous luminosity of 5×10^{34} cm^{-2} s^{-1} , the 100-kHz p_{T} threshold of single muon, e/γ , and jet triggers is expected to be around 90, 175, and 350 GeV. These thresholds are too high for collecting interesting electroweak physics, such as the Higgs boson pair production. Better reconstruction techniques may have to be developed, possibly by including tracks in the level-1 trigger, or a shift in the triggering strategies, such as developing new multi-object triggers, may be required in order to lower the p_{T} thresholds.

BIBLIOGRAPHY

[1] J M Campbell et al.
Report of the Snowmass 2013 energy frontier QCD working group.
Tech. rep. arXiv:1310.5189. ANL-HEP-CP-13-48. FERMILAB-FN-0967-CMS-T.
2013.
URL: `http://cds.cern.ch/record/1613344`.

[2] LHC-ILC Study Group.
"Physics Interplay of the LHC and the ILC. Physics interplay of the LHC and the ILC".
In: *Phys. Rep.* 426.SLAC-PUB-10764. ANL-HEP-PR-2004-108. CERN-PH-TH-2004-214. DCPT-2004-134. DESY-04-206. DESY-2004-206. IFIC-2004-59. IISc-CHEP-2004-13. IPPP-2004-67. SLAC-PUB-10764. UB-ECM-PF-2004-31. UCD-2004-28. UCI-TR-2004-37. 2-6 (2004), 47–358. 312 p.
DOI: `10.1016/j.physrep.2005.12.003`.
URL: `https://cds.cern.ch/record/800650`.

[3] M. Benedikt et al.
"Future Circular Collider Study. Volume 3: The Hadron Collider (FCC-hh) Conceptual Design Report".
In: *Eur. Phys. J. ST.* (December 2018).

[4] M. Benedikt et al.
"Future Circular Collider Study. Volume 2: The Lepton Collider (FCC-hh) Conceptual Design Report".
In: *Eur. Phys. J. ST.* (December 2018).

[5] E. Rutherford.
"The scattering of alpha and beta particles by matter and the structure of the atom".
In: *Phil. Mag. Ser. 6* 21 (1911), pp. 669–688.
DOI: `10.1080/14786440508637080`.

[6] Alois F. Kovarik.
"On the Automatic Registration of α-Particles, β-particles and γ-Ray and X-Ray Pulses".
In: *Phys. Rev.* 13 (4 1919), pp. 272–280.
DOI: `10.1103/PhysRev.13.272`.
URL: `https://link.aps.org/doi/10.1103/PhysRev.13.272`.

[7] J. H. Christenson et al.
"Evidence for the 2π Decay of the K_2^0 Meson".
In: *Phys. Rev. Lett.* 13 (4 1964), pp. 138–140.
DOI: `10.1103/PhysRevLett.13.138`.
URL: `https://link.aps.org/doi/10.1103/PhysRevLett.13.138`.

[8] Jheroen Dorenbosch.
"Trigger in UA2 and in UA1".
In: *eConf* C851111 (1985), pp. 134–151.

[9] N. Bains et al.
"The UA1 upgrade calorimeter trigger processor".
In: *Nucl. Instrum. Methods Phys. Res., A* 292.2 (1990), pp. 401 –423.
ISSN: 0168-9002.
DOI: `https://doi.org/10.1016/0168-9002(90)90396-N`.
URL: `http://www.sciencedirect.com/science/article/pii/016890029090396N`.

[10] ALEPH Collaboration.
"The design, construction and performance of the ALEPH silicon vertex detector".
In: *Nucl. Instrum. Methods Phys. Res., A* 379.CERN-PPE-96-041. CERN-ALEPH-PUB-96-001 (1996), 101–115. 26 p.
DOI: `10.1016/0168-9002(96)00281-1`.
URL: `https://cds.cern.ch/record/302130`.

[11] OPAL Collaboration.
"The OPAL detector at LEP".
In: *Phys. Lett. B* 251.CERN-PPE-90-114 (1990). Contribution to the Festschrift : M Morpurgo, 211–222. 93 p.
DOI: `10.1016/0168-9002(91)90547-4`.
URL: `https://cds.cern.ch/record/211674`.

[12] L3 Collaboration.
"L3 Experiment".
1982.
URL: `https://cds.cern.ch/record/5318`.

[13] DELPHI Collaboration.
"Performance of the DELPHI detector".
In: *Nucl. Instrum. Methods Phys. Res., A* 378.CERN-PPE-95-194 (1995), 57–100. 75 p.
DOI: `10.1016/0168-9002(96)00463-9`.
URL: `https://cds.cern.ch/record/295267`.

[14] R W Assmann, M Lamont, and S Myers.
"A Brief History of the LEP Collider".

In: *Nucl. Phys. B, Proc. Suppl.* 109.CERN-SL-2002-009-OP (2002), 17–31. 15 p.
DOI: `10.1016/S0920-5632(02)90005-8`.
URL: `https://cds.cern.ch/record/549223`.

[15] CDF Collaboration.
"The CDF Detector: An Overview".
In: *Nucl. Instrum. Meth. A* 271 (1988), pp. 387–403.
DOI: `10.1016/0168-9002(88)90298-7`.

[16] D0 Collaboration.
"Design Report: The D0 Experiment at the Fermilab Antiproton - Proton Collider".
In: (Oct. 1984).

[17] H T Edwards.
"The Tevatron Energy Doubler: A Superconducting Accelerator".
In: *Annual Review of Nuclear and Particle Science* 35.1 (1985), pp. 605–660.
DOI: `10.1146/annurev.ns.35.120185.003133`.
URL: `https://doi.org/10.1146/annurev.ns.35.120185.003133`.

[18] *HERA - A Proposal for a Large Electron Proton Colliding Beam Facility at DESY*.
1981.

[19] "Tevatron Run II Handbook".
In: (1998). Ed. by S.D. Holmes.

[20] H1 Collaboration.
"The H1 detector at HERA".
In: (July 1993).

[21] ZEUS Collaboration.
"The trigger of ZEUS, a flexible system for a high bunch crossing rate collider".
In: *Nucl. Instrum. Meth. A* 379 (1996). Ed. by B. Khazin, pp. 542–544.
DOI: `10.1016/0168-9002(96)00559-1`.

[22] CDF Collaboration.
The CDF-II detector: Technical design report.
Tech. rep. FERMILAB-DESIGN-1996-01. FERMILAB-PUB-96-390-E.
1996.
URL: `https://cds.cern.ch/record/1478626`.

[23] Graham Wilson et al.
"The run IIb trigger upgrade for the DO experiment".
In: (June 2004).

[24] Oliver Sim Brüning et al.
LHC Design Report.

CERN Yellow Reports: Monographs.
Geneva: CERN, 2004.
DOI: `10.5170/CERN-2004-003-V-1`.
URL: `https://cds.cern.ch/record/782076`.

[25] *ATLAS: technical proposal for a general-purpose pp experiment at the Large Hadron Collider at CERN.*
LHC Tech. Proposal.
Geneva: CERN, 1994.
URL: `https://cds.cern.ch/record/290968`.

[26] *CMS: the Compact Muon Solenoid; 1993 ed.*
Tech. rep. CERN-LHCC-93-48.
Geneva: CERN, 1993.
URL: `https://cds.cern.ch/record/290852`.

[27] *LHCb : Technical Proposal.*
Tech. Proposal.
Geneva: CERN, 1998.
URL: `https://cds.cern.ch/record/622031`.

[28] *ALICE: Technical proposal for a Large Ion collider Experiment at the CERN LHC.*
LHC Tech. Proposal.
Geneva: CERN, 1995.
URL: `https://cds.cern.ch/record/293391`.

[29] G et al Apollinari.
High-Luminosity Large Hadron Collider (HL-LHC): Preliminary Design Report.
CERN Yellow Reports: Monographs.
Geneva: CERN, 2015.
URL: `http://cds.cern.ch/record/2116337`.

[30] *ATLAS Phase-II Upgrade Scoping Document.*
Tech. rep. CERN-LHCC-2015-020. LHCC-G-166.
Geneva: CERN, 2015.
URL: `https://cds.cern.ch/record/2055248`.

[31] CMS Collaboration.
The Phase-2 Upgrade of the CMS Level-1 Trigger.
Tech. rep. CERN-LHCC-2020-004. CMS-TDR-021.
Geneva: CERN, 2020.
URL: `http://cds.cern.ch/record/2714892`.

[32] *LHCb Trigger and Online Upgrade Technical Design Report.*
Tech. rep. CERN-LHCC-2014-016. LHCB-TDR-016.

2014.
URL: `https://cds.cern.ch/record/1701361`.

[33] P Antonioli, A Kluge, and W Riegler.
Upgrade of the ALICE Readout & Trigger System.
Tech. rep. CERN-LHCC-2013-019. ALICE-TDR-015.
2013.
URL: `https://cds.cern.ch/record/1603472`.

[34] Michael E Peskin and Daniel V Schroeder.
An introduction to quantum field theory.
Includes exercises.
Boulder, CO: Westview, 1995.
URL: `https://cds.cern.ch/record/257493`.

[35] Andrew Purcell.
"Go on a particle quest at the first CERN webfest. Le premier webfest du CERN se lance à la conquête des particules".
In: BUL-NA-2012-269. 35/2012 (2012), p. 10.
URL: `https://cds.cern.ch/record/1473657`.

[36] R.Keith Ellis, W.James Stirling, and B.R. Webber.
QCD and collider physics.
Vol. 8.
Cambridge University Press, Feb. 2011.
ISBN: 978-0-511-82328-2, 978-0-521-54589-1.

[37] *DESY news: The most precise picture of the proton*.
URL: `https://www.desy.de/news/news_search/index_eng.html?openDirectAnchor=829`.

[38] Johannes Blümlein.
"The theory of deeply inelastic scattering".
In: *Progress in Particle and Nuclear Physics* 69 (2013), 28–84.
ISSN: 0146-6410.
DOI: `10.1016/j.ppnp.2012.09.006`.
URL: `http://dx.doi.org/10.1016/j.ppnp.2012.09.006`.

[39] Jonathan Pumplin et al.
"New Generation of Parton Distributions with Uncertainties from Global QCD Analysis".
In: *Journal of High Energy Physics* 2002.07 (2002), 012–012.
ISSN: 1029-8479.
DOI: `10.1088/1126-6708/2002/07/012`.
URL: `http://dx.doi.org/10.1088/1126-6708/2002/07/012`.

[40] V.N. Gribov and L.N. Lipatov.
"Deep inelastic e p scattering in perturbation theory".
In: *Sov. J. Nucl. Phys.* 15 (1972), pp. 438–450.

[41] Guido Altarelli and G. Parisi.
"Asymptotic Freedom in Parton Language".
In: *Nucl. Phys. B* 126 (1977), pp. 298–318.
DOI: `10.1016/0550-3213(77)90384-4`.

[42] Yuri L. Dokshitzer.
"Calculation of the Structure Functions for Deep Inelastic Scattering and e+ e- Annihilation by Perturbation Theory in Quantum Chromodynamics."
In: *Sov. Phys. JETP* 46 (1977), pp. 641–653.

[43] John C. Collins and Davison E. Soper.
"The Theorems of Perturbative QCD".
In: *Ann. Rev. Nucl. Part. Sci.* 37 (1987), pp. 383–409.
DOI: `10.1146/annurev.ns.37.120187.002123`.

[44] J. Varela.
"The Standard Model of Particle Physics - Lecture 3".
Lecture at Course on Physics at the LHC.
13th February 2012.
URL: `https://indico.cern.ch/event/174750/contributions/281134/`.

[45] ALICE collaboration.
"Measurements of jets in ALICE".
6th January 2016.
URL: `http://nattrass.utk.edu/Talks/EpiphanyJan2016/NattrassEpiphany2016.v4.pdf`.

[46] Mets501.
"Pseudorapidity plot".
24th July 2012.
URL: `https://commons.wikimedia.org/w/index.php?curid=20392149`.

[47] Micheal Leyton.
"Minimum Bias and Underlying Event Studies at ATLAS and CMS".
Talk at Rencontres de Moriond 2009.
18th March 2009.
URL: `http://moriond.in2p3.fr/QCD/2009/WednesdayAfternoon/Leyton.pdf`.

[48] ATLAS Collaboration.

“Measurement of the Inelastic Proton-Proton Cross Section at $\sqrt{s} = 13$ TeV with the ATLAS Detector at the LHC. Measurement of the Inelastic Proton-Proton Cross Section at $\sqrt{s} = 13$ TeV with the ATLAS Detector at the LHC”.
In: *Phys. Rev. Lett.* 117.CERN-EP-2016-140 (2016), 182002. 19 p.
DOI: `10.1103/PhysRevLett.117.182002`.
URL: `https://cds.cern.ch/record/2159578`.

[49] Torbjörn Sjöstrand, Stephen Mrenna, and Peter Skands.
“A brief introduction to PYTHIA 8.1”.
In: *Computer Physics Communications* 178.11 (2008), pp. 852 –867.
ISSN: 0010-4655.
DOI: `https://doi.org/10.1016/j.cpc.2008.01.036`.
URL: `http://www.sciencedirect.com/science/article/pii/S0010465508000441`.

[50] T. Pierog et al.
“EPOS LHC: Test of collective hadronization with data measured at the CERN Large Hadron Collider”.
In: *Phys. Rev. C* 92 (3 2015), p. 034906.
DOI: `10.1103/PhysRevC.92.034906`.
URL: `https://link.aps.org/doi/10.1103/PhysRevC.92.034906`.

[51] CMS Collaboration.
“Measurement of charged particle spectra in minimum-bias events from proton–proton collisions at $\sqrt{s} = 13\,\text{TeV}$”.
In: *Eur. Phys. J. C* 78.9 (2018), p. 697.
DOI: `10.1140/epjc/s10052-018-6144-y`.
arXiv: `1806.11245 [hep-ex]`.

[52] Gavin P. Salam.
“Towards jetography”.
In: *The European Physical Journal C* 67.3-4 (2010), 637–686.
ISSN: 1434-6052.
DOI: `10.1140/epjc/s10052-010-1314-6`.
URL: `http://dx.doi.org/10.1140/epjc/s10052-010-1314-6`.

[53] Matteo Cacciari, Gavin P Salam, and Gregory Soyez.
“The anti-kt jet clustering algorithm”.
In: *Journal of High Energy Physics* 2008.04 (2008), 063–063.
ISSN: 1029-8479.
DOI: `10.1088/1126-6708/2008/04/063`.
URL: `http://dx.doi.org/10.1088/1126-6708/2008/04/063`.

[54] Matteo Cacciari, Gavin P. Salam, and Gregory Soyez.

"FastJet user manual".
In: *The European Physical Journal C* 72.3 (2012).
ISSN: 1434-6052.
DOI: `10.1140/epjc/s10052-012-1896-2`.
URL: `http://dx.doi.org/10.1140/epjc/s10052-012-1896-2`.

[55] CMS Collaboration.
"Performance of CMS Muon Reconstruction in pp Collision Events at $\sqrt{s} = 7$ TeV".
In: *JINST* 7 (2012), P10002.
DOI: `10.1088/1748-0221/7/10/P10002`.
arXiv: `1206.4071 [physics.ins-det]`.

[56] CMS Collaboration.
Evidence for Higgs boson decay to a pair of muons.
Tech. rep. arXiv:2009.04363. CMS-HIG-19-006-003.
Submitted to JHEP.
Geneva: CERN, 2020.
URL: `http://cds.cern.ch/record/2730058`.

[57] ATLAS Collaboration.
"Observation of a new particle in the search for the Standard Model Higgs boson with the ATLAS detector at the LHC".
In: *Physics Letters B* 716.1 (2012), 1–29.
ISSN: 0370-2693.
DOI: `10.1016/j.physletb.2012.08.020`.
URL: `http://dx.doi.org/10.1016/j.physletb.2012.08.020`.

[58] "Observation of a new boson at a mass of 125 GeV with the CMS experiment at the LHC".
In: *Phys. Lett. B* 716.arXiv:1207.7235. CMS-HIG-12-028. CERN-PH-EP-2012-220 (2012), 30–61. 59 p.
URL: `https://cds.cern.ch/record/1471016`.

[59] A. Zaborowska for the FCC-hh detector group.
"FCC-hh and HE-LHC experiments & detectors overview".
Talk at the FCC Week 2018, Amsterdam.
9th April 2018.
URL: `https://indico.cern.ch/event/656491/contributions/2915653/`.

[60] S Borowka et al.
Higgs boson pair production in gluon fusion at NLO with full top-quark mass dependence.
Tech. rep. arXiv:1604.06447. MPP-2016-80. NSF-KITP-16-040. ZH-TH-14-16.
2016.
URL: `https://cds.cern.ch/record/2148163`.

[61] Andrew H. Jaffe.
"Cosmology 2012: Lecture Notes".
URL: `http://www.sr.bham.ac.uk/~smcgee/ObsCosmo/Jaffe_cosmology.pdf`.

[62] CMS Collaboration.
"Seeking Susy".
URL: `http://cms.web.cern.ch/news/seeking-susy`.

[63] Michael Duerr et al.
"Hunting the dark Higgs".
In: *Journal of High Energy Physics* 2017.4 (2017).
ISSN: 1029-8479.
DOI: `10.1007/jhep04(2017)143`.
URL: `http://dx.doi.org/10.1007/JHEP04(2017)143`.

[64] Thomas Sven Pettersson and P Lefèvre.
The Large Hadron Collider: conceptual design.
Tech. rep. CERN-AC-95-05-LHC.
1995.
URL: `https://cds.cern.ch/record/291782`.

[65] Jean-Luc Caron.
"Overall view of LHC experiments.. Vue d'ensemble des experiences du LHC."
AC Collection. Legacy of AC. Pictures from 1992 to 2002.
1998.
URL: `https://cds.cern.ch/record/841555`.

[66] Apollinari G. et al.
High-Luminosity Large Hadron Collider (HL-LHC): Technical Design Report.
CERN Yellow Reports: Monographs.
Geneva: CERN, 2017.
DOI: `10.23731/CYRM-2017-004`.
URL: `https://cds.cern.ch/record/2284929`.

[67] *CMS Detector Layout*.
URL: `http://www.hephy.at/user/friedl/diss/html/node8.html`.

[68] V Karimäki et al.
The CMS tracker system project: Technical Design Report.
Technical Design Report CMS.
Geneva: CERN, 1997.
URL: `https://cds.cern.ch/record/368412`.

[69] CMS Collaboration.
The Phase-2 Upgrade of the CMS Tracker.

Tech. rep. CERN-LHCC-2017-009. CMS-TDR-014.
Geneva: CERN, 2017.
URL: `https://cds.cern.ch/record/2272264`.

[70] *The CMS electromagnetic calorimeter project: Technical Design Report*.
Technical Design Report CMS.
Geneva: CERN, 1997.
URL: `https://cds.cern.ch/record/349375`.

[71] *The CMS hadron calorimeter project: Technical Design Report*.
Technical Design Report CMS.
Geneva: CERN, 1997.
URL: `https://cds.cern.ch/record/357153`.

[72] CMS Collaboration.
The Phase-2 Upgrade of the CMS Endcap Calorimeter.
Tech. rep. CERN-LHCC-2017-023. CMS-TDR-019.
Geneva: CERN, 2017.
URL: `https://cds.cern.ch/record/2293646`.

[73] *The CMS muon project: Technical Design Report*.
Technical Design Report CMS.
Geneva: CERN, 1997.
URL: `https://cds.cern.ch/record/343814`.

[74] CMS Collaboration.
The Phase-2 Upgrade of the CMS Muon Detectors.
Tech. rep. CERN-LHCC-2017-012. CMS-TDR-016.
Geneva: CERN, 2017.
URL: `https://cds.cern.ch/record/2283189`.

[75] CMS Collaboration.
CMS Technical Design Report for the Muon Endcap GEM Upgrade.
Tech. rep. CERN-LHCC-2015-012. CMS-TDR-013.
2015.
URL: `https://cds.cern.ch/record/2021453`.

[76] CMS Collaboration.
CMS TriDAS project: Technical Design Report, Volume 1: The Trigger Systems.
Technical Design Report CMS.
URL: `https://cds.cern.ch/record/706847`.

[77] Sergio Cittolin, Attila Rácz, and Paris Sphicas.
CMS The TriDAS Project: Technical Design Report, Volume 2: Data Acquisition and High-Level Trigger. CMS trigger and data-acquisition project.

Technical Design Report CMS.
Geneva: CERN, 2002.
URL: `https://cds.cern.ch/record/578006`.

[78] A Tapper and Darin Acosta.
CMS Technical Design Report for the Level-1 Trigger Upgrade.
Tech. rep. CERN-LHCC-2013-011. CMS-TDR-12.
Geneva: CERN, 2013.
URL: `https://cds.cern.ch/record/1556311`.

[79] M. Bachtis et al.
"Upgrade of the CMS Barrel Muon Track Finder for HL-LHC featuring a Kalman Filter algorithm and an ATCA Host Processor with Ultrascale+ FPGAs".
In: *PoS* TWEPP2018 (2019), p. 139.
DOI: `10.22323/1.343.0139`.

[80] R. Frazier et al.
"A demonstration of a time multiplexed trigger for the CMS experiment".
In: *JINST* 7 (2012), p. C01060.
DOI: `10.1088/1748-0221/7/01/C01060`.

[81] G. Hall.
"A time-multiplexed track-trigger for the CMS HL-LHC upgrade".
In: *Nuclear Instruments and Methods in Physics Research Section A: Accelerators, Spectrometers, Detectors and Associated Equipment* 824 (2016). Frontier Detectors for Frontier Physics: Proceedings of the 13th Pisa Meeting on Advanced Detectors, pp. 292 –295.
ISSN: 0168-9002.
DOI: `https://doi.org/10.1016/j.nima.2015.09.075`.
URL: `http://www.sciencedirect.com/science/article/pii/S0168900215011304`.

[82] Mahmoud Khaled.
"Enhancing the Performance of Digital Controllers using Distributed Multicore/Heterogeneous Embedded Systems".
PhD thesis. Jan. 2014.
DOI: `10.13140/2.1.4172.2245`.

[83] Xilinx.
"UltraScale Architecture - Configurable Logic Block".
28th February 2017.
URL: `https://www.xilinx.com/support/documentation/user_guides/ug574-ultrascale-clb.pdf`.

[84] *MicroTCA Overview*.
URL: `http://www.vadatech.com/media/article_MicroTCA_Overview.pdf`.

[85] J Butler et al.
Technical Proposal for the Phase-II Upgrade of the CMS Detector.
Tech. rep. CERN-LHCC-2015-010. LHCC-P-008.
Geneva. Geneva: CERN, 2015.
URL: `https://cds.cern.ch/record/2020886`.

[86] CMS Collaboration.
"Particle-flow reconstruction and global event description with the CMS detector".
In: *JINST* 12.CMS-PRF-14-001. CMS-PRF-14-001-004. 10 (2017), P10003. 82 p.
DOI: `10.1088/1748-0221/12/10/P10003`.
URL: `https://cds.cern.ch/record/2270046`.

[87] Daniele Bertolini et al.
"Pileup Per Particle Identification".
In: *JHEP* 10.arXiv:1407.6013 (2014), 59. 23 p.
DOI: `10.1007/JHEP10(2014)059`.
URL: `https://cds.cern.ch/record/1745357`.

[88] Siona Ruth Davis.
"CMS slice image view (transverse/longitudinal/3-D)".
In: (2016).
URL: `http://cds.cern.ch/record/2204863`.

[89] *AdvancedTCA Overview*.
URL: `https://www.picmg.org/openstandards/advancedtca/`.

[90] *ComExpress, PICMG"*.
URL: `https://www.picmg.org/openstandards/com-express`.

[91] *EMP framework guide*.
URL: `https://serenity.web.cern.ch/serenity/emp-fwk/`.

[92] S Agostinelli et al.
"GEANT4: A Simulation toolkit".
In: *Nucl. Instrum. Methods Phys. Res., A* 506.CERN-IT-2002-003. SLAC-PUB-9350. 3 (2002), 250–303. 86 p.
DOI: `10.1016/S0168-9002(03)01368-8`.
URL: `https://cds.cern.ch/record/602040`.

[93] CMS Collaboration.
Performance of the CMS Level-1 trigger in proton-proton collisions at $\sqrt{s}$ *= 13 TeV*.
Tech. rep. CERN-EP-2020-065. CMS-TRG-17-001-003.
Geneva: CERN, 2020.
URL: `https://cds.cern.ch/record/2721198`.

[94] Katie Walkingshaw-Pass.
"Implementing the MHT Algorithm".
Internal document.
2nd April 2020.

[95] *Vivado HLS website*.
URL: `https://www.xilinx.com/products/design-tools/vivado/integration/esl-design.html`.

[96] J. Volder.
"The CORDIC Computing Technique".
In: *Managing Requirements Knowledge, International Workshop on*.
Vol. 1.
Los Alamitos, CA, USA: IEEE Computer Society, 1959,
P. 257.
DOI: `10.1109/AFIPS.1959.57`.
URL: `https://doi.ieeecomputersociety.org/10.1109/AFIPS.1959.57`.

[97] David d'Enterria and Tanguy Pierog.
"Global properties of proton-proton collisions at $\sqrt{s} = 100$ TeV".
In: *JHEP* 08.arXiv:1604.08536 (2016), 170. 16 p.
DOI: `10.1007/JHEP08(2016)170`.
URL: `http://cds.cern.ch/record/2149519`.

[98] ALICE Collaboration.
"Pseudorapidity and transverse-momentum distributions of charged particles in proton-proton collisions at $\sqrt{s} = 13$ TeV".
In: *Phys. Lett. B* 753.CERN-PH-EP-2015-270. CERN-PH-EP-2015-270 (2015), 319–329. 19 p.
DOI: `10.1016/j.physletb.2015.12.030`.
URL: `https://cds.cern.ch/record/2056018`.

[99] R. Contino et al.
"Chapter 2: Higgs and EW Symmetry Breaking Studies".
In: *CERN Yellow Reports: Monographs* 3.0 (2017), p. 255.
ISSN: 2519-8076.
URL: `https://e-publishing.cern.ch/index.php/CYRM/article/view/513`.

[100] Loukas Gouskos, Allan Sung, and Joseph Incandela.
Search for stop scalar quarks at FCC-hh.
Tech. rep. CERN-ACC-2019-0036.
Geneva: CERN, 2018.
URL: `https://cds.cern.ch/record/2642475`.

[101] Simone Bologna et al.
"Trigger & Data Acquisition at FCC-hh".
Talk at the FCC Week 2018, Amsterdam.
12th April 2018.
URL: `https://indico.cern.ch/event/656491/contributions/2923411/`.

[102] Zbynek Drasal.
"FCC-hh machine design overview".
Talk at the FCC Week 2018, Amsterdam.
9th April 2018.
URL: `https://indico.cern.ch/event/656491/contributions/2939179/`.

[103] CMS Collaboration.
"Level-1 Jets and Sums Trigger Performance".
In: (2016).
URL: `http://cds.cern.ch/record/2194257`.

[104] CMS collaboration.
"Use of tracking in the CMS L1 trigger for the Phase-2 upgrade".
Internal document, DN-2014/002.
4th August 2019.

[105] J. de Favereau et al.
"DELPHES 3: a modular framework for fast simulation of a generic collider experiment".
In: *Journal of High Energy Physics* 2014.2 (2014), p. 57.
ISSN: 1029-8479.
DOI: `10.1007/JHEP02(2014)057`.
URL: `https://doi.org/10.1007/JHEP02(2014)057`.

[106] CMS Collaboration.
Particle-Flow Event Reconstruction in CMS and Performance for Jets, Taus, and MET.
Tech. rep. CMS-PAS-PFT-09-001.
Geneva: CERN, 2009.
URL: `https://cds.cern.ch/record/1194487`.

[107] CMS Collaboration.
The Phase-2 Upgrade of the CMS L1 Trigger Interim Technical Design Report.
Tech. rep. CERN-LHCC-2017-013. CMS-TDR-017.
Geneva: CERN, 2017.
URL: `https://cds.cern.ch/record/2283192`.

[108] Rene Brun and Fons Rademakers.
"'ROOT — An object oriented data analysis framework'".

In: *Nuclear Instruments and Methods in Physics Research Section A: Accelerators, Spectrometers, Detectors and Associated Equipment* 389.1 (1997). New Computing Techniques in Physics Research V, pp. 81 –86.
ISSN: 0168-9002.
DOI: `https://doi.org/10.1016/S0168-9002(97)00048-X`.
URL: `http://www.sciencedirect.com/science/article/pii/S016890029700048X`.

[109] J H Friedman.
"Data analysis techniques for high energy particle physics".
In: SLAC-176 (1974), 96 p.
DOI: `10.5170/CERN-1974-023.271`.
URL: `http://cds.cern.ch/record/695770`.

[110] W. Riegler for the FCC-hh collaboration.
"Muon system".
Talk at the FCC Week 2017, Berlin.
29th May 2017.
URL: `https://indico.cern.ch/event/556692/contributions/2465161`.

[111] Giuseppe Di Guglielmo et al.
Compressing deep neural networks on FPGAs to binary and ternary precision with HLS4ML.
2020.
arXiv: `2003.06308 [cs.LG]`.

LIST OF ACRONYMS

AK4 Anti-k_T algorithm with a distance parameter of 0.4

ALICE A Large Ion Collider Experiment

ASIC Application Specific Integrated Circuit

ATCA Advanced Telecommunications Computing Architecture

ATLAS A Toroidal LHC ApparatuS

BCT Barrel Calorimeter Trigger

BMTF Barrel Muon Track Finder

CERN Conseil Européen pour la Recherche Nucléaire (European Organization for Nuclear Research)

CLB Configurable Logic Block

CMS Compact Muon Solenoid

CORDIC Coordinate rotation digital computer

CSC Cathode Strip Chamber

CT Correlator Trigger

DAQ Data Acquisition

DSP Digital Signal Processor

DT Drift Tube

ECAL Electromagnetic CALorimeter

EMP Extensible Modular (data) Processor framework

EMTF Endcap Muon Track Finder

FCC Future Circular Collider

FCC-ee Future Circular Collider Electron-Positron

FCC-eh Future Circular Collider Electron-Hadron

FCC-hh Future Circular Collider Hadron-Hadron

FF Flip Flop

FPGA Field Programmable Gate Array

GCT Global Calorimeter Trigger

GEM Gas Electron Multiplier

GMT Global Muon Trigger

GT Global Trigger

GTT Global Track Trigger

HCAL Hadronic CALorimeter

HDL Hardware Description Language

HF Hadron Forward calorimeter

HGCAL High-Granularity CALorimeter

HL-LHC High Luminosity Large Hadron Collider

HLS High-Level Synthesis

HLT High-Level Trigger

IRC InfraRed and Collinear (safety)

L1T Level-1 Trigger

LEP Large Electron Positron collider

LHC Large Hadron Collider

LHCb Large Hadron Collider

LUT Look-Up Table

MET Missing Transverse Energy

NP New Physics

OMTF Overlap Muon Track Finder

PDF Parton Distribution Function

PF Particle Flow

PU Pile-Up

PUPPI Pile-Up Per Particle Identification

QCD Quantum ChromoDynamics

QGP Quark-Gluon Plasma

RPC Resistive Plate Chamber

SM Standard Model

SMASH Serenity MAnagement SHell

SPPS Super Proton-Antiproton Synchrotron

SPS Super Proton Synchrotron

SUSY SUper SYmmetry

TP Trigger Primitive

TT Trigger Tower

UE Underlying Event

μ**TCA** Micro Telecommunications Computing Architecture

VEV Vacuum Expectation Value